LEVEL II

(2)

(6)

APPLICATION OF THE INTEGRAL THEORY OF IMPACT TO THE QUALIFICATION OF MATERIALS AND THE DEVELOPMENT OF A SIMPLIFIED ROD PENETRATOR MODEL.

(10) Ross M. /Contiliano Thomas B. /McDonough
Claude V. /Swanson

AERONAUTICAL RESEARCH ASSOCIATES OF PRINCETON, INC.
50 WASHINGTON ROAD, P.O. BOX 2229
PRINCETON, NEW JERSEY 08540

(15) DAAD25-76-C-1757, DARPA Order-3097

(11) Nov[redacted]78 (12) 157

(9) FINAL REPORT,

FOR PERIOD 15 MAR[redacted]76 - 30 SEP[redacted]78.

PREPARED FOR (14) ARAP-368

DEFENSE ADVANCED RESEARCH PROJECTS AGENCY
1400 WILSON BOULEVARD
ARLINGTON, VIRGINIA 22209

U.S. ARMY BALLISTIC RESEARCH LABORATORIES
ABERDEEN PROVING GROUND, MARYLAND 21005

009400

UNCLASSIFIED

SECURITY CLASSIFICATION OF THIS PAGE (When Data Entered)

REPORT DOCUMENTATION PAGE

READ INSTRUCTIONS BEFORE COMPLETING FORM

1. REPORT NUMBER

2. GOVT ACCESSION NO. AD-A100 152

3. RECIPIENT'S CATALOG NUMBER

4. TITLE (and Subtitle)
APPLICATION OF THE INTEGRAL THEORY OF IMPACT TO THE QUALIFICATION OF MATERIALS AND THE DEVELOPMENT OF A SIMPLIFIED ROD PENETRATOR MODEL

5. TYPE OF REPORT & PERIOD COVERED
Final
15 Mar '76 - 30 Sep '78

6. PERFORMING ORG. REPORT NUMBER
A.R.A.P. Report No. 368

7. AUTHOR(s)
Ross M. Contiliano
Thomas B. McDonough
Claude V. Swanson

8. CONTRACT OR GRANT NUMBER(s)
DAAD05-76-C-0757

9. PERFORMING ORGANIZATION NAME AND ADDRESS
Aeronautical Research Associates of Princeton, Inc., 50 Washington Road
Princeton, New Jersey 08540

10. PROGRAM ELEMENT, PROJECT, TASK AREA & WORK UNIT NUMBERS
ARPA Order No. 3090

11. CONTROLLING OFFICE NAME AND ADDRESS
Defense Advanced Research Projects Agency
1400 Wilson Boulevard
Arlington, Virginia 22209

12. REPORT DATE
November 1978

13. NUMBER OF PAGES
151

14. MONITORING AGENCY NAME & ADDRESS (if different from Controlling Office)
U.S. Army Ballistic Research Laboratories
Aberdeen Proving Ground, Maryland 21005

15. SECURITY CLASS. (of this report)
UNCLASSIFIED

15a. DECLASSIFICATION/DOWNGRADING SCHEDULE

16. DISTRIBUTION STATEMENT (of this Report)

Approved for public release, distribution unlimited.

17. DISTRIBUTION STATEMENT (of the abstract entered in Block 20, if different from Report)

18. SUPPLEMENTARY NOTES

19. KEY WORDS (Continue on reverse side if necessary and identify by block number)

Impact	Armor
Integral Theory	Penetrator
Integral Theory of Impact	Rod Penetrator
Material Properties	Brittle Fracture
Adiabatic Hardness	Energy Partitioning

20. ABSTRACT (Continue on reverse side if necessary and identify by block number)

The Integral Theory of Impact has been used to evaluate two characteristic properties for many target materials. One property, E'_{*p}, represents the energy absorbed during plastic deformation of the target; the other, E_{*e}, represents the absorbed elastic energy. A series of impact tests was conducted in A.R.A.P.'s Impact Facility for each material. The data from these tests are in excellent agreement with the results of computations

DD FORM 1 JAN 73 1473 EDITION OF 1 NOV 65 IS OBSOLETE

UNCLASSIFIED

SECURITY CLASSIFICATION OF THIS PAGE (When Data Entered)

using the Integral Theory and the properties E'_{*p} and E'_{*e}. A theory has been developed which relates E'_{*p} and E'_{*e} to fundamental material properties which can be measured in the laboratory.

A rod penetrator model has also been developed using the Integral Theory. The rod is approximated by two cells. The first cell models the deforming region at the leading edge; the second cell models the rigid shaft. Material strengths are incorporated through the "adiabatic hardness" as measured by ρE_{*p}. Equations of motion and conservation equations are satisfied in a global sense and are solved numerically. The resulting computations agree well with data.

A fundamental experiment has been conducted to measure the partitioning of energy during brittle fracture of a penetrator specimen.

PREFACE

This report covers work performed for the Ballistic Research Laboratories with funds provided by the Defense Advanced Research Projects Agency under contract number DAAD05-76-C-0757. The program director at DARPA was initially Dr. Ernest Blase and subsequently Dr. Raymond Gogolewski. The contract monitor at BRL was Mr. Louis Giglio-Tos. The work was performed during the period 15 March 1976 to 30 September 1978.

The authors wish to thank Dr. Coleman duP. Donaldson, A.R.A.P. President and Senior Consultant, for his expert consultations and guidance during the course of this work. They also wish to thank Mr. Jimmy Hillhouse who performed the material qualification tests and Mr. Sylvester Hight who performed the E_{*d} tests for their diligence. The careful typing of this manuscript by Mrs. Virginia Anderson and preparation of the drawings by Mrs. Patricia Tobin is also gratefully acknowledged.

TABLE OF CONTENTS

Chapter			Page
I		INTRODUCTION	1
II		TARGET MATERIAL QUALIFICATION	4
	A	Rigid Sphere Impacting Semi-Infinite Target	4
	B	Experimental Program	13
	C	Data Theory Correlations	18
	D	Summary of Qualification Tests	30
III		IMPACT PROPERTIES OF MATERIALS	37
	A	Formulas for E_{*p} and E_{*e}	37
	B	Table of Materials Properties	40
IV		LONG ROD PENETRATOR MODEL	43
	A	Physics of the Model	44
	B	Correlations of Theory and Data	55
V		E_{*d} EXPERIMENTS	65
	A	Test Concept	65
	B	Experimental Program	67
	C	Test Results	78
VI		CONCLUSIONS	99
VII		REFERENCES	100

APPENDIX

A	MATERIAL QUALIFICATION TEST DATA	101
B	E_* EVALUATION	110
C	USER'S GUIDE TO ROD CODE	125

I. INTRODUCTION

This report presents the significant results of a two and one half year research program conducted by A.R.A.P. under contract number DAAD05-76-C-0757. The primary objective of the program was to gain an understanding of the underlying physics of the impact process and to apply this knowledge in the development of a simple model to describe the penetrator-target interaction.

The program evolved in three distinct phases. Phase 1 dealt with the characterization of target materials. Phase 2 dealt with the development of a long rod penetrator model. The final phase concerned the measurement of the partitioning of energy during fracture of a penetrator specimen.

Interim reports were issued at the end of Phase 1 and Phase 2 (Refs. 1 and 2). Some of the work described in these reports was incomplete, and some of the results have had to be revised in the light of subsequent developments. It is the purpose of this report to tie together the loose ends from the first two phases and to present for the first time the results of Phase 3 of the research program.

Prior to the inception of this program, a useful tool for the study of the impact process was under development at A.R.A.P. This tool, called the Integral Theory of Impact, sought to describe the impact process in as simple terms as possible without sacrificing the essential physics which were thought to describe the problem. Rather than worry about the microscopic details of the interaction of two materials during impact, it was decided to model the interaction in a global or integral sense. In this way, a set of ordinary rather than partial differential equations was obtained - an attractive simplification from both cost and time viewpoints. Since the equations used in the theory retain the essential physics of the impact process in an integral sense,

---

1. Donaldson, Coleman duP., Contiliano, Ross M., and McDonough, Thomas B.: The Qualification of Target Materials Using the Integral Theory of Impact. A.R.A.P. Rept. No. 295, Aeronautical Research Associates of Princeton, Inc., December 1976.

2. Swanson, Claude V. and Donaldson, Coleman duP.: Application of the Integral Impact Theory to Modeling Long-Rod Penetrators. A.R.A.P. Rept. No. 333, Aeronautical Research Associates of Princeton, Inc., March 1978.

it was felt that the important features of such processes could be exhibited in spite of the simplicity of the model. Thus, the integral theory was born in an attempt to bridge the gap between the complex and costly multi-element codes and the purely empirical models.

It was not intended that the integral theory replace either the large codes or the experimentalist. Because of its simplicity, the model introduces a degree of economy which makes it reasonable to conduct parametric studies and observe trends rather than single points. In this way, the integral theory can be used to guide experimental programs, interpret results, and serve as a screening tool for cases which require the details which are only available in the large codes.

Early studies (Ref. 3) of the impact process showed that for the purpose of computing target response during impact it was necessary to determine at least two characteristic quantities, in addition to density, for any target material. One of these, denoted by E_{*p} and called the hydrodynamic mode energy, represents the amount of energy required to put a well defined mass of target material in a hydrodynamic state. The other quantity, denoted by E_{*e}, represents the elastic energy absorbed by the same mass of target material during impact. Phase 1 of this program consisted of an experimental and theoretical evaluation of E_{*p} and E_{*e} for a wide spectrum of target materials. Reference 1 summarized the experimental program and evaluation of E_{*p} and E_{*e} and the development of equations to predict these two quantities from fundamental material properties. More recently, additional materials have been qualified and coefficients in the theoretical equations have been modified as more data have become available. In addition, the correlations which were reported in Ref. 1 have been revised to include a better estimate for the drag coefficient which appears in the equations. The results of all qualification tests and the present best estimates for the theoretical value of F_*, i.e., the sum of E_{*p} and E_{*e}, are described in Chapters II and III.

---

3. Donaldson, Coleman duP., McDonough, Thomas B., and Contiliano, Ross M.: Application of the Integral Impact Theory to the Design of Specialized Tactical Ordnance. A.R.A.P. Rept. No. 279, Aeronautical Research Associates of Princeton, Inc., May 1976.

During the second phase of this program, attention was directed toward the design of rod penetrators. The concepts of the integral theory were applied to the development of a long rod penetrator model. A two-element model was developed which incorporates the physics of the deforming single cell model developed several years ago by A.R.A.P. (Ref. 4) and couples this cell to a rigid shaft. This model was described in Ref. 2. However, the code which was developed contained several bugs and was difficult to utilize. In order to eliminate these problems, the equations of the model were recast, and the code was rewritten. The revised model and code are described in this report.

The rod model requires the specification of a property, E_{*d}, which represents the non-recoverable or dissipated energy required to hydrodynamicize a unit mass of the rod material as the tip of the rod is forced to flow out of the path of the relatively undamaged shaft of the penetrator. In essence, E_{*d} is to the rod what E_{*p} is to the target. The property E_{*d} can be obtained by correlating experimental data with calculations using the two-cell model. Alternatively, an experimental technique was devised by A.R.A.P. to measure E_{*d} directly. The results of these experiments are also described in this report.

In what follows, a summary of the entire target materials qualification program is provided in Chapter II. For completeness, the test data are provided in Appendix A, and the deduced values of E_* are shown in Appendix B. The theoretical model for E_* based on fundamental material properties is provided in Chapter III together with the present estimates for the theoretical E_* of many materials. Chapter IV contains a description of the long rod penetrator model. A user's guide for the numerical code is provided in Appendix C. Chapter V describes the E_{*d} experiments, and Chapter VI contains the conclusions drawn from this program.

---

4. Donaldson, Coleman duP., Contiliano, Ross M., and McDonough, Thomas B.: A Study of Water Drop Displacement and Deformation in Aerodynamic Shock Layers. A.R.A.P. Rept. No. 265, Aeronautical Research Associates of Princeton, Inc., March 1978.

II. TARGET MATERIAL QUALIFICATION

In this chapter, the method by which the impact properties E_{*p} and E_{*e} of a target material are obtained will be described. Briefly, the procedure consists of conducting a series of impact tests using nondeforming projectiles and relatively thick target samples. By eliminating the deformation of the projectile and backface effects in the target, the equations of motion are simplified and an impact can be completely specified given the density and geometry of the projectile and target plus the material property E_* of the target. In the next section, the Integral Theory of Impact will be developed for a nondeforming sphere impacting a semi-infinite target to show how E_{*p} and E_{*e} are evaluated. In the subsequent section, the results of an experimental program to characterize a wide range of target materials will be summarized.

A. Rigid Sphere Impacting Semi-Infinite Target

1. Decelerating Force - Consider the penetration of a semi-infinite target by a nondeforming sphere of radius R and mass m_p which is traveling at a velocity V_{c_o} normal to the target. At any instant during the penetration, the projectile, which has traveled a distance z, has a velocity V_c and is being decelerated by a force F. The nomenclature is depicted schematically in Figure 1. Conservation of momentum requires that

$$\frac{d}{dt}\left(m_p V_c\right) = -F \ . \tag{1}$$

If both sides of Eq. (1) are multiplied by V_c, the result is the equation for the rate of change of the center of mass kinetic energy

$$\frac{d}{dt}\left(m_p \frac{V_c^2}{2}\right) = -FV_c \ . \tag{2}$$

The product FV_c is the rate at which the projectile loses kinetic energy or the rate at which work is done on the target by the projectile. If W_t is the total energy of the target material, then

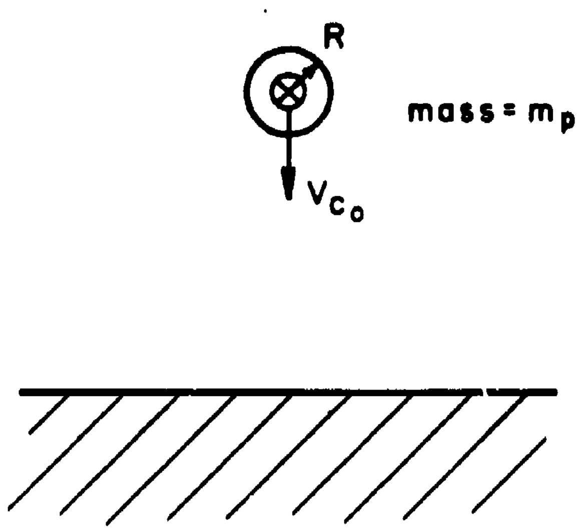

Before impact

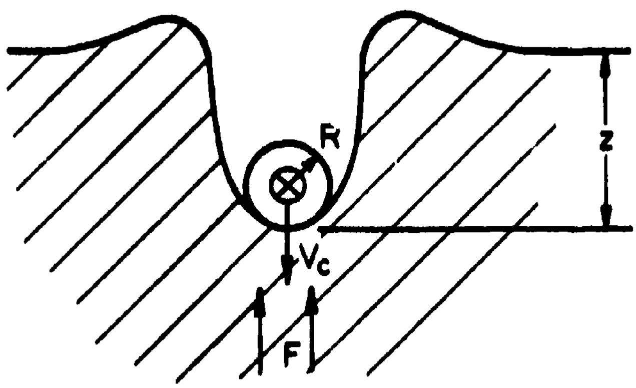

During impact

Figure 1

$$\frac{d}{dt} W_t = FV_c \ , \tag{3}$$

or

$$\frac{d}{dt}\left(m_p \frac{V_c^2}{2} + W_t\right) = 0 \ , \tag{4}$$

which is just a restatement of conservation of total energy.

The energy absorbed by the target is distributed between kinetic energy of the target material K_t and a quantity U_t which represents nonkinetic forms of energy such as plastic work and elastic energy

$$\frac{d\,W_t}{dt} = \frac{d\,K_t}{dt} + \frac{d\,U_t}{dt} \ . \tag{5}$$

As the projectile penetrates, the target volume swept out per unit time at angle ϕ on the sphere is given by

$$\frac{dv}{dt} = \int_0^{\phi_s} 2\pi R^2 \sin\phi \, d\phi \, V_c \cos\phi = V_c A \ , \tag{6}$$

where $2\pi R^2 \sin\phi \cos\phi \, d\phi$ represents the elemental area normal to the velocity vector V_c at an angle ϕ from the nose and ϕ_s is the submergence angle.

The rate of change of kinetic energy can be written as

$$\frac{d\,K_t}{dt} = \rho_t \frac{dv}{dt}\left(\frac{C_D}{2} V_c^2\right) = \rho_t V_c A \frac{C_D V_c^2}{2} \ , \tag{7}$$

and the change of nonkinetic energy can be written as

$$\frac{d\,U_t}{dt} = \rho_t \frac{dv}{dt} (E_*) = \rho_t\, V_c\, A\, E_* \;, \tag{8}$$

where ρ_t is the target mass density and C_D represents the instantaneous drag coefficient of the projectile. It will be shown that C_D is related to the Newtonian drag coefficient of the sphere.

The term E_* in Eq. (8) consists of two parts: a constant part E_{*p} which represents plastic work and a term E_{*e} which represents elastic energy and is significant for small penetrations. The product $\rho_t\, E_{*p}$, which accounts for plastic flow work and has the units of pressure is analogous to the Brinell hardness of the target material. However, it models the flow strength of the material at the strain rate of impact rather than at the quasi-static strain rate of a Brinell test. In reality, it is an adiabatic rather than an isothermal measurement of the yield strength because the time scale for shear heating in the material is much faster than the time scale for thermal relaxation. The quantity $\rho_t\, E_{*p}$ is therefore called the "adiabatic hardness" of the material. It will be shown later that $\rho_t\, E_{*p}$ is roughly constant as a function of velocity for each material. In Ref. 1, a formula was derived for E_{*p} based on Brinell hardness, melting temperature, and specific heat. A summary of this work is given in Chapter III.

The quantity $\rho_t\, E_{*e}$ represents the pressure produced by elastic compression of the target material. A formula for E_{*e} was also derived in Ref. 1, based on the elastic modulus, Brinell hardness, and density of the target material. At the end of this section, the method by which E_{*e} is evaluated from impact tests will be described.

Comparison of Eqs. (5), (7), and (8) with Eq. (3) shows that the decelerating force can be written as

$$F = \rho_t\, A \left(C_D \frac{V_c^2}{2} + E_{*p} + E_{*e} \right) \;. \tag{9}$$

Based on Newtonian flow considerations but allowing some freedom for comparison with experimental data, it is possible to write the force in the following form

$$F = 2\pi\rho_t R^2 \int_o^{\phi_s} \sin\phi \cos\phi \left(\frac{\alpha}{2} V_c^2 \cos^2\phi + E_{*p} + E_{*e}\right) d\phi \ . \quad (10)$$

For this analysis, the quantity α which is related to the Newtonian drag coefficient is constant and has the value $\alpha = 1$. Equation (10) can be integrated to yield

$$F = \pi R^2 \rho_t \left[\frac{\alpha}{2} V_c^2 \left(\frac{1-\cos^4\phi_s}{2}\right) + \left(E_{*p} + E_{*e}\right) \sin^2\phi_s\right] \ , \quad (11)$$

where ϕ_s is given by

$$\phi_s = \cos^{-1}(1 - z/R) \quad z \leq R$$

$$\phi_s = \pi/2 \quad z > R \ . \quad (12)$$

Note that the integration of Eq. (10) can only be done in this manner if E_{*e} is independent of ϕ . Thus, the term E_{*e} which appears in Eq. (11) is an <u>average</u> value of the elastic energy for the submergence angle ϕ_s . It is not the local value of the elastic energy per unit mass absorbed by the target. More on this point later.

With (11) for the force, the momentum equation (1) becomes

$$\frac{d}{dt} V_c = - \frac{3}{4} \frac{1}{R} \frac{\rho_t}{\rho_p} \left[\frac{\alpha}{2} V_c^2 \left(\frac{1-\cos^4\phi_s}{2}\right) + \left(E_{*p} + E_{*e}\right) \sin^2\phi_s\right] \ . \quad (13)$$

In Eq. (13), the definition for projectile mass, $m_p = (4/3)(\pi R^3 \rho_p)$, has been used. The penetration is governed by

$$\frac{dz}{dt} = V_c \; . \tag{14}$$

Equations (13) and (14) together with Eq. (12) can be integrated simultaneously to yield $z(t)$ and $V_c(t)$. The integration proceeds from $t = 0$ to $t = t_f$, the time at which V_c is reduced to 0.

2. The Newtonian drag coefficient - It was noted above that the drag force is based on the Newtonian flow approximation. In this approximation, the target material is assumed to flow in a very thin layer along the surface of the projectile. As a small volume of target material enters this layer, it suffers an abrupt change in direction as it comes in contact with the projectile. In the Newtonian model, the normal component of velocity is destroyed while the tangential component is conserved as the control volume enters the shear layer. It is the destruction of the normal component of velocity which increases the pressure at the surface of the projectile. The momentum transferred by each volume of material is

$$\frac{d}{dt}(\text{momentum}) = \rho_t \frac{dv}{dt} V_c \cos\phi \; . \tag{15}$$

The component of this momentum in the axial direction is the drag force. The contribution to the total drag force at the angle ϕ is given by

$$F_{drag} = \rho_t \frac{dv}{dt} V_c \cos^2\phi \; . \tag{16}$$

This force must be integrated over the surface area of the sphere which is in contact with the target to obtain the total drag force,

$$F_{drag} = \int_0^{\phi_s} 2\pi\rho_t \, R^2 \sin\phi \cos^3\phi \, V_c^2 \, d\phi$$

or

$$F_{drag} = \pi R^2 \sin^2\phi_s \frac{\rho_t V_c^2}{2}\left(1 + \cos^2\phi_s\right) . \tag{17}$$

The quantity $\pi R^2 \sin^2 \phi_s$ is the projected area in the direction of motion and is denoted A_ϕ. Hence,

$$F_{drag} = \left(1 + \cos^2\phi_s\right) A_\phi \frac{\rho_t V_c^2}{2} . \tag{18}$$

Upon comparing Eq. (18) with the usual definition for the drag coefficient

$$C_D = \frac{F_{drag}}{A \rho V^2/2} , \tag{19}$$

it is clear that $C_D = 1 + \cos^2\phi_s$. For the case of a fully embedded sphere, $\phi_s = \pi/2$ and therefore $C_D = 1$.

The Newtonian flow model is strictly valid only at the outer edge of the disturbed region and <u>not</u> at the projectile surface. Hence, the value of the drag coefficient deduced above must be modified to account for centrifugal effects in the distrubed layer. It can be shown that when centrifugal effects are included, the pressure at the surface of the projectile is given by

$$P = \rho_t V_c^2 \left(\cos^2\phi - \sin^2\phi \frac{\delta}{R}\right) , \tag{20}$$

where δ is the thickness of the layer. The layer thickness can be estimated using a conservation of mass statement together with an assumption for the velocity profile. The simplest assumption is that the velocity is uniform in the layer. In this case, it can be shown that $\delta/R = 1/2$ and, further, that $C_D = 1/2$ for a fully submerged sphere. This is the same value as that obtained from the inertial term in Eq. (11) when $\alpha = 1$ and $\phi_s = \pi/2$. The value of $C_D = 1/2$ provides a very good fit to the data for a wide range of velocities and materials as will be demonstrated shortly. The Newtonian approximation for the drag term probably works as well as it does because the strength of the target material confines the region of plastic flow to a narrow layer close to the surface of the projectile - a basic assumption of the Newtonian model.

3. Elastic energy per unit mass - E_{*e} - In Ref. 1, the term E_{*e} does not appear in the momentum equation. Instead, the elastic energy was included in the model as a velocity cutoff during the integration. This velocity cutoff was denoted by V_*, and it was assumed that at this velocity all the remaining kinetic energy of the projectile could be elastically absorbed by the target with no further permanent penetration. A disadvantage of using this approach is that V_* depends not only on the physical properties of the target but also on the density of the projectile. The quantity E_{*e}, however, depends only on the physical properties of the target material and is therefore a more convenient parameter to use.

During the course of this program, experimental and theoretical evidence has been developed to show that E_{*e} depends on the dimensionless penetration depth $z/2R$. However, in analyzing experimental data, only integral quantities such as projectile mass, radius, velocity, kinetic energy, and final penetration depth are available. Empirical information about the time dependence of velocity and penetration are generally not available. Hence, the value of E_{*e}, which is a local property, can only be deduced from impact data in an integral sense. The method by which this can be done is as follows.

Consider the equation for the rate at which work is done on the target (Eq. (5)). This equation can be integrated to give the total work done on the target

$$W_t = \int_0^p \rho_t \left[\frac{C_D}{2} V_c^2 + E_{*p} + E_{*e}(z)\right] A dz \quad , \tag{21}$$

where p is the final penetration. The integral can be written as follows

$$W_t = \int_0^p \rho_t A \frac{C_D}{2} V_c^2 \, dz + \rho_t \left[E_{*p} + \overline{E_{*e}}(p)\right] v(p) \quad , \tag{22}$$

where

$$\overline{E_{*e}}(p) \equiv \frac{1}{v(p)} \int_0^p E_{*e}(z) A dz \quad . \tag{23}$$

The quantity $\overline{E_{*e}}$ (p) represents the average value of E_{*e} over the trajectory and only depends on the final value of the penetration p . It will be shown shortly that E_{*p} is constant. Hence the quantity $E_{*p} + \overline{E_{*e}}$ in Eq. (22) is solely a function of p . Therefore, for each impact test a unique value of $E_* = E_{*p} + \overline{E_{*e}}$ can be found which when integrated via Eqs. (13) and (14) gives the correct penetration depth p for the given impact velocity V_{c_0} .

It will be shown that $E_*(p)$ deduced in this manner can be interpreted as the superposition of two components; a constant component, E_{*p} , for relatively large penetrations and a depth-dependent component, $\overline{E_{*e}}$, for shallow penetrations. It was shown in Ref. 1. that $\overline{E_{*e}}$ has the following form

$$\overline{E_{*e}} \cong k\ (p/2R)^N \ , \qquad (24)$$

where k and N are constants. The exponent N is approximately -.75 for most metals. For other materials, N is between -.75 and -1.5 .

To summarize, impact data (crater depth measurements) are used to deduce $E_*(p)$. The constant portion of E_* obtained for large penetrations is E_{*p} . For shallow penetrations, Eq. (24) is used to evaluate the constants k and N which best match the data. In this way $\overline{E_{*e}}$ is obtained.

Note that this procedure requires knowledge of the final penetration. In the general case when p is not known a priori, the local value of E_{*e} and not the average value must be used. The local value can be obtained by differentiating Eq. (23)

$$E_{*e}(z) = \overline{E_{*e}}(p) + \frac{v(p)}{A(p)} \frac{d}{dp} \left[\overline{E_{*e}}(p)\right] . \qquad (25)$$

This value can then be used in the integration of the momentum equation. $\overline{E_{*e}}$ (note the bar), because it is constant over the trajectory and depends only on the final penetration p , is considerably more convenient to use than the local value of E_{*e} . It will be used exclusively in this report. The bar will be dropped from the notation, and the local value of E_{*e} will no longer be used. This approach permits the

integration of Eq. (10) as was noted earlier.

B. Experimental Program

This section describes the experimental program which was used to evaluate the impact properties E_{*p} and E_{*e} of the various target materials. It contains a brief description of the A.R.A.P. Impact Facility, a summary of the test matrix, and an illustration of the method by which E_{*p} and E_{*e} are evaluated from impact data.

1. A.R.A.P. impact facility - Figure 2 depicts schematically the A.R.A.P. Impact Facility. This facility consists of a mounted rifle and enclosed test tube and test chamber. Two guns* were used for this program; a Winchester .270 caliber smooth bore rifle and a Power Line 880 Air Gun.

The Winchester is permanently mounted to a fixed support and is bore-sighted on the target. Cartridges are hand loaded using Hercules 2400 gunpowder. The projectiles are 0.250-inch diameter balls made of either tungsten carbide or chrome steel (AISI 52100). The ball is fired using a Lexan sabot which is manufactured in four sections. The sabot separates aerodynamically after leaving the muzzle and is stripped from the flight path ahead of the test chamber. The velocity range for steel and tungsten carbide projectiles is 700 to 5,500 feet per second. Lighter projectiles have been fired at velocities up to 6,600 feet per second.

The Power Line gun is utilized to extend the low velocity range of the facility. The gun can fire 0.156 and 0.172-inch diameter tungsten carbide and chrome steel balls in a velocity range between 160 and 740 feet per second.

Projectile velocity is measured using a Schmidt-Weston Chronograph. Two light screens, separated by a fixed distance, sense the passage of the projectile using photo-resistor elements. The flight path is illuminated by light which passes through slits in the shelf located in the chamber. The shadow produced by the projectile on the light screens triggers and then stops a counter. Digital readout of the velocity is provided on a display board.

Targets are mounted in a cylindrical tube at the aft end of the test chamber. Most of the targets were circular disks

*The Impact Facility also includes both a Weatherby .460 rifle and a 30-06 rifle, although these rifles were not used for this test program.

A.R.A.P. IMPACT FACILITY

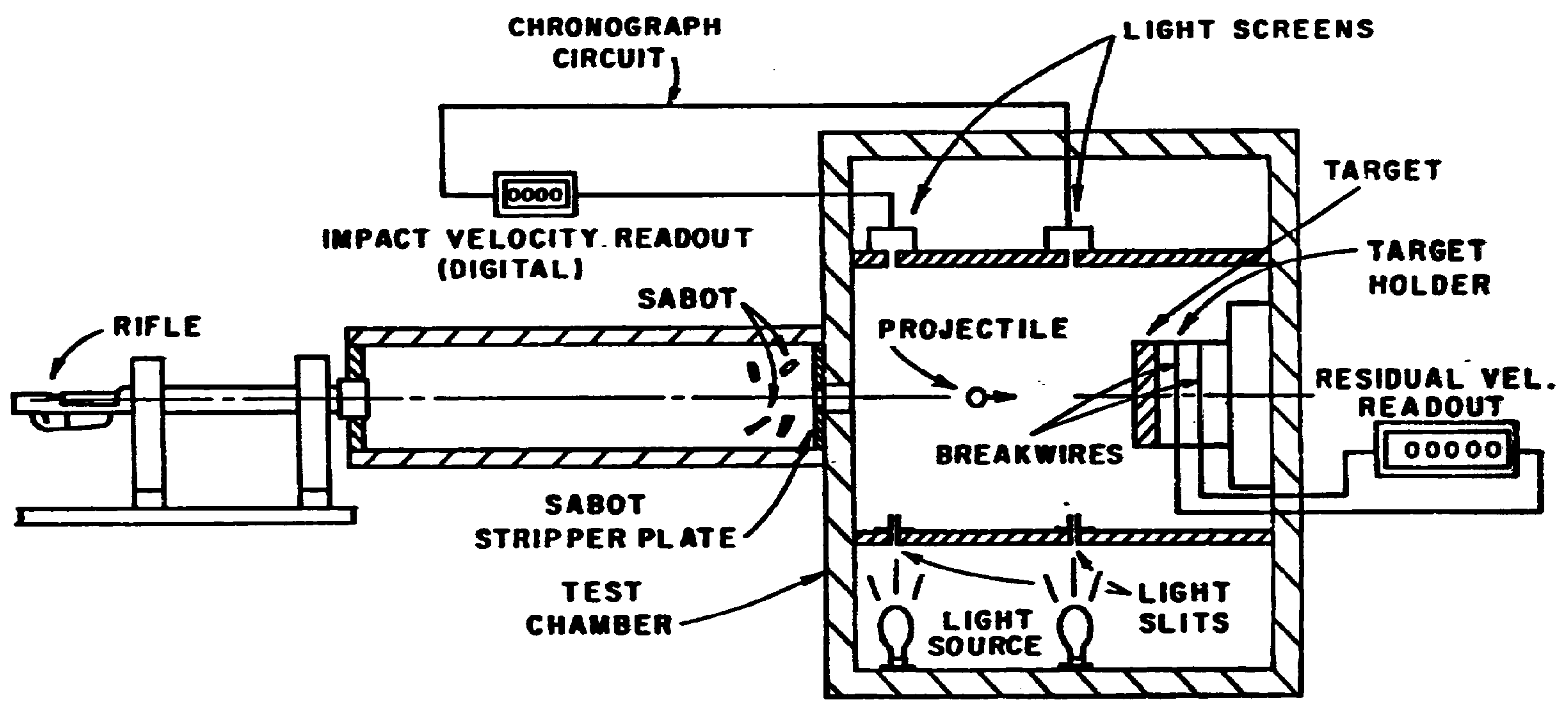

Gun	Projectile	Velocity range
Winchester .270 Smooth bore rifle	Dia. ≤ .25" WC, Al Pb, Glass, Steel	700-6600 fps
Power Line 880 Air gun	Dia. ≤ .172" WC, Steel	160-740 fps

Figure 2

with a nominal diameter of 6 inches and a thickness of 1 inch. Other shapes and sizes, however, can be easily accommodated. The target is restrained on the front by an annular steel ring fastened to the cylindrical steel tube and on the rear by a 1-inch thick wood disk and several steel disks held in place by a 1-inch steel screw.*

Documentation for each test is available and a summary of the data is contained in Appendix A. Pre-test measurements include thickness, diameter and mass of target, mass and diameter of the projectile and photographs of the undamaged target. Post-test measurements include target crater depth - using a dial indicator, and diameter, target mass, and projectile mass and diameter. Photographs were also taken of the damaged target.

2. Test program - A total of 181 impact tests were conducted on 16 different target materials. These materials include seven metals, four alloys, two plastics, two ceramics and one composite. Table 1 provides a description of these materials and a summary of the results. A tabulation of the data is contained in Appendix A.

The limits for the velocity range over which each material was tested are based on the following criteria. The lower limit was set by the chronograph sensitivity which is approximately 150 feet per second. The upper limit of the velocity range was set to limit maximum crater depth to approximately half the target thickness in order to minimize backface effects.

Note that for most of these materials, a free fall test was also conducted by dropping a 0.50-inch diameter chrome steel ball from the ceiling of the laboratory onto the target. From a height of approximately 14 feet, the impact velocity was computed to be 28 feet per second.

3. Evaluation of E_{*p} and E_{*e} - For each impact test, a value of E_* was computed using Eqs. (13) and (14) which gave the correct value of penetration depth, p, for the impact velocity. Figure 3 shows the results of these computations for the soft aluminum target. The computed E_* is shown as a function of the normalized penetration p/d_o,

*The breakwires shown in Figure 2 are used to measure projectile residual velocity for finite thickness targets. The wires were not used for this test program.

TABLE 1

MATERIALS CHARACTERIZATION TEST PROGRAM							
TARGET MATERIAL	DESCRIPTION	# of Tests	Velocity Range	Spec Grav	E_{*p}	$E_{*e}=k(p/d_o)^N$ k	N
			ft/sec		Btu/lbm		
Acrylic	American Cyanamid-acrylite	14	162-1397	1.19	110	190	-1.5
Aluminum	1100-F Plate	11	28-1701	2.73	84	0	-
Aluminum	5083-Rockwell B-75	7	196-2326	2.74	245	15.1	-.75
Cadmium	99.9% Pure, Open Cast	12	28-1491	8.81	29	0	-
Copper	Hot Rolled ETP Plate	12	28-2483	9.01	38	0	-
Glass	Corning Pyrex 7740	8	192-1087	2.18	105	0	-
Iron	Class 40 - Gray	13	28-2892	7.13	121	7	-.75
Kevlar	Rigid Composite of Aramid Fibers and Epoxy Resin	12	198-2059	1.23	171	24.9	-1.5
Lead	99.9% Pure, Open Cast	18	28-1174	11.3	3.5	0	-
Polycarbonate	General Electric - Lexan	9	162-1293	1.21	101	106	-1.1
Salt	Polycrystalline Sodium Chloride	16	28-1282	1.99	86	0	-
Silicon	Porous with .5% Fe	4	916-1381	2.1	184	-	-
Steel	1020 - hot rolled plate	12	28-4336	7.86	141	8.9	-.75
Steel	Rolled Homogeneous Armor	7	193-2082	7.83	203	19	-.75
Titanium	Ti-6Aℓ-4V	14	259-3015	4.48	328	7.1	-.75
Zinc	99.9% Pure, Open Cast	12	28-2680	7.19	62	0	-
		181					

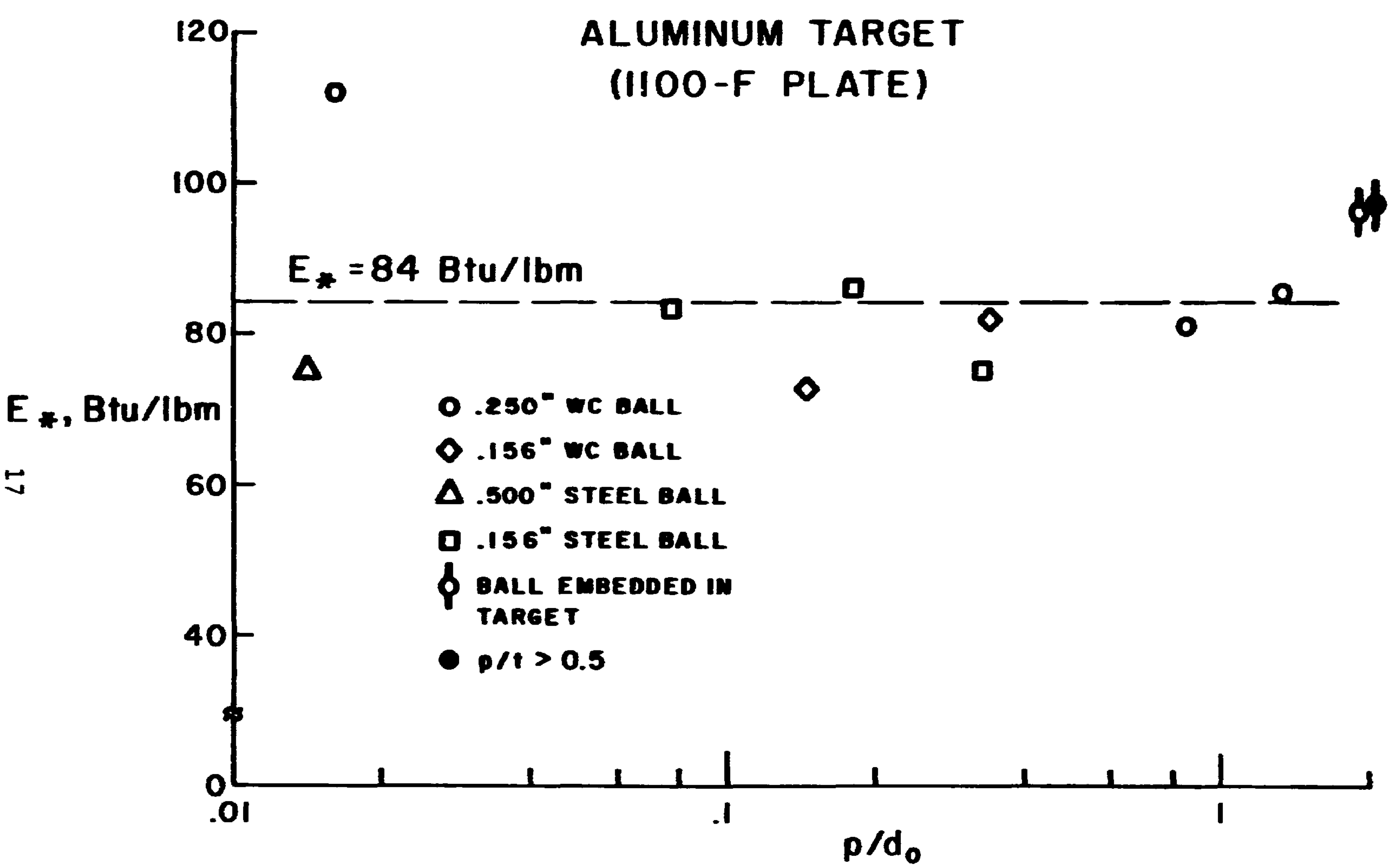
ALUMINUM TARGET
(1100-F PLATE)
E* =84 Btu/lbm
E*, Btu/lbm
120
100
80
60
40
0
.01
.1
1
p/do
O .250" WC BALL
◇ .156" WC BALL
△ .500" STEEL BALL
□ .156" STEEL BALL
BALL EMBEDDED IN TARGET
● p/t > 0.5

Figure 3

where d_o is the initial diameter of the ball. For this material, the values of E_* fall within a narrow band, and the average value of the band is approximately 84 Btu/lbm. All of the E_* values fall within 15% of the average, except for one shallow penetration data point which was relatively inaccurate.

As noted earlier, for each material an equation of the form

$$E_* = E_{*p} + E_{*e} = E_{*p} + k\ (p/d_o)^N , \qquad (26)$$

was fit to the E_* computations. The functional form of E_{*e} is based on the static experiments described in Ref. 1. Therefore, for soft aluminum, $E_{*p} = 84$ Btu/lbm and $E_{*e} = 0$. Appendix B contains the E_* evaluations for the remaining materials.

C. Data Theory Correlations

After E_{*p} and E_{*e} have been evaluated for a given target material, the Integral Theory of Impact can be used to compute the depth of penetration for any impact velocity. The procedure is simply to differentiate $E_{*e}(p)$, evaluate $E_{*e}(z)$ according to Eq. (25) and integrate Eq. (13) and Eq. (14) simultaneously. In this section, the impact data for each material are presented and compared to the results of such computations. Data are shown for both tungsten carbide and chrome alloy steel (AISI-52100) balls.

In each of the tests, except those noted "ball broken", there was no measurable plastic deformation of the ball after impact. For most of the tests, the ball rebounded from the target. Hence, the crater depth could be measured directly using a dial indicator. In some tests, however, the ball remained embedded in the target. For these cases, the dial indicator was used to locate the position of the top of the ball and the ball diameter was added to obtain crater depth.

1. Metals - The results for six metal targets are shown in Figures 4 - 9. Each of the targets was a circular disk with a nominal diameter of six inches. The nominal thickness of each target was one inch, except for a few of the lead targets which were two-inches thick. With the exception of the cast iron target, these metals are relatively soft (E_{*p} < 100 Btu/lbm) and inelastic ($E_{*e} = 0$).

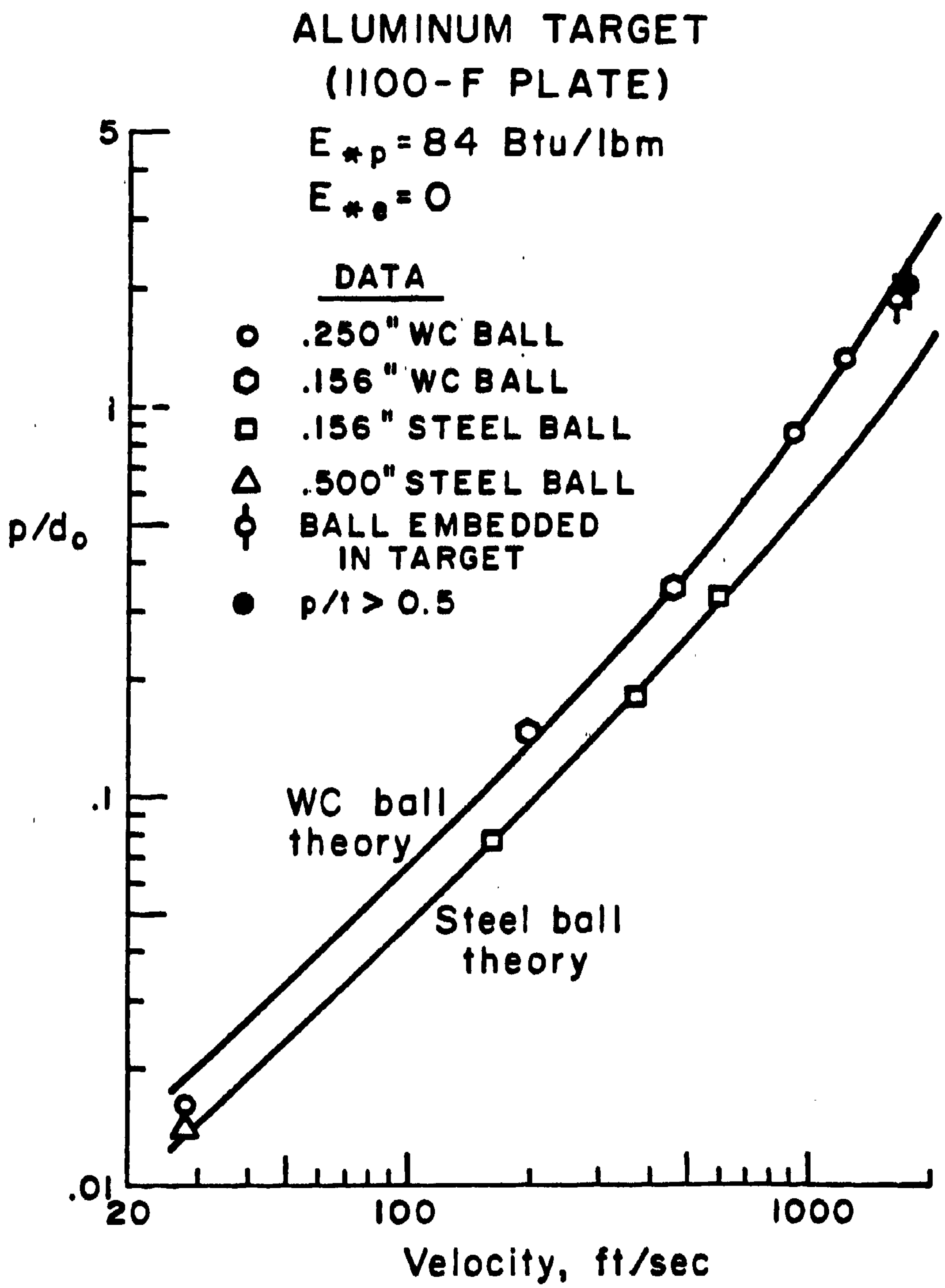
ALUMINUM TARGET
(1100-F PLATE)
E_{*p} = 84 Btu/lbm
E_{*e} = 0
DATA
.250" WC BALL
.156" WC BALL
.156" STEEL BALL
.500" STEEL BALL
BALL EMBEDDED IN TARGET
p/t > 0.5
WC ball theory
Steel ball theory
p/d$_o$
5
1
.1
.01
20
100
1000
Velocity, ft/sec

Figure 4

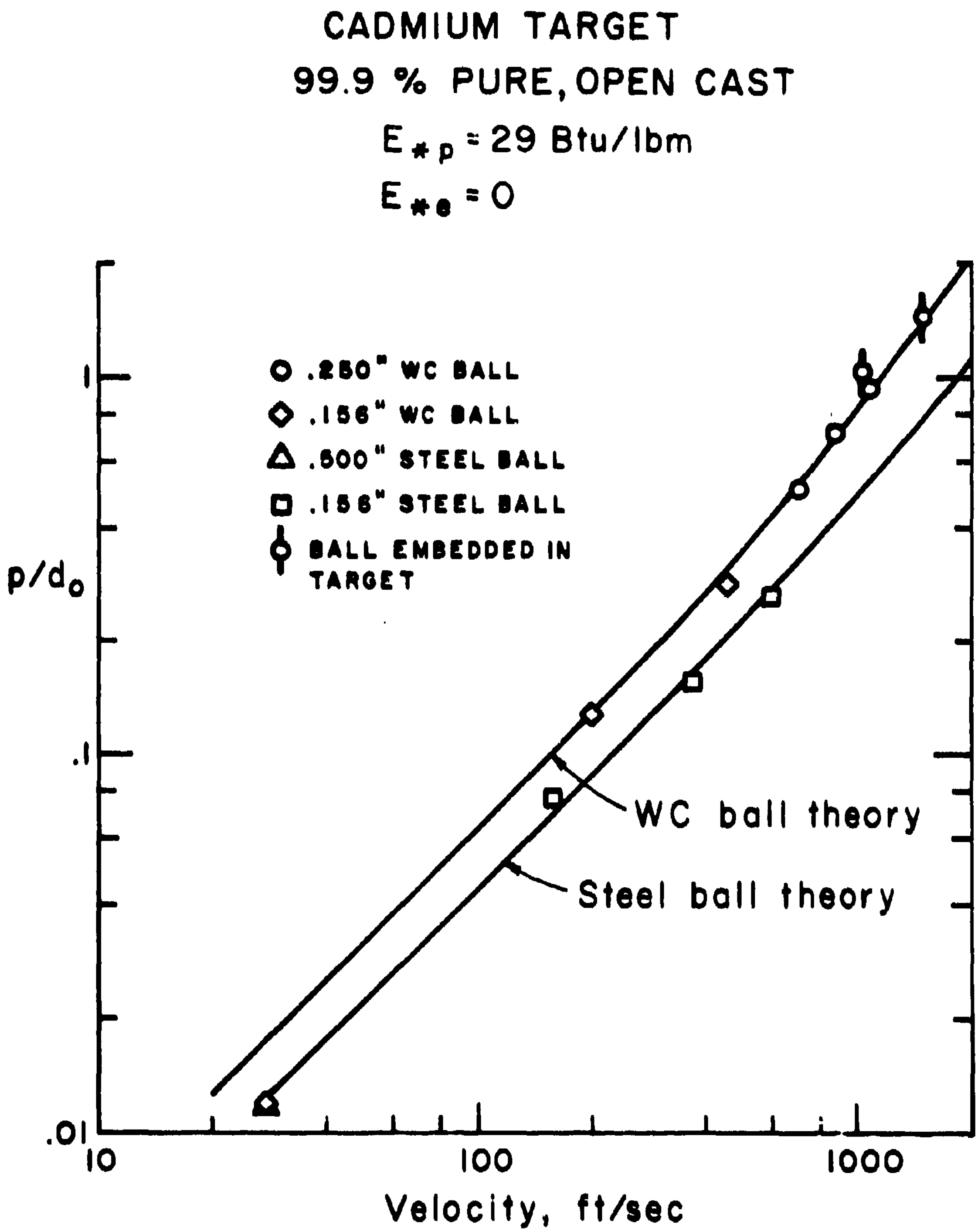
CADMIUM TARGET
99.9 % PURE, OPEN CAST
$E_{*p} = 29$ Btu/lbm
$E_{*e} = 0$
.250" WC BALL
.156" WC BALL
.500" STEEL BALL
.156" STEEL BALL
BALL EMBEDDED IN TARGET
p/d_o
1
.1
.01
10
100
1000
Velocity, ft/sec
WC ball theory
Steel ball theory

Figure 5

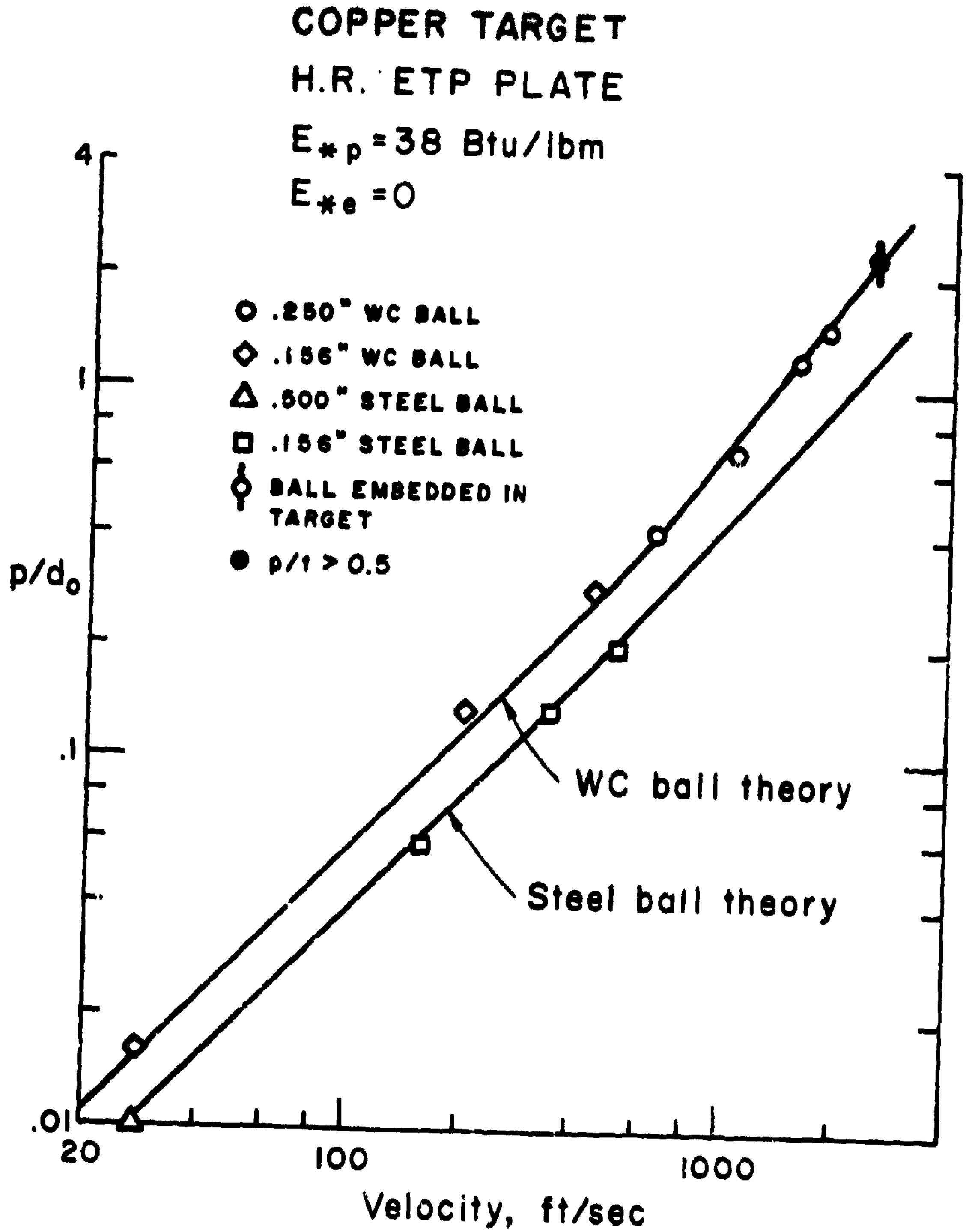

COPPER TARGET
H.R. ETP PLATE
E_{*p} = 38 Btu/lbm
E_{*e} = 0
.250" WC BALL
.156" WC BALL
.500" STEEL BALL
.156" STEEL BALL
BALL EMBEDDED IN TARGET
p/t > 0.5
p/d_o
4
1
.1
.01
20
100
1000
WC ball theory
Steel ball theory
Velocity, ft/sec

Figure 6

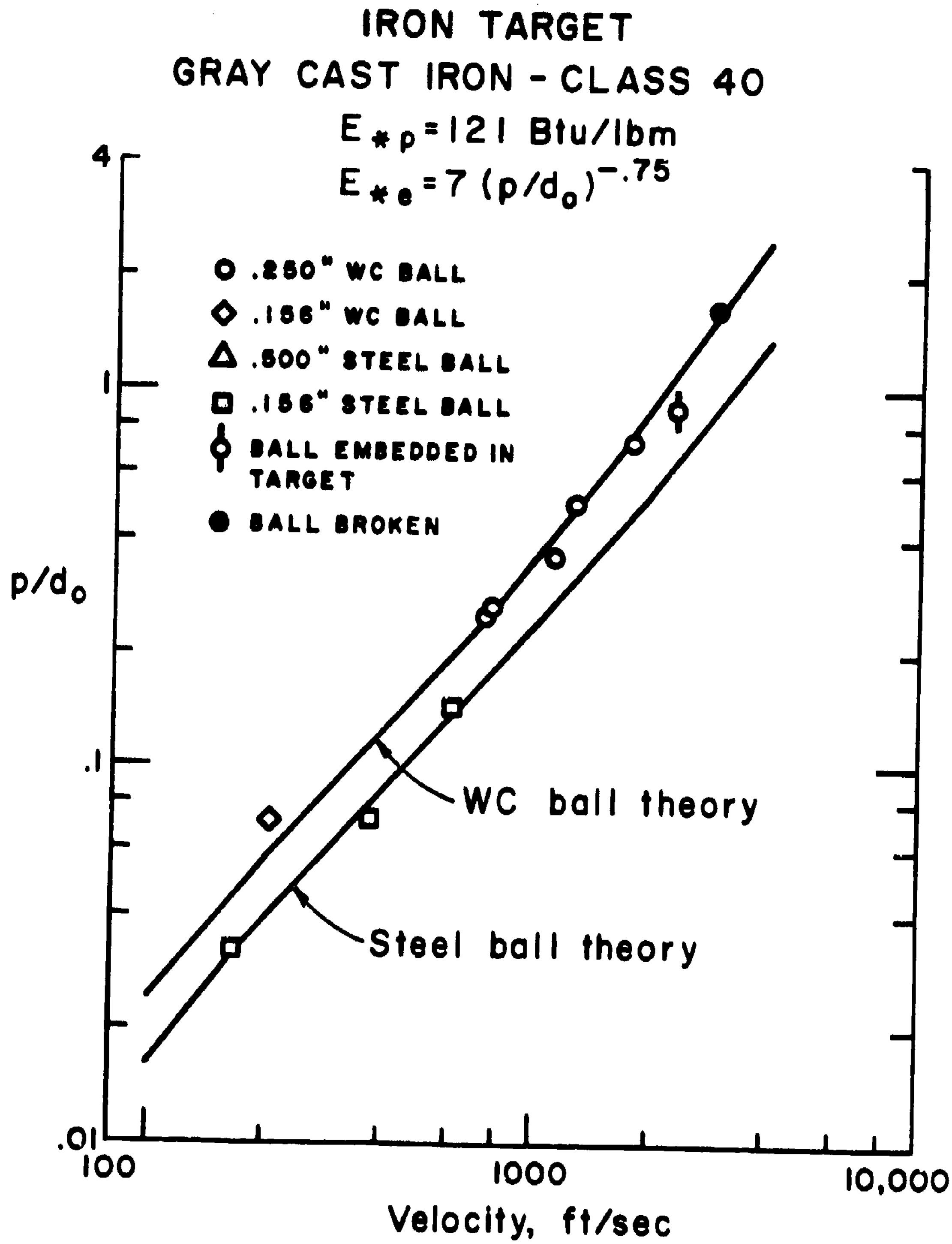
IRON TARGET
GRAY CAST IRON - CLASS 40
E*p = 121 Btu/lbm
E*e = 7 (p/do)^-.75
.250" WC BALL
.156" WC BALL
.500" STEEL BALL
.156" STEEL BALL
BALL EMBEDDED IN TARGET
BALL BROKEN
p/do
4
1
.1
.01
100
1000
10,000
Velocity, ft/sec
WC ball theory
Steel ball theory

Figure 7

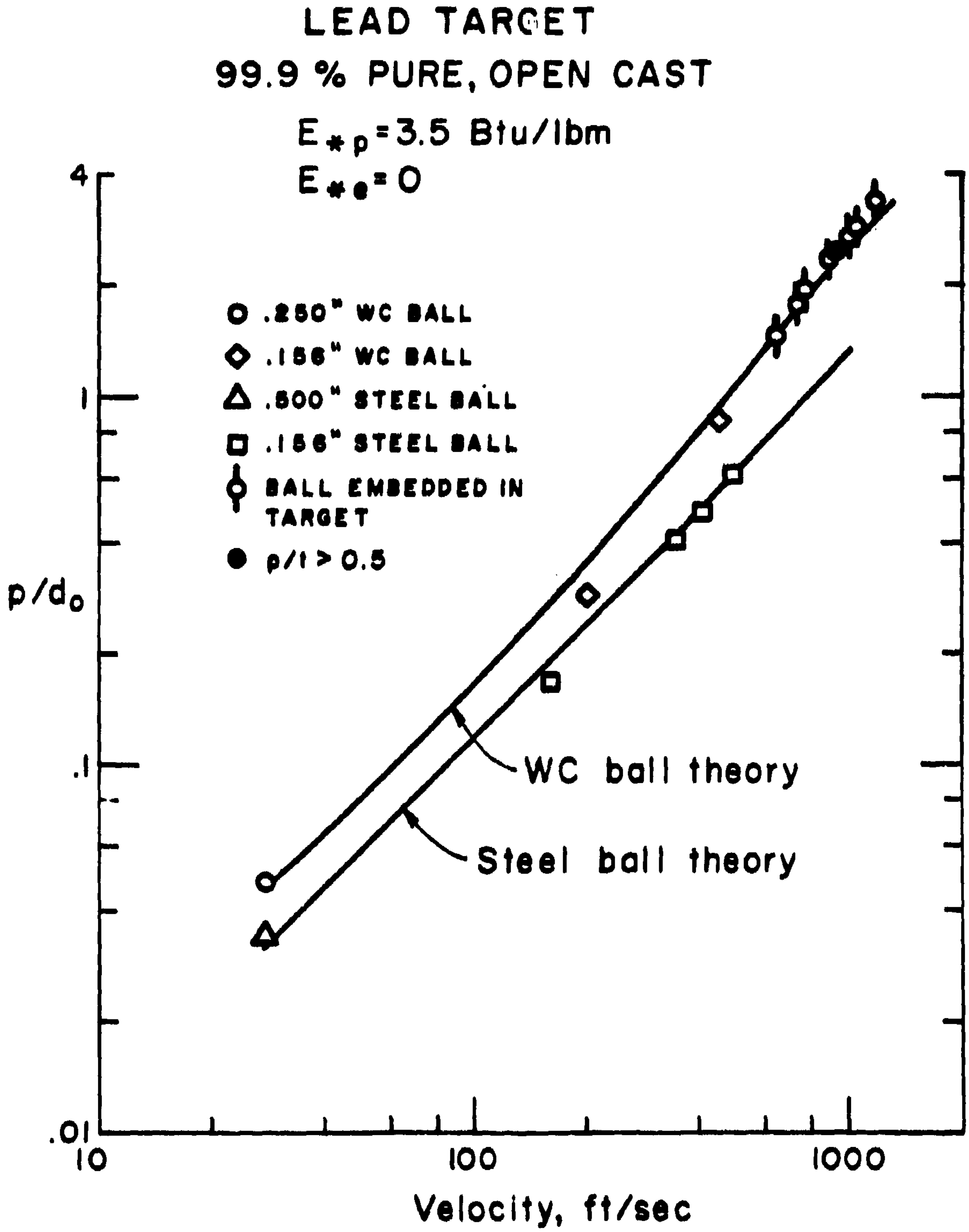
LEAD TARGET
99.9 % PURE, OPEN CAST
E*p=3.5 Btu/lbm
E*e=0
.250" WC BALL
.156" WC BALL
.500" STEEL BALL
.156" STEEL BALL
BALL EMBEDDED IN TARGET
p/t > 0.5
p/d0
WC ball theory
Steel ball theory
4
1
.1
.01
10
100
1000
Velocity, ft/sec

Figure 8

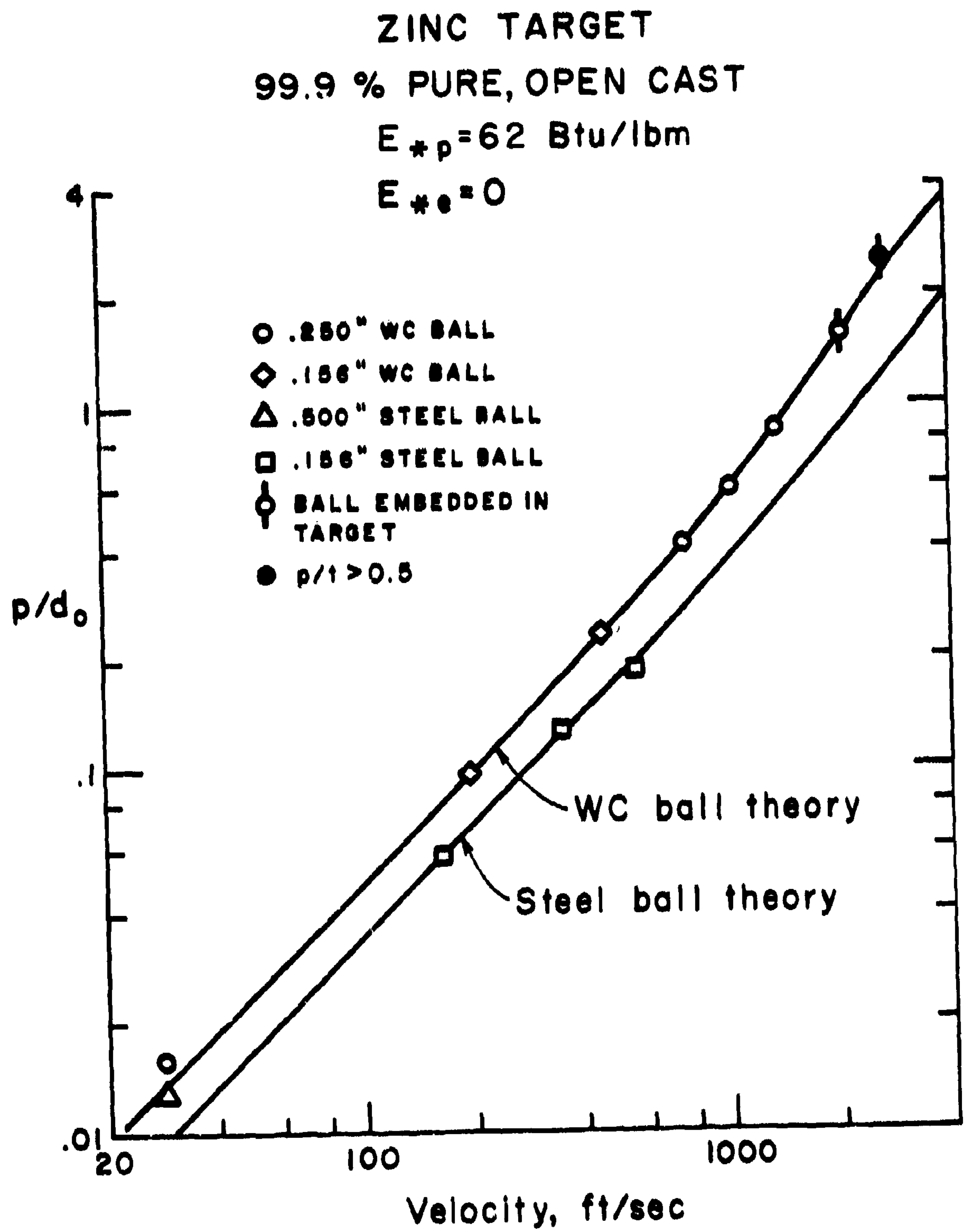
ZINC TARGET
99.9 % PURE, OPEN CAST
E*p=62 Btu/lbm
E*e=0
.250" WC BALL
.156" WC BALL
.500" STEEL BALL
.156" STEEL BALL
BALL EMBEDDED IN TARGET
p/t > 0.5
p/d0
4
1
.1
.01
20
100
1000
Velocity, ft/sec
WC ball theory
Steel ball theory

Figure 9

In addition to these metals, four tests were conducted on silicon targets. The silicon was in the form of relatively large chunks - major dimension approximately four to five inches - obtained as a byproduct of steel processing. The samples were porous and contained a small amount of iron impurities. In order to test this material, each of the four largest pieces was cast in concrete, and the front surface of each piece was ground flat. Suitable material was available for only four tests. The average value of E_* for these tests was 134 Btu/lbm. The data were insufficient to determine E_{*e} .

2. <u>Metal alloys</u> - Four metal alloys were tested, and the results are shown in Figures 10-13. The aluminum alloy was designated 5083 Aluminum, but its temper was unknown. However, it had a static hardness of Rockwell B-75. The targets had a rectangular cross-section, 3.9" by 4.5", and were one-inch thick. This alloy has a relatively high value of E_{*p} = 245 Btu/lbm and also has a moderate value of E_{*e} for small penetrations.

Two steels were tested - a mild steel (1020 - hot rolled) and an armor steel (rolled homogeneous steel armor). The mild steel targets were six-inch diameter disks; the armor steel targets were 3.9" by 4.5" rectangles. All steel targets were one-inch thick. The value of E_{*p} varied from 141 Btu/lbm for the mild steel to 203 Btu/lbm for the armor steel. Both steels have moderate E_{*e} components with the armor steel having approximately twice the value of the mild steel. Note that the tungsten carbide balls were broken for impact velocities in excess of 2,000 feet per second. However, the correlations with nondeforming ball theory are still fairly good. This is because the tungsten carbide exhibits very little deformation prior to brittle fracture and not more than three or four pieces are formed for velocities of 2,000 feet per second. However, when the ball is shattered into many small pieces, the rigid ball theory overpredicts the penetration as is evident in Figure 11 for velocities in excess of 4,000 feet per second.

The titanium alloy (Figure 13) was Ti-6Aℓ-4V. The targets had a square cross section 4.375" on a side and a nominal thickness of 0.68 inches. This alloy has the highest value of E_{*p} of any of the metals and alloys tested. It also has a moderate value of E_{*e} .

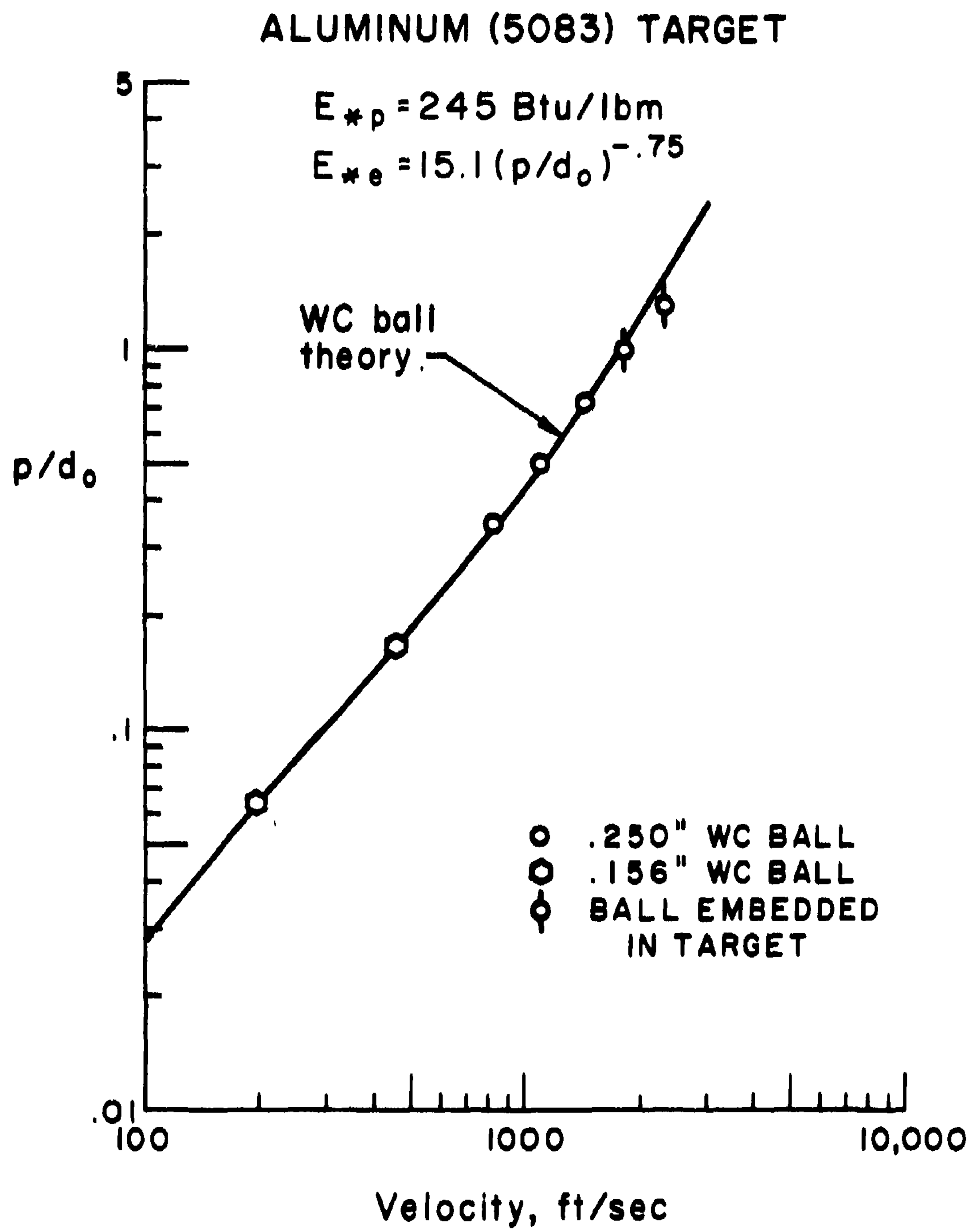
ALUMINUM (5083) TARGET
E*p = 245 Btu/lbm
E*e = 15.1 (p/do)^-.75
WC ball theory
5
1
.1
.01
p/do
100
1000
10,000
Velocity, ft/sec
.250" WC BALL
.156" WC BALL
BALL EMBEDDED IN TARGET

Figure 10

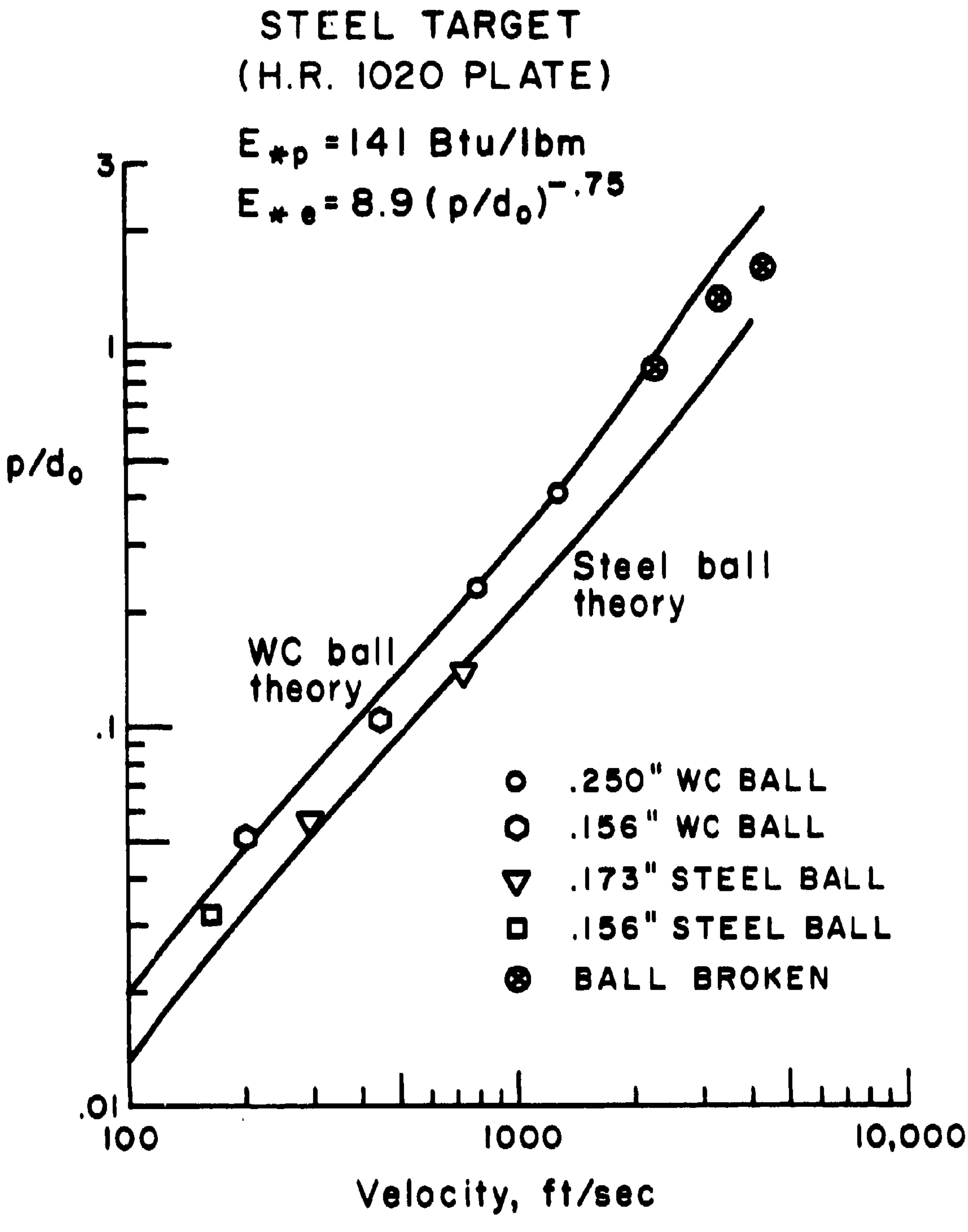
STEEL TARGET
(H.R. 1020 PLATE)
E*p = 141 Btu/lbm
E*e = 8.9 (p/do)^-.75
p/do
3
1
.1
.01
100
1000
10,000
Velocity, ft/sec
WC ball theory
Steel ball theory
.250" WC BALL
.156" WC BALL
.173" STEEL BALL
.156" STEEL BALL
BALL BROKEN

Figure 11

STEEL TARGET
ROLLED HOMOGENEOUS STEEL ARMOR

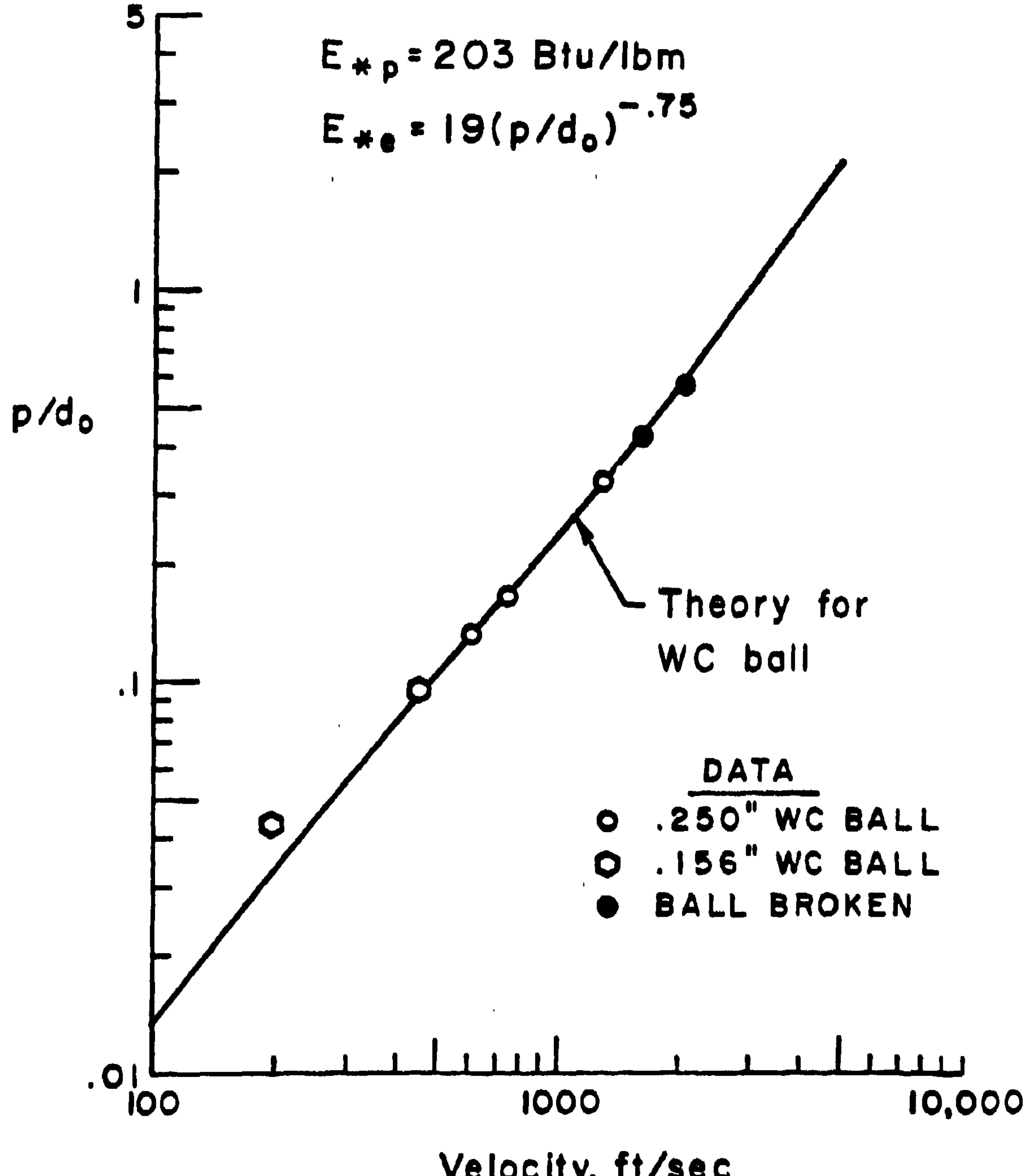

Figure 12

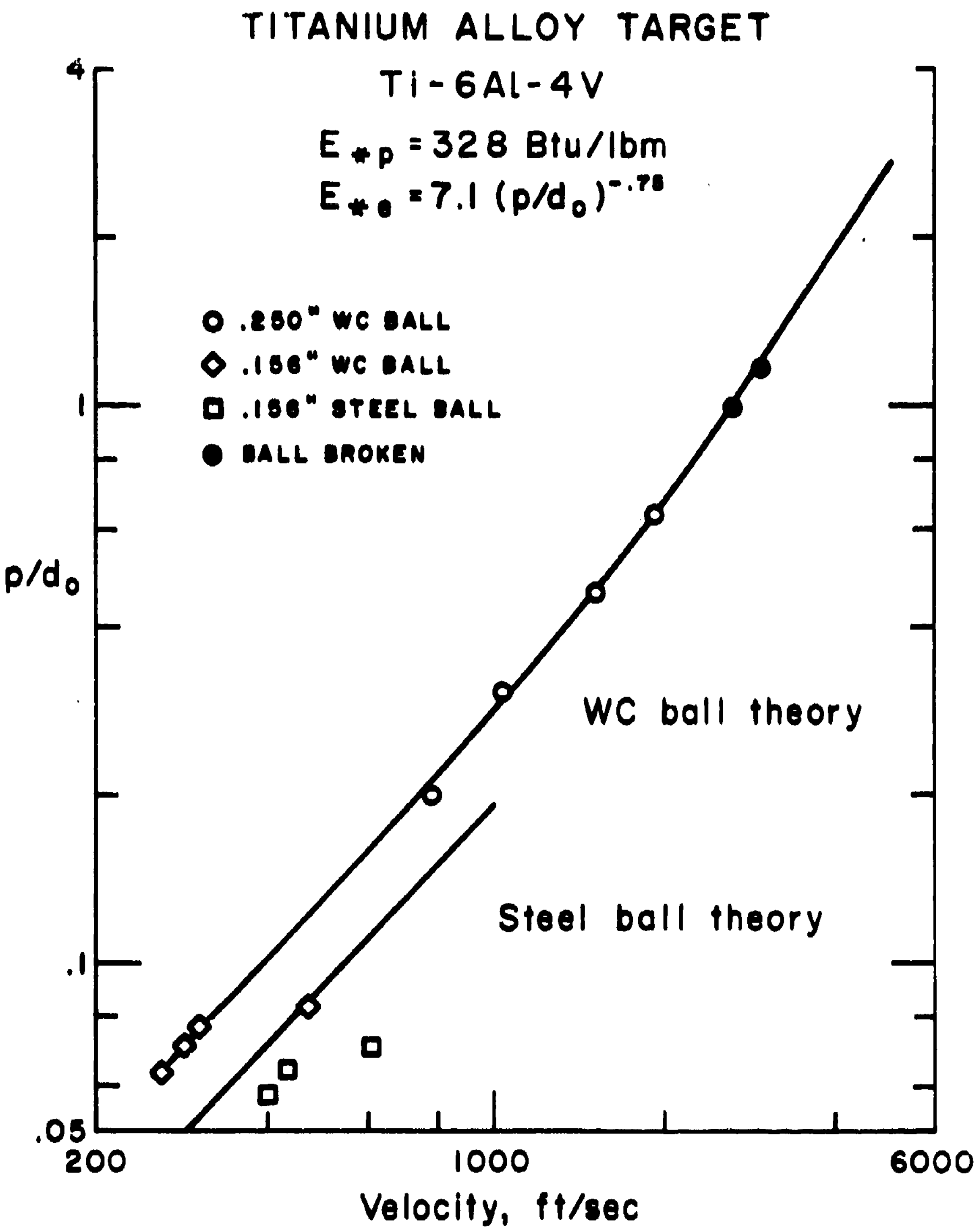

TITANIUM ALLOY TARGET
Ti-6Al-4V
E_{*p} = 328 Btu/lbm
E_{*e} = 7.1 $(p/d_o)^{-.78}$
.250" WC BALL
.156" WC BALL
.156" STEEL BALL
BALL BROKEN
WC ball theory
Steel ball theory
p/d_o
4
1
.1
.05
200
1000
6000
Velocity, ft/sec

Figure 13

3. Plastics - Two plastics - acrylic and polycarbonate - were tested, and the results are shown in Figures 14 and 15. Targets for each material were six-inch diameter disks and one-inch thick. The acrylic was Acrylite and is produced by the American Cyanamid Company. The polycarbonate was Lexan, produced by the General Electric Company. These materials have similar impact properties. The values of E_{*p} are not high (~ 100 Btu/lbm) and differ by only about 10%. They each exhibit large values for E_{*e}. For penetrations less than one ball diameter, the E_{*e} component is larger than E_{*p}. Despite the similarities in the impact properties, the appearance of the damaged targets is quite different. The acrylic is brittle and exhibits large cracks over most of its surface as well as backface spall. The polycarbonate is much more ductile, and the damage is localized to a small region in the vicinity of the ball.

4. Ceramics - Two ceramics - glass and salt - were tested, and the results are shown in Figures 16 and 17. The glass targets were Corning Pyrex 7740 cast mirror blanks, six inches in diameter and one-inch thick. This material is extremely brittle and, as a result, there is considerable scatter in the crater depth measurements.

The salt targets which were cut from large blocks of polycrystalline sodium chloride were six-inch diameter, one-inch thick disks. This material is also quite brittle and exhibits considerable scatter in the data. However, a value of E_{*p} = 86 Btu/lbm appears to provide good correlation with the data.

5. Composite - Figure 18 shows the results for the Kevlar target. This composite is a woven fabric produced by DuPont and consists of aramid (Kevlar) fibers treated with an epoxy resin and molded into a rigid sheet. The sheets which are approximately 3/8" thick were cut into four-inch squares. Targets were made by stacking three pieces. No bonding between layers was employed. Kevlar has a value of E_{*p} comparable to steel and a large component of E_{*e}.

D. Summary of Qualification Tests

A summary of the value of E_{*p} and the constants needed to evaluate E_{*e} is contained in Table 1. In general, the Integral Theory of Impact when used with these two properties provides very good correlation with the data for the wide range of materials

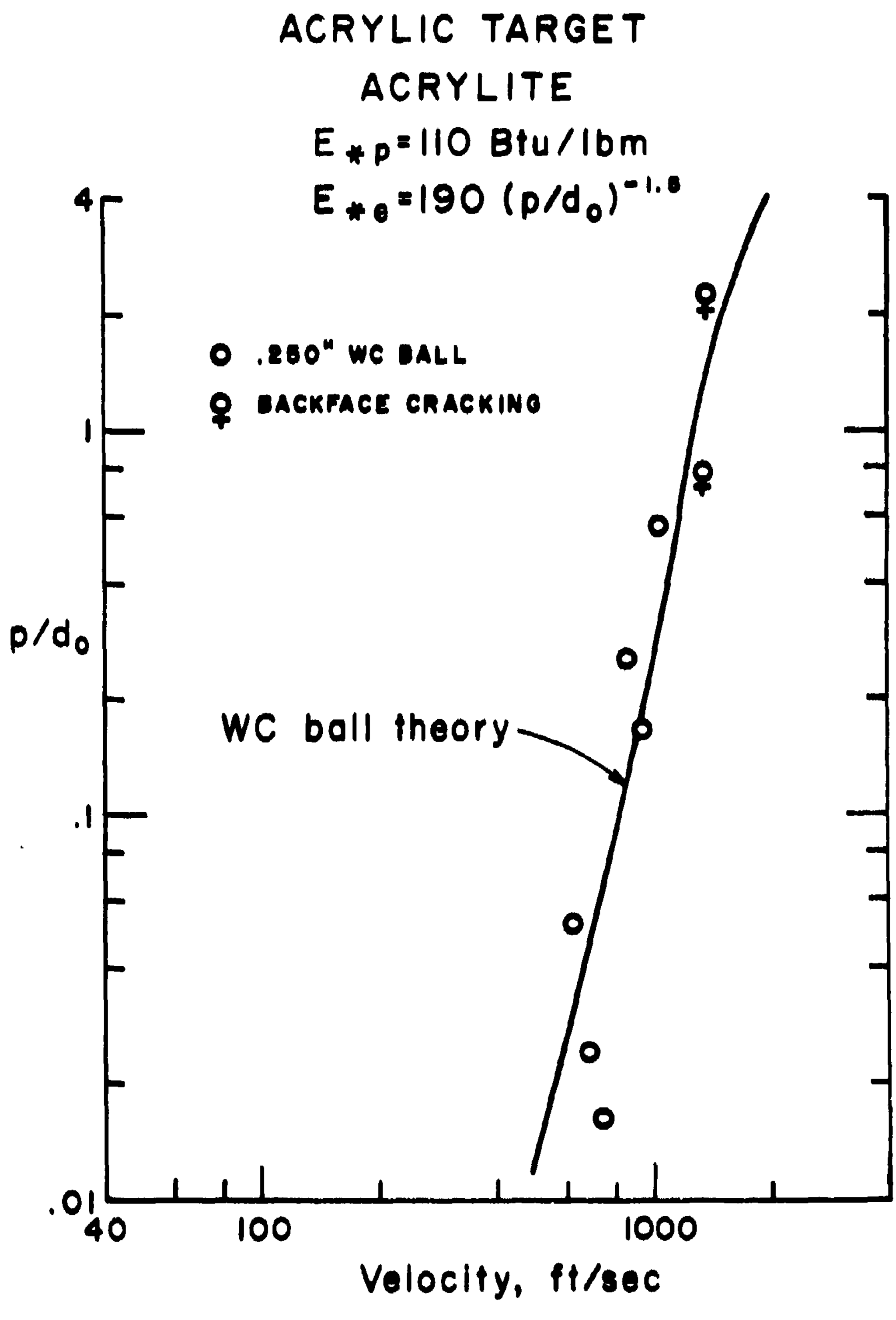
ACRYLIC TARGET
ACRYLITE
E_{*p}=110 Btu/lbm
E_{*e}=190 $(p/d_o)^{-1.8}$
.250" WC BALL
BACKFACE CRACKING
WC ball theory
p/d_o
4
1
.1
.01
40
100
1000
Velocity, ft/sec

Figure 14

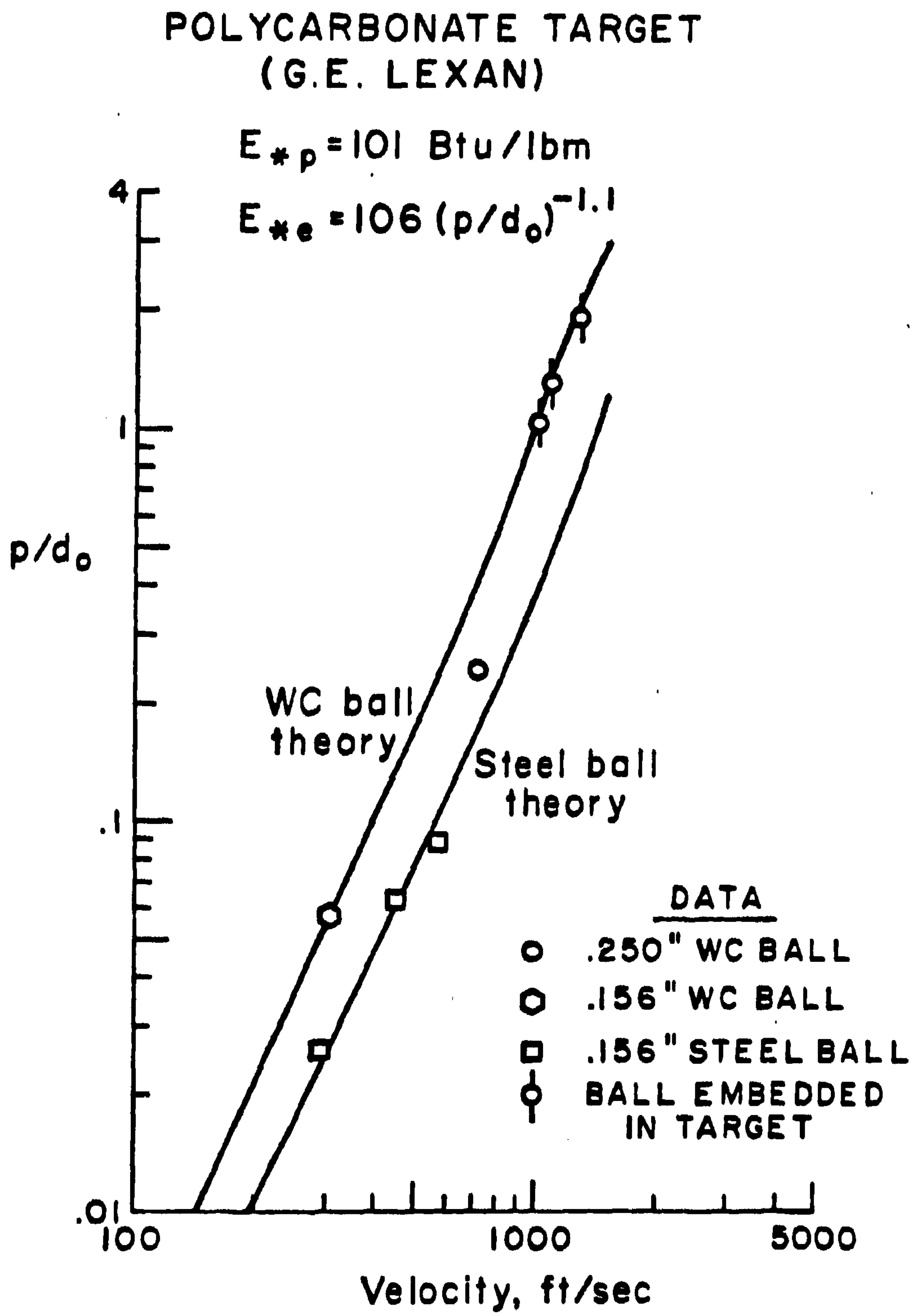

POLYCARBONATE TARGET
(G.E. LEXAN)
E_{*p} = 101 Btu/lbm
$E_{*e} = 106\,(p/d_o)^{-1.1}$
4
1
.1
.01
p/d_o
WC ball theory
Steel ball theory
DATA
.250" WC BALL
.156" WC BALL
.156" STEEL BALL
BALL EMBEDDED IN TARGET
100
1000
5000
Velocity, ft/sec

Figure 15

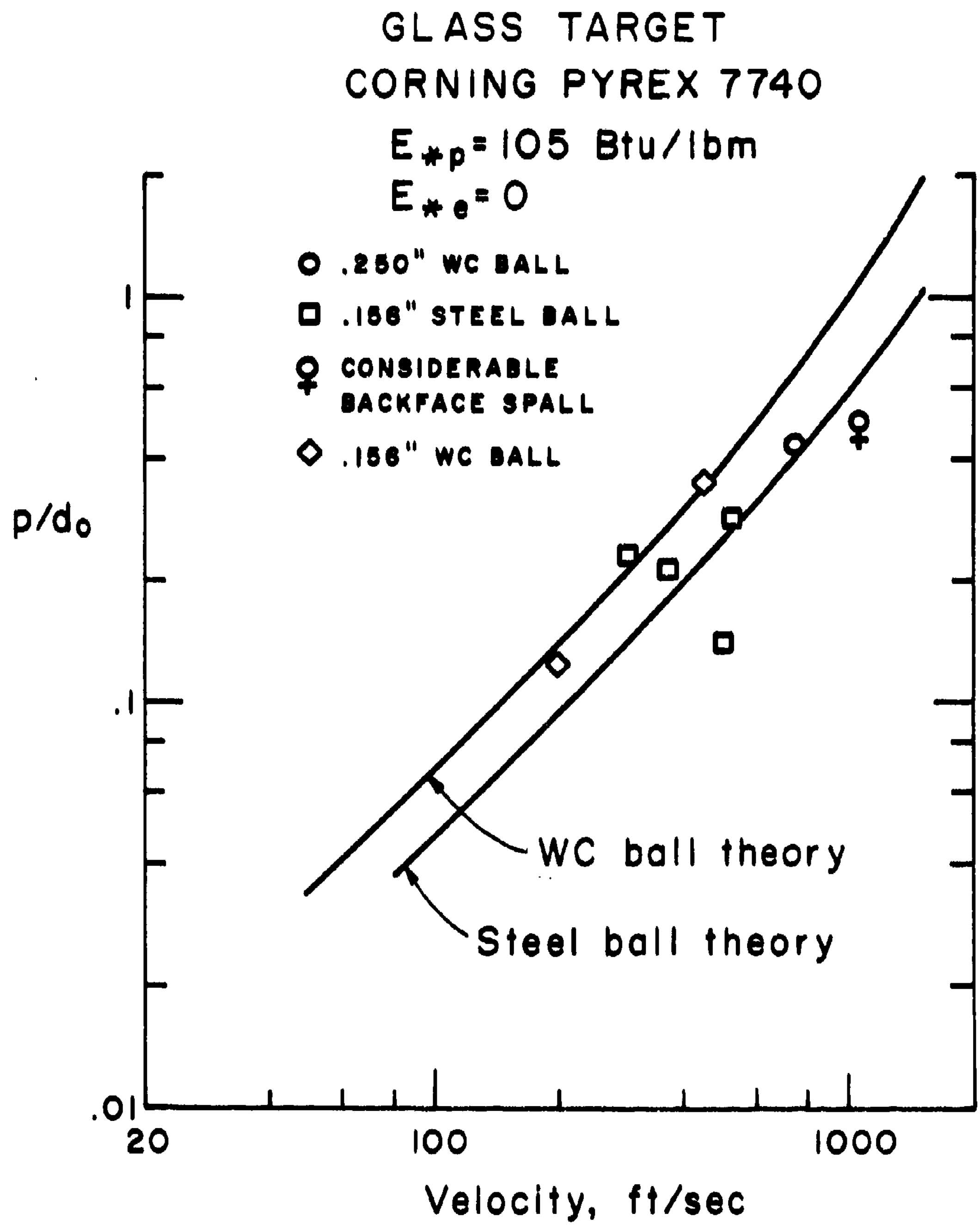
GLASS TARGET
CORNING PYREX 7740
E*p = 105 Btu/lbm
E*e = 0
.250" WC BALL
.156" STEEL BALL
CONSIDERABLE BACKFACE SPALL
.156" WC BALL
p/do
1
.1
.01
20
100
1000
Velocity, ft/sec
WC ball theory
Steel ball theory

Figure 16

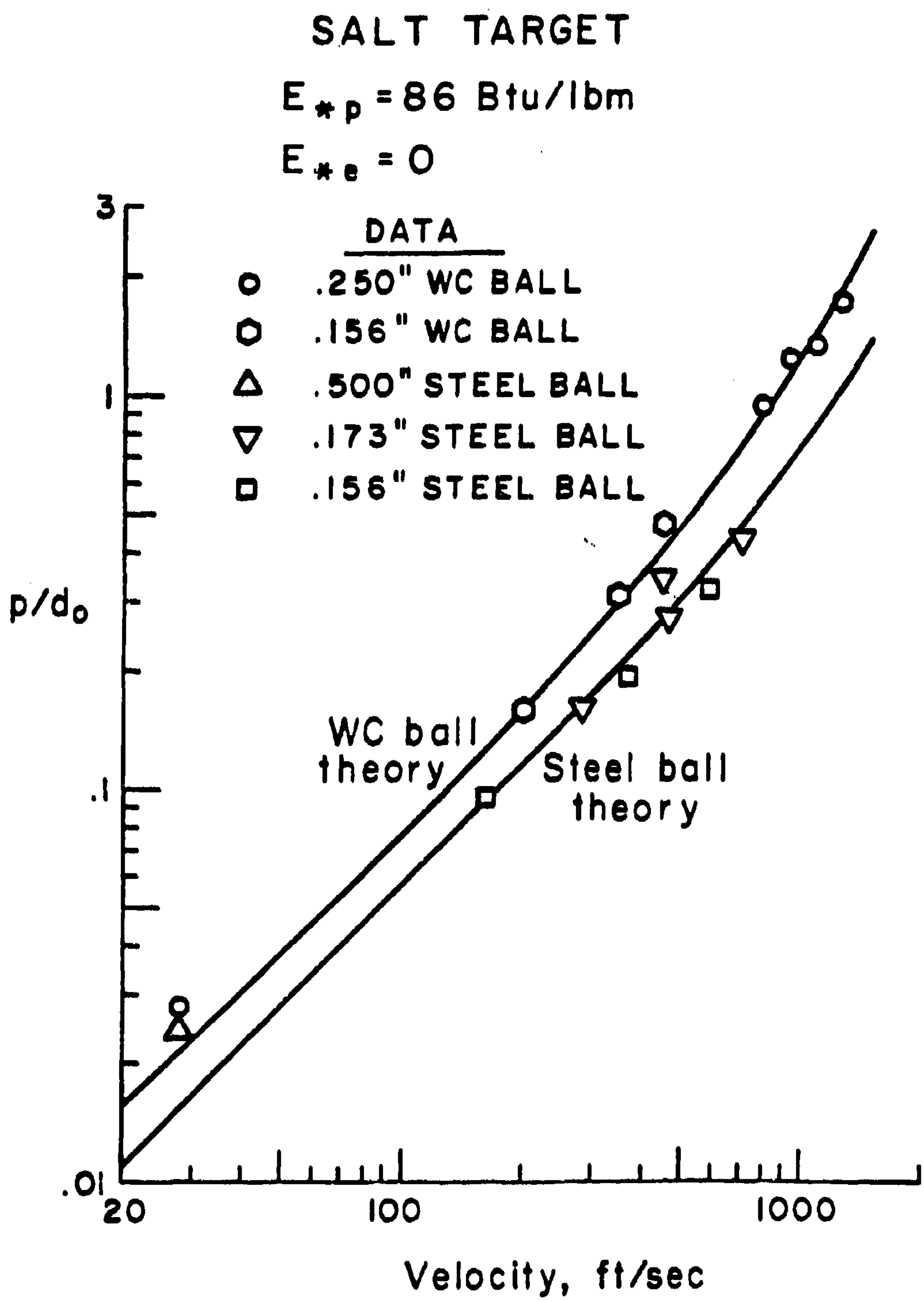

SALT TARGET
E*p = 86 Btu/lbm
E*e = 0
DATA
.250" WC BALL
.156" WC BALL
.500" STEEL BALL
.173" STEEL BALL
.156" STEEL BALL
p/do
3
1
.1
.01
20
100
1000
Velocity, ft/sec
WC ball theory
Steel ball theory

Figure 17

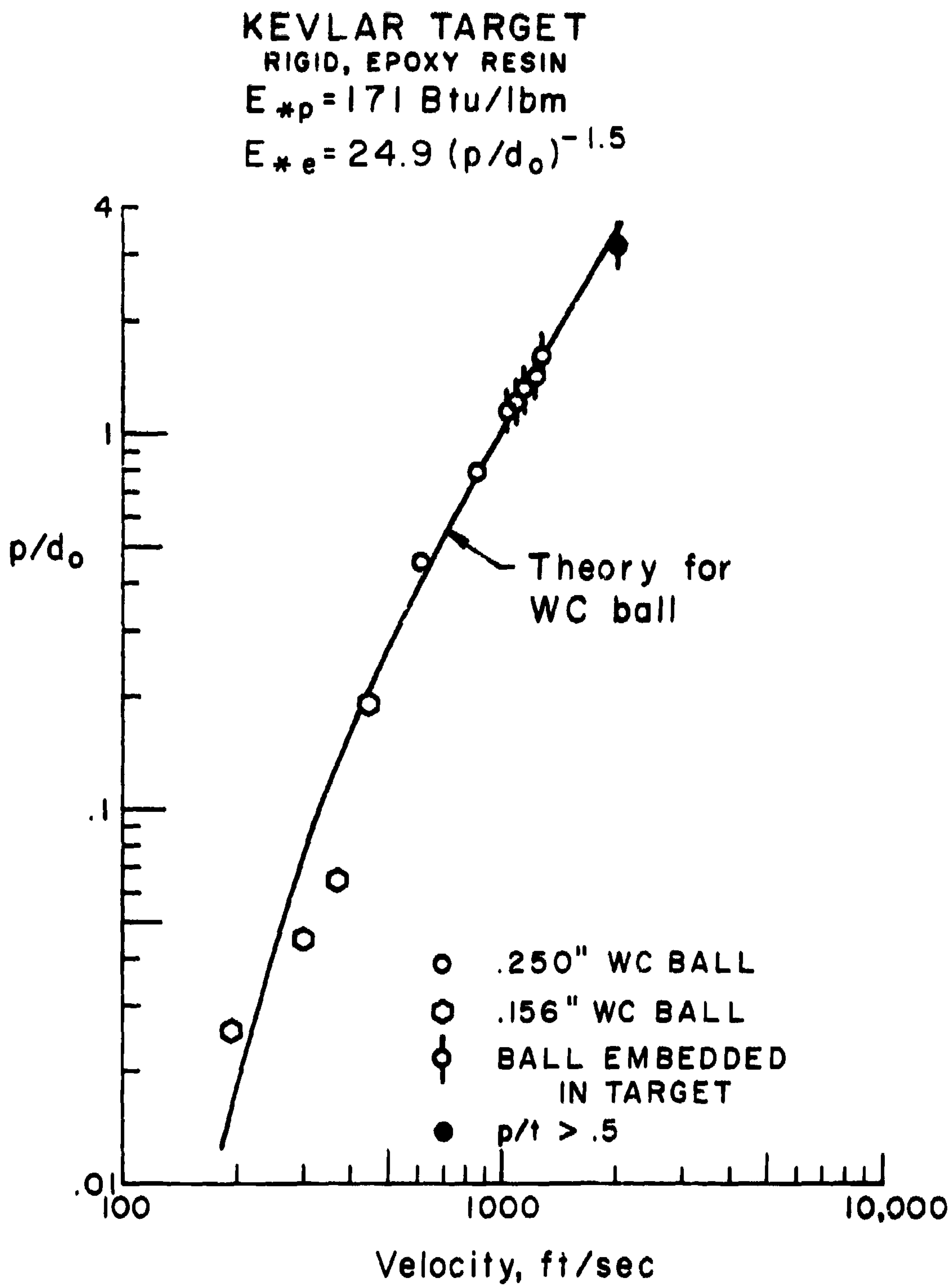

KEVLAR TARGET
RIGID, EPOXY RESIN
$E_{*p} = 171$ Btu/lbm
$E_{*e} = 24.9\,(p/d_o)^{-1.5}$
4
1
.1
.01
p/d_o
Theory for
WC ball
.250" WC BALL
.156" WC BALL
BALL EMBEDDED
IN TARGET
p/t > .5
100
1000
10,000
Velocity, ft/sec

Figure 18

which have just been discussed. The theory correctly predicts the dependence of penetration depth on velocity, projectile diameter, and density. Hence, the procedure described in this chapter can be used to obtain the impact properties of most target materials.

It appears, however, that the procedure does require some modification for characterizing extrememly hard, brittle materials. When the target is hard, the projectile breaks at relatively low velocity , and insufficient rigid ball data can be obtained to deduce E_* . If only broken ball data are available, then one must be careful to separate the target E_* from the ball deformation model. Even with nondeforming balls, brittle targets inherently have large scatter in crater depth measurements. A quantitative measure of this scatter or a procedure to reduce the scatter is necessary if much data for brittle materials are needed. Despite these limitations, the procedure described in this chapter does provide an adequate dynamic screening test for target materials in impact applications.

III. IMPACT PROPERTIES OF MATERIALS

This chapter contains a summary of the formulas which relate the characteristic properties E_{*p} and E_{*e} to more fundamental material properties such as Brinell hardness, melting temperature, heat capacity, and Young's modulus. The derivation of these formulas was presented in Ref. 1, and will not be repeated here. The values of the constants which appear in these formulas differ slightly from those which were contained in Ref. 1. The revisions are the result of a more detailed survey of materials data and a better fit to more impact test data. Also included in this chapter is a comprehensive table which summarizes the pertinent properties for many target materials.

A. Formulas for E_{*p} and E_{*e}

Before writing the equations, it is particularly important that the caveats be mentioned. When simple formulas are presented which purport to give solutions to complex problems the temptation is to accept the results without hesitation and to ignore the limitations of the model which produced the formulas. The formulas which are written below were derived to serve as a tool for the preliminary screening of target materials for particular impact applications, not as a final solution for E_{*p} and E_{*e} and not as a substitute for impact tests.

If one follows the derivations in Ref. 1. closely, it becomes clear that some gross assumptions have been made regarding material behavior and failure mechanisms, and that order-of-magnitude arguments have been used to justify the use of a single equation which is applicable to hard steel as well as soft zinc and to brittle ceramic as well as ductile plastic. The hope was that such a model would give a ball-park estimate for E_{*p} and E_{*e} . In this regard, the formulas succeed as a tool to distinguish good target materials from poor materials and to provide a rough ranking of materials. The fact that the equations predict the values of E_{*p} and E_{*e} within 15% for many materials is a dividend and a confirmation that the assumptions of the model are good for many materials. More importantly, however, the equations isolate those material properties which have the most influence on impact performance.

1. E_{*e} - The formula for E_{*e} is given by

$$E_{*e} = .69 \times 10^{-3} \frac{B^2\gamma}{\rho E} (p/d_o)^{-.75} , \qquad (27)$$

where B is Brinell hardness in N/m^2 , ρ is mass density in kg/m^3, E is Young's modulus in N/m^2, γ is a dimensionless strain rate parameter, and E_{*e} is given in Btu/lbm. The parameter γ accounts for the increase in Brinell hardness at high strain rates. It can be evaluated from hardness measurements taken at room temperature and at cryogenic temperatures using the strain rate - temperature relationships discussed in Ref. 1 and in Chapter 13 of Ref. 5. Typically, γ has a value of 1.5 for metals and 5.0 for plastics.

2. E_{*p} - The equation for E_{*p} is given by

$$E_{*p} = C_2 \, \beta \, \frac{C_p \, T_m}{2326.} \, \ell n \left[\frac{\sigma_f(T_i, \dot{\varepsilon})}{\beta\rho \, C_p \, T_m} + 1 \right], \qquad (28)$$

where C_p is the specific heat in joule/kgK, T_m is the melting temperature in K , σ_f is the flow stress corrected for strain rate effects in N/m^2 , E_{*p} is in Btu/lbm, and C_2 and β are constants which are obtained by correlating this equation with data from impact experiments. T_i is the initial temperature of the material, and $\dot{\varepsilon}$ is the strain rate. The present best estimate for the constants is

$$\beta = .072$$

$$C_2 = 5.76 \, . \qquad (29)$$

Note, the factor 2326 in the denominator of Eq. (28) is required to convert units from joule/kg to Btu/lbm - the typical units in which E_{*p} is expressed. The quasi-static flow stress can be obtained from Brinell hardness measurements using the Prandtl solution (Ref. 5) for the deformation flow field in a hardness test given by

---

5. McClintock, F. A. and Argon, A. S., *Mechanical Behavior of Materials*, Chapter 13, Addison-Wesley, Reading, Mass., 1966

$$\sigma_f = \frac{B}{3.2} . \tag{30}$$

This flow stress is corrected for strain rate effects using the "velocity-temperature" or "temperature-strain rate" interrelationship which was mentioned in Ref. 1 and is described in Ref. 5. In essence, this correction equates the hardness test performed at high strain rate to a hardness test performed at lower temperature. For many materials the increase in hardness for impact strain rates is equivalent to the increase in hardness for a 100 kelvin decrease in temperature. In general, Eq. (28) is within approximately 15% of the experimentally deduced values of E_{*p} for most metals.

For the brittle materials, the theory is generally within a factor of two of the experimental data. The discrepancy between theory and data is not unexpected. Recall that E_{*p} is the plastic energy dissipation which occurs in a thin, high shear region adjacent to the projectile. In impact tests of brittle targets, there is a large shard fracture mode which limits the extent of the shear region. In essence, the tensile release waves at the side of the projectile break off large pieces of target material before significant shearing can occur, thereby inhibiting the energy-dissipation potential of the material. Hence the performance of brittle materials in impact tests is considerably less than the theoretical prediction.

Equation (28) has one other interesting feature which should be noted. When the value of $\sigma_f/\beta\rho\, C_p\, T_m$ is very small compared to 1, Eq. (28) can be written

$$E_{*p} \simeq \frac{C_2}{\rho} \sigma_f . \tag{31}$$

For this case, there is a linear relationship between E_{*p} and the Brinell hardness of the material. However, when the value of $\sigma_f/\beta\rho\, C_p\, T_m$ is large, then the logarithm cannot be simplified and increasing the hardness of the material may result in but small improvements in E_{*p} because of the nature of the logarithm function. Hence, to a first approximation, Eq. (28) can be used to determine those materials whose impact performance can be improved by hardening techniques.

B. Table of Materials Properties

Table 2 presents a listing of the pertinent materials properties of many materials for which hardness, specific heat, and melting temperature data are available. These data were obtained from a variety of sources in the open literature. The properties were used in Eq. (28) to obtain the value of E_{*p} .

The final column in Table 2 lists the adiabatic hardness - the product ρE_{*p} - of each material. This quantity is particularly important for determining the penetration of a deforming projectile. Recall from Eq. (9) that the pressure on the front face of a projectile is primarily ρE_{*p} for low velocities. This pressure should be as high as possible if the objective is the deformation of the projectile.

Note that the properties in Table 2 contain both metric and English standard units. Both E_{*p} and the product ρE_{*p} have traditionally been tabulated in the units shown in Table 2. To convert these quantities to their metric equivalent the following conversion factors may be employed.

$$2326 \frac{\text{joule}}{\text{kg}} = 1 \frac{\text{Btu}}{\text{lbm}}$$

$$6895 \text{ Pascal} = 1 \text{ psi}$$

TABLE 2.

THEORETICAL E_{*p} FOR ASSORTED MATERIALS

	$C_p\left(\frac{J}{kgK}\right)$	T_m (K)	$B\left(\frac{kg}{mm^2}\right)$	$\rho\left(\frac{g}{cm^3}\right)$	$E_{*p}\left(\frac{Btu}{lbm}\right)$	ρE_{*p}(psi) x 10^{-5}	Material
1	936	933	26	2.7	64	.586	Aℓ, pure
2	936	933	95	2.7	164	1.50	Aℓ, (6061-T6)
3	936	933	125	2.7	193	1.76	Aℓ, armor
4	936	933	141	2.7	207	1.88	Aℓ, (7075)
5	130	1336	30	19.3	11	.706	Au
6	130	1336	60	19.3	19	1.23	Au
7	1046	2573	2800	2.34	1435	11.3	B
8	628	3800	8000	3.51	1586	18.8	C (diamond)
9	840	3952	19.5	2.25	62	.474	C (graphite)
10	547	593	17.8	8.64	24	.708	Cd
11	460	2148	1000	7.19	342	8.31	Cr (hard)
12	384	1356	51	8.9	37	1.12	Cu
13	459	1809	190	7.3	138	3.39	Fe (cast)
14	1610	850	50	1.41	200	.951	Kevlar-49
15	1170	523	20	1.2	127	.514	Lexan
16	1025	924	50	1.8	146	.886	Mg
17	1025	924	80	1.8	196	1.19	Mg
18	276	2883	160	10.22	104	3.60	Mo
19	877	1074	15	2.16	57	.415	NaCℓ

Table 2. Cont.

	C_p	T_m	B	ρ	E_{*p}	ρE_{*p} x 10^{-5}	Material
20	877	1074	30	2.16	85	.620	NaCℓ
21	129	2973	350	22.69	68	5.22	Os
22	125	600	4.5	11.34	3.6	.139	Pb
23	522	1683	163	2.33	232	1.82	Si (porous)
24	522	1683	820	2.33	453	3.56	Si (fused)
25	837	1990	1100	2.6	733	6.43	SiO_2 (quartz)
26	226	504	5	7.3	5.8	.144	Sn
27	226	504	15	7.3	14	.346	Sn
28	226	504	30	7.3	22	.549	Sn
29	459	1809	164	7.8	133	3.50	Steel (mild)
30	459	1809	250	7.8	173	4.55	Steel
31	459	1809	300	7.8	192	5.06	Steel (armor)
32	459	1809	400	7.8	224	5.90	Steel
33	459	1809	555	7.8	263	6.93	Steel
34	142	3269	73	16.6	34	1.89	Ta
35	266	3323	900	9.86	266	8.84	ThO
36	519	1941	374	4.5	271	4.11	Ti
37	142	3700	250	17.0	73	4.22	Mallory
38	138	3683	260	19.3	68	4.46	W
39	382	692	38	7.0	47	1.10	Zn

IV. LONG ROD PENETRATOR MODEL

This chapter summarizes the integral theory for long rod penetrators. Preliminary development of this model was described in Ref. 2, and listings of the computer codes ROD and PEN were provided. Unfortunately, these codes contained some theoretical and numerical errors which produced anomalous results at times. Improvements have been made to the ROD code which eliminate much of the anomalous behavior. However, it is important to note that there are still certain limitations in the use of this code. In its present form, the model is limited to: (1) high velocity impact, (2) homogeneous, isotropic rods, and (3) rod materials with some ductility. The reasons for these limitations are described below.

In the model, the head of the rod is assumed to flow hydrodynamically. There are no constitutive equations built into the deformation model, and there is no mechanism for energy dissipation due to internal shear stresses. As a result, the model is applicable for impact velocities which are high enough so that the pressures generated by the impact are much in excess of the material yield strength.

An additional assumption of the model is that the shape of the flowfield in the head does not change very much from material to material. Hence, each material undergoes the same amount of plastic deformation prior to failure. The model parameter, ε_o , which represents the plastic strain in the head, accounts for this deformation. A single value for ε_o appears to be adequate for most ductile rod materials. However, for brittle materials which have much lower values for strain to failure, a different model for ε_o may be needed.

A further assumption of the model is that the rod material is homogeneous and isotropic. Anisotropic material properties such as might exist for composite rods, for example, cannot be handled in the present model. In the future, as more impact data become available, the model will be extended to include constitutive equations and anisotropic material properties.

In what follows, the equations which govern the penetration of a long rod projectile will be presented. These equations form a coupled set of ordinary differential equations and are solved numerically using the ROD code. Appendix C contains the computer listings and a user's guide for this code. Typical results of numerical computations are presented at the end of this chapter.

A. Physics of the Model

It is known from x-ray photographs that the stages of long rod penetration may be roughly characterized as in Figure 19. As the rod impacts the target, the pressures generated at the interface begin to deform the front end of the rod, as in Figure 19(b). Simultaneously, the same pressure erodes the target and produces a crater as in Figure 19(c). As penetration continues, material at the leading face of the projectile is eroded by the target, forced out laterally from the contact region by the high pressure there and ejected back out of the crater. As material erodes from the rod face, new material is supplied to this region by the shaft of the rod which is traveling at a higher velocity than the rod-target interface. At some point, the shaft material is completely used, Figure 19(d), and the remaining head is then brought to a stop by the target.

1. Kinematics - The model for the rod flowfield consists of two regions; the head of the rod which corresponds to the region undergoing hydrodynamic strain and the shaft or rear portion of the rod which contains the undeformed material. During penetration the head which is in contact with the target decelerates and spreads laterally. It is assumed that the rod is cylindrical, that the shape of the head remains cylindrical during the penetration, and that the velocity flowfield in the head is linear. Figure 20 schematically illustrates the rod model and the pertinent nomenclature.

The motion of the material in the head is described by a center of mass velocity V_{cm} and by the velocity of its front face $V_{\perp}$ and side face V_{t}. At any instant, the thickness of the head is 2ℓ, and its radius is b. Since the velocity field is assumed to be linear, the following equations can be written for the particle velocity at the shaft-head interface,* V_b,

$$V_b = V_{\perp} + 2(V_{cm} - V_{\perp}) , \tag{32}$$

and for the rate of change of head dimensions

*In this analysis, no distinction is made between particle velocity and surface velocity at the shaft-head interface.

FLOW FIELD OF ROD AT VARIOUS STAGES OF PENETRATION

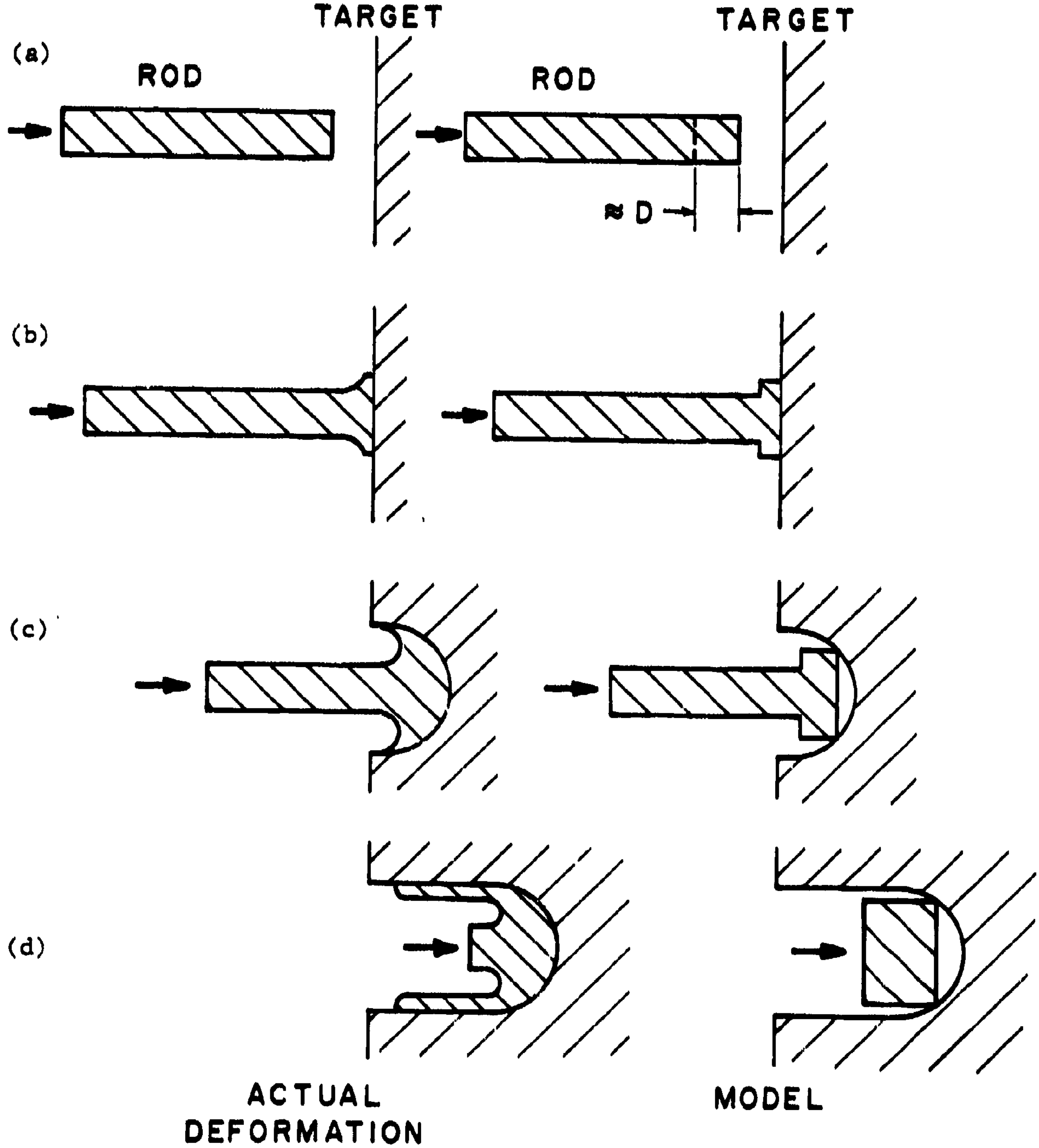

Figure 19

LONG ROD MODEL

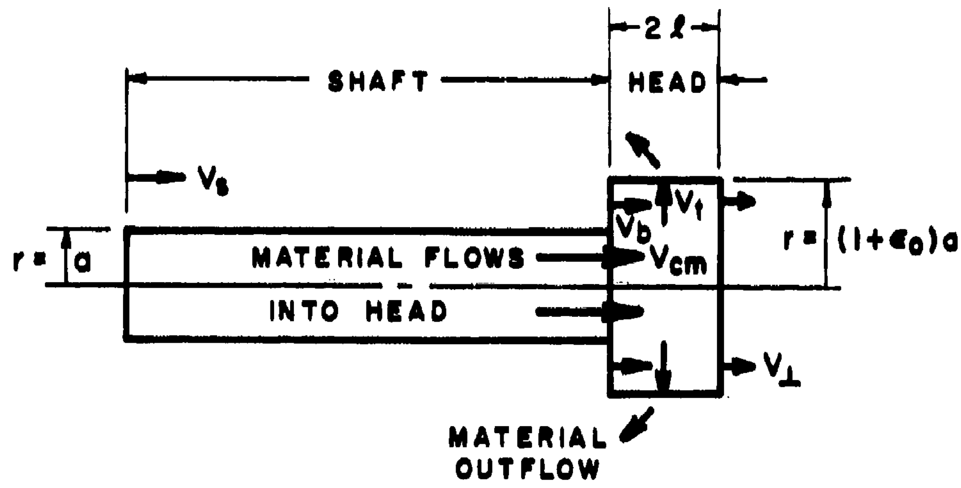

ASSUMPTIONS:

1. Conservation of energy
2. Conservation of momentum
3. Linear flow field in head
4. Continuity of mass flow across interface
5. Constant yield stress at interface
6. Mass of penetrator erodes from head when radius exceeds $(1+\epsilon_0)a$
7. The model depends upon two parameters:

   The yield stress $\sigma \cong \rho E_{*d} = \chi \rho E_*$

   and

   The shearing radius given by $(1+\epsilon_0)a$

Figure 20

$$\dot{\ell} = V_i - V_{cm} , \tag{33}$$

$$\dot{b} = V_t \quad \text{for} \quad b < (1 + \varepsilon_o)a , \tag{34a}$$

$$\dot{b} = 0 \quad \text{for} \quad b \geq (1 + \varepsilon_o)a , \tag{34b}$$

where a is the initial radius of the head, and the dot above a symbol denotes the time derivative. The quantity ε_o represents the allowable plastic strain in the head.

As penetration proceeds, the head widens as rod material is forced to flow in the lateral direction. At some distance from the axis of the rod, say $(1 + \varepsilon_o)a$ laterally, material is detached from the head. The dynamics of this material as it further interacts with the target has no subsequent effect on the head or shaft. This assumption is justified because the rod material at this point in the flow has been adiabatically heated by plastic work to such an extent that its shear strength is very low. Hence, it is able to influence the rod only through compressive or hydrodynamic forces. However, the axial component of the compressive hydrodynamic force will only be significant within one or two rod radii from the central axis. Thus, $(1 + \varepsilon_o)a \leq 2a$ and really characterizes the turning radius of the rod material in the target or the shape of the flowfield in the head. For simplicity, it is assumed that the shape of the flowfield does not change too much with different materials. Hence, ε_o is the same for all rod penetrators, independent of material. Its value can be deduced from impact data. More on this point later.

2. <u>Mass Conservation</u> - Conservation of mass across the shaft-head interface imposes the following condition for the rate at which material flows from the shaft to the head,

$$\dot{m}_a = \rho_p \pi a^2 \; (V_s - V_b) , \tag{35}$$

where ρ_p is the penetrator density, and V_s is the shaft velocity.

When the radius of the head reaches the value $(1 + \varepsilon_o)a$, it is assumed that any further increase in the radius simply

results in loss of rod material across the boundary. The rate of mass loss from the head is given by

$$\dot{m}_b = 4\pi\rho_p b\ell(V_t - \dot{b}) \ . \tag{36}$$

Before the head reaches the cutoff radius, $V_t = \dot{b}$ and $\dot{m}_b = 0$. After the cutoff radius is reached, $\dot{b} = 0$.

The rate of change of mass in the head can be obtained from Eqs. (35) and (36)

$$\dot{m}_h = \dot{m}_a - \dot{m}_b = \pi\rho_p \left[a^2(V_s - V_b) - 4b\ell(V_t - \dot{b})\right] \ , \tag{37}$$

and the rate of change of mass in the shaft is simply

$$\dot{m}_s = - \dot{m}_a = - \rho_p \pi a^2(V_s - V_b) \ . \tag{38}$$

3. Momentum conservation - The pressure* applied to the front face of the rod by the target is given by

$$P = \rho_t\left(E_* + C_D \frac{V_\perp^2}{2}\right) . \tag{39}$$

This pressure acts across the entire front face of the rod which is in contact with the target. The contact area is πb^2 . Hence, the drag force becomes

$$F = \pi b^2\rho_t\left(E_* + C_D \frac{V_\perp^2}{2}\right) . \tag{40}$$

The equation for conservation of axial momentum can be written

*Equation (39) is written for a total $E_* = E_{*p} + E_{*e}$. However, only E_{*p} is used at the present time.

$$\frac{d}{dt}(m_h V_{cm} + m_s V_s) = -F - \dot{m}_b V_{cm}$$

$$= -\pi b^2 \rho_t \left(E_* + C_D \frac{V_\perp^2}{2}\right) - \dot{m}_b V_{cm} , \quad (41)$$

where the second term on the right side accounts for the flux of axial momentum out the side of the head. This equation may be separated into two equations for the head and the shaft. The shaft will only experience deceleration forces if it has a nonzero yield strength σ . In general, the force on the shaft, F_s , is given by

$$F_s = -\pi a^2 \sigma = m_s \dot{V}_s . \quad (42)$$

When $\sigma = 0$, as is the case for a shaped-charge jet which is liquid, the shaft velocity remains constant during the entire penetration.

An illustrative equation is obtained by combining Eqs. (37), (38), (41), and (42) to obtain an equation for the deceleration of the head

$$m_h \dot{V}_{cm} = -\pi b^2 \rho_t \left(E_* + C_D \frac{V_\perp^2}{2}\right) + \pi a^2 \sigma + \dot{m}_a \left(V_s - V_{cm}\right) . \quad (43)$$

The first term on the right is the deceleration of the head due to the target pressure. The second term is the acceleration of the head due to the push from behind by the yield strength of the shaft. The third term is the net momentum flux to the head due to mass flux across material surfaces.

4. Energy conservation - The total kinetic energy in the rod is given by

$$K = K_s + K_{cm} + K_r , \quad (44)$$

where

$$K_s = \frac{1}{2} m_s V_s^2 , \quad (45)$$

is the kinetic energy in the shaft and

$$K_{cm} = \frac{1}{2} m_h V_{cm}^2 , \tag{46}$$

is the kinetic energy associated with the mass center motion of the head and

$$K_r = \frac{1}{6} m_h \left[\frac{3}{2} V_t^2 + (V_\perp - V_{cm})^2 \right] , \tag{47}$$

is the kinetic energy in the head relative to the mass center motion, i.e., the energy associated with the deformation of the head. Equation (47) can be obtained by integrating the linear velocity distribution over the entire volume of the head, i.e.

$$K_h = K_{cm} + K_r = \frac{1}{2} \rho_p \int_{vol} \left(V_r^2 + V_\theta^2 + V_z^2 \right) RdRd\theta dz , \tag{48}$$

where

$$V_r = \frac{R}{b} V_t$$

$$V_\theta = 0$$

$$V_z = V_{cm} + \frac{z}{\ell} (V_\perp - V_{cm}) .$$

Equations (44-47) can be differentiated to yield the following kinematic expressions

$$\dot{K} = \dot{K}_{cm} + \dot{K}_s + \dot{K}_r , \tag{49}$$

$$\dot{K}_{cm} = \frac{1}{2} \dot{m}_h V_{cm}^2 + m_h V_{cm} \dot{V}_{cm} , \tag{50}$$

$$\dot{K}_s = \frac{1}{2} \dot{m}_s V_s^2 + m_s V_s \dot{V}_s , \tag{51}$$

$$\dot{K}_r = \frac{\dot{m}_h}{6} \left[\frac{3}{2} V_t^2 + (V_\perp - V_{cm})^2 \right] + \frac{m_h}{6} \left[3 V_t \dot{V}_t + 2 (V_\perp - V_{cm}) (\dot{V}_\perp - \dot{V}_{cm}) \right] . \tag{52}$$

The rate at which work is done on the rod by the target is given by

$$\dot{U} = \pi b^2 \rho_t V_\perp \left(E_* + \frac{C_D}{2} V_\perp^2 \right) . \tag{53}$$

The heating rate, denoted by $\dot{W}$, or the rate at which rod material is converted into the hydrodynamic state is given by

$$\dot{W} = \dot{m}_a E_{*d} . \tag{54}$$

$\dot{W}$ represents the rate at which energy is dissipated as material crosses the interface between shaft and head and is transformed from the solid to the hydrodynamic state. The quantity E_{*d} is the "adiabatic yield strength" of the rod material. More about this quantity later.

The flux of kinetic energy which crosses the lateral boundaries of the head is given by

$$\dot{K}_b = \frac{1}{2} \dot{m}_b \left[V_t^2 + V_{cm}^2 + \frac{1}{3} (V_\perp - V_{cm})^2 \right] . \tag{55}$$

Conservation of energy requires that $\dot{K} + \dot{U} + \dot{W} + \dot{K}_b = 0$ or

$$\dot{K} = - \pi b^2 \rho_t V_\perp \left(E_* + \frac{C_D}{2} V_\perp^2 \right) - \dot{m}_a E_{*d}$$
$$- \frac{1}{2} \dot{m}_b \left[V_t^2 + V_{cm}^2 + \frac{1}{3} (V_\perp - V_{cm})^2 \right] . \tag{56}$$

5. Incompressibility - The final equation which is needed to specify the problem is the statement of incompressibility. At any instant, the mass in the head is given by

$$m_h = 2\pi b^2 \ell \rho_p . \tag{57}$$

If the rod material is incompressible, then ρ_p is constant and Eq. (57) can be differentiated to yield

$$\dot{m}_h = m_h \left[\frac{2\dot{b}}{b} + \frac{\dot{\ell}}{\ell} \right] . \tag{58}$$

6. System of equations - The preceding equations form a system of first-order ordinary differential equations which can be solved simultaneously to yield solutions, as a function of time, for the velocity field, dimensions of the head and shaft, and energy partitioning. One additional equation is needed to obtain solutions as a function of depth of penetration, i.e.,

$$\dot{y} = V_1 . \tag{59}$$

The complete system of equations is summarized in Table 3. The numerical procedure employed to integrate this system is discussed in Appendix C. The input parameters required for running the code are the length and diameter of the rod, the density, adiabatic yield strength and adiabatic hardness of the rod material, the density and hydrodynamic mode energy of the target, and the plastic strain in the head ε_o .

7. Model parameters - It is assumed that the energy dissipation parameter of the rod material, E_{*d} , is directly proportional to the hydrodynamic mode energy, E_* , i.e.

$$E_{*d} = \chi E_* . \tag{60}$$

The value of E_* , of course, is deduced from impact tests using the procedure described in Chapter II or, in the absence of impact data, estimated from Eq. (28). The value of E_{*d} is different from E_* because the flowfield in the rod is somewhat different than in a semi-infinite target of the same material. The value of χ can be obtained by correlating impact data and numerical computations. As a result of such correlations, $\chi = 0.42$ has been obtained. An experimental program was designed and conducted at A.R.A.P. to measure E_{*d} at laboratory strain rates. This program is described in Chapter V.

TABLE 3.

ROD MODEL EQUATIONS

Mass

$$\dot{m}_h = \pi a^2 \rho_p \left(V_s - V_b\right) - \dot{m}_b \quad (37)$$

$$\dot{m}_b = 4\pi b \ell \rho_p \left(V_t - \dot{b}\right) \quad (36)$$

$$\dot{m}_s = - \rho_p \pi a^2 \left(V_s - V_b\right) \quad (38)$$

Momentum

$$\frac{d}{dt}\left(m_h V_{cm} + m_s V_s\right) = - \pi b^2 \rho_t \left(E_* + \frac{C_D V_\perp^2}{2}\right) - \dot{m}_b V_{cm} \quad (41)$$

$$m_s \dot{V}_s = - \pi a^2 \sigma \quad (42)$$

Energy

$$\dot{K} = \dot{K}_{cm} + \dot{K}_r + \dot{K}_s \quad (49)$$

$$\dot{K}_{cm} = \frac{1}{2} \dot{m}_h V_{cm}^2 + m_h V_{cm} \dot{V}_{cm} \quad (50)$$

$$\dot{K}_s = \frac{1}{2} \dot{m}_s V_s^2 + m_s V_s \dot{V}_s \quad (51)$$

$$\dot{K}_r = \frac{\dot{m}_h}{6}\left[\frac{3}{2} V_t^2 + (V_\perp - V_{cm})^2\right] + \frac{m_h}{6}\left[3V_t \dot{V}_t + 2(V_\perp - V_{cm})(\dot{V}_\perp - \dot{V}_{cm})\right], \quad (52)$$

$$\dot{K} = -\pi b^2 \rho_t V_\perp \left(E_* + \frac{C_D}{2} V_\perp^2\right) - \rho_p \pi a^2 \left(V_s - V_b\right) E_{*d}$$
$$- \frac{1}{2}\dot{m}_b \left[V_t^2 + V_{cm}^2 + \frac{1}{3}\left(V_\perp - V_{cm}\right)^2\right] \quad (56)$$

Kinematics

$$\dot{b} = V_t \qquad b < (1+\varepsilon_o)a$$
$$\dot{b} = 0 \qquad b \geq (1+\varepsilon_o)a \quad (34)$$

$$\dot{\ell} = V_\perp - V_{cm} \quad (33)$$

$$V_b = V_\perp + 2(V_{cm} - V_\perp) \quad (32)$$

$$\dot{y} = V_\perp \quad (59)$$

Incompressibility

$$\dot{m}_h = m_h \left[\frac{2\dot{b}}{b} + \frac{\dot{\ell}}{\ell}\right] \quad (58)$$

The adiabatic yield stress, σ , is related to the adiabatic hardness, $\rho_p E_*$, of the material by

$$\sigma = \rho_p E_{*d} = \chi \rho_p E_* . \tag{61}$$

This equation, which is similar to Eq. (30), is analogous to the relationship between the Brinell hardness, B , and the uniaxial tensile strength of a material in static tests.

The last parameter, ε_o , is assumed to be constant for all rod materials. The limitations of this assumption for brittle materials and composite rods have already been noted. The value of ε_o can only be deduced by correlating data and computations. As a result of such correlations, the value $\varepsilon_o = 0.36$ has been obtained.

8. Backface Effects - The resistance of the target to penetration by the projectile is given by Eq. (40). When the target is thick, the value of E_* obtained by the procedures described in Chapters II and III should be used. However, to apply the integral theory to targets of finite thickness, it is necessary to adjust E_* for backface effects.

Recall that the E_* concept was originally developed for the flow of target material around a penetrator in a semi-infinite target. The shear work done on the target material in the flow volume defines E_* . When the projectile has penetrated almost all the way through the target, to within one or two rod diameters of the backface, the target material can spall or simply bulge on the backside, rather than flow around the penetrator hydrodynamically. Thus, each small volume of target material absorbs less energy than it would in the semi-infinite case. Thus, the effective E_* for the target decreases near the backface. In Chapter IV of Ref. 2, a simple model for the decrease in E_* near the backface was proposed. The reader is referred to that development for the details. Briefly, for those materials which exhibit backface effects, the value of E_* is held constant until the head of the rod reaches a point which is two rod diameters from the backface. From this point, the E_* of the target is decreased linearly with distance such that E_* is zero when the front of the head reaches the backface.

9. Oblique impact - The rod model described above can also be used for the case of oblique impact. In this case, the target thickness is equivalent to the slant length of the target. For oblique impact of finite-thickness targets, the backface effect occurs when the perpendicular distance from the front of the head to the backface of the target is less than two rod diameters. This treatment of oblique impact does not attempt to handle fracture of the rod shaft or jetting of the rod front end during impact.

10. Multi-layer targets - The rod model has been used with some success for multi-layered targets. For such targets, the equations are solved for each layer. The conditions which exist at the rear of one layer simply become the initial conditions for the next layer. This procedure continues until the penetrator is stopped or perforates the last layer.

B. Correlations of Theory and Data

The parameters ε_o and χ can be deduced from correlations with data. Experiments were conducted for A.R.A.P. at the Ballistics Research Lab (BRL), Aberdeen Proving Grounds. Several long rods with a length-to-diameter ratio, L/D, of 10 were fired into targets of Rolled Homogeneous Steel Armor. In order to avoid backface effects, very thick targets - target thickness greater than twice the total rod penetration - were used. The rods were chosen to provide a variety of materials and strengths. The materials included mild (1018) steel, tantalum, lead, and Mallory 3000, a tungsten alloy.

The data were compared to calculations using the ROD code to select a best fit for ε_o, which characterizes the maximum strain in the head, and χ which relates the adiabatic hardness to the adiabatic yield strength of the rod. The value of E_* for the armor steel target is 200 Btu/lbm. For the rod materials, the values of E_* are: Mallory 3000 - 50 Btu/lbm; tantalum - 80 Btu/lbm; 1018 steel - 140 Btu/lbm; lead - 3.5 Btu/lbm. Based on these comparisons, it was deduced that $\varepsilon_o = .36$ and $\chi = .42$. A comparison of the correlations between theory and data is shown in Figures 21 - 24. Note that the high velocity lead rod deformed upon exit from the barrel and had an irregular shape upon impact. The L/D for this rod was somewhere between 5 and 10.

The ROD code can be used for finite thickness targets. The values of the parameters ε_o and χ remain 0.36 and 0.42 respectively. However, the decrease in the E_* of the target

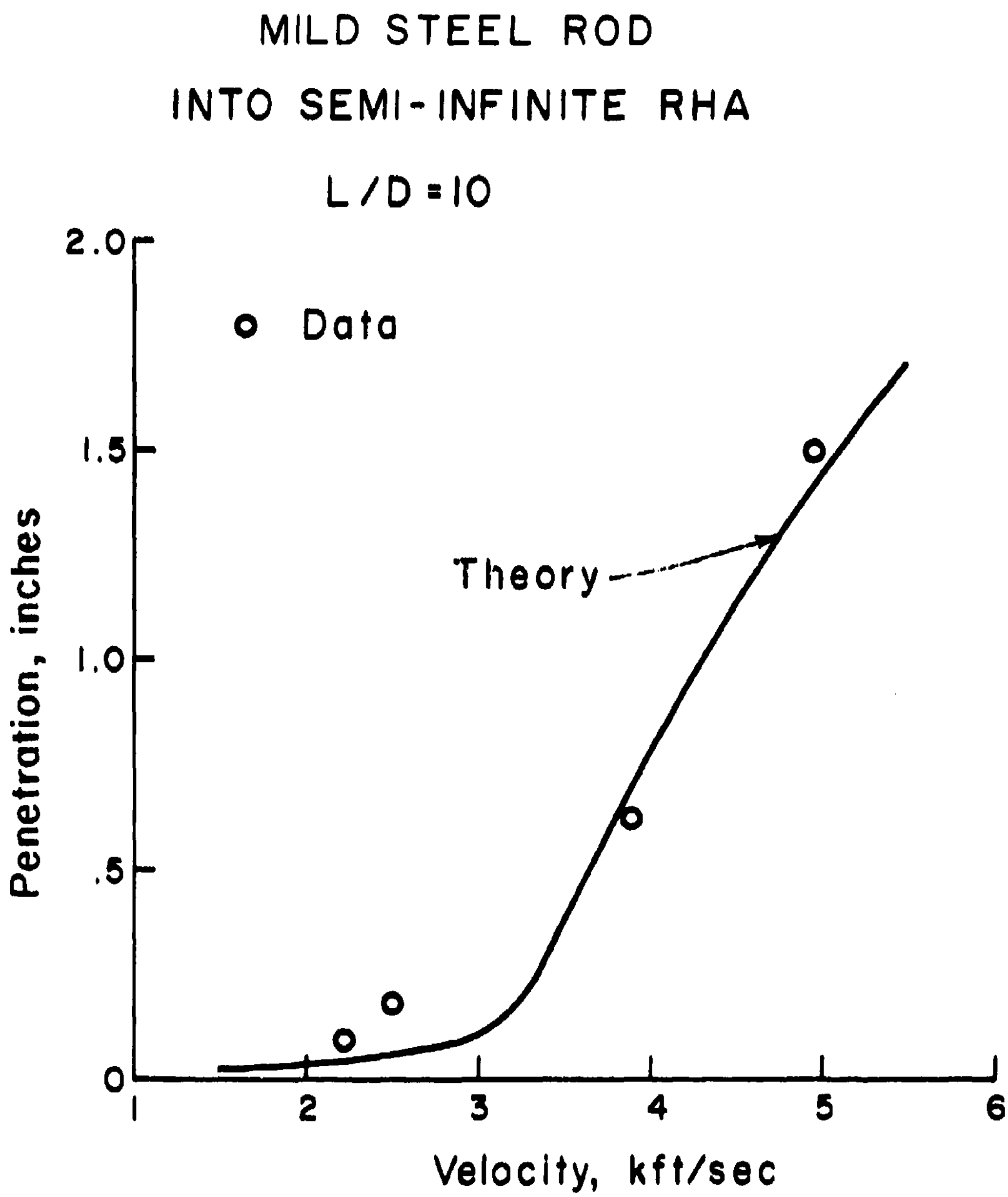
MILD STEEL ROD
INTO SEMI-INFINITE RHA
L/D = 10
Data
Theory
Penetration, inches
2.0
1.5
1.0
.5
0
1
2
3
4
5
6
Velocity, kft/sec

Figure 21

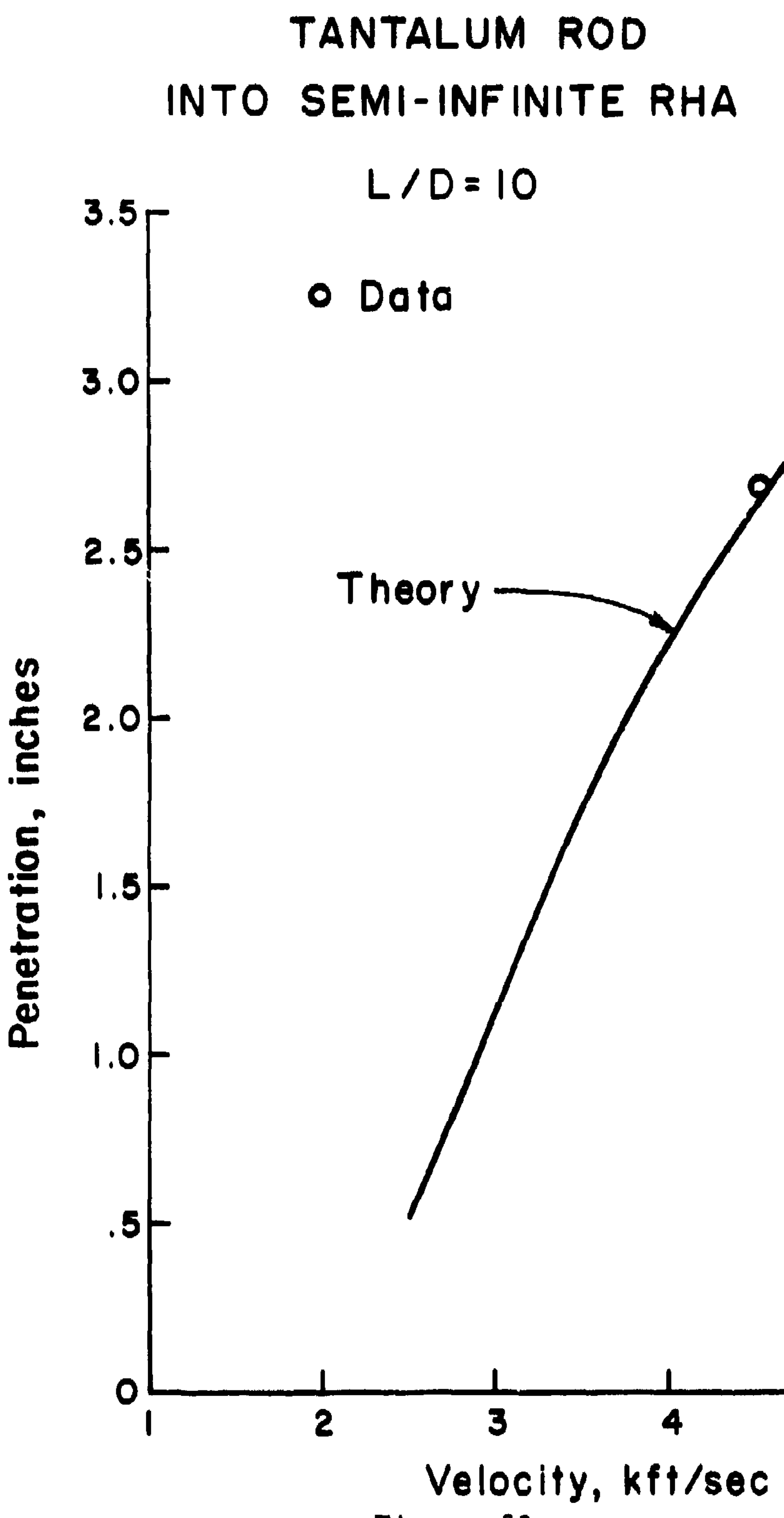
TANTALUM ROD
INTO SEMI-INFINITE RHA
L/D=10
o Data
Theory
Penetration, inches
3.5
3.0
2.5
2.0
1.5
1.0
.5
0
1
2
3
4
5
6
Velocity, kft/sec
Figure 22

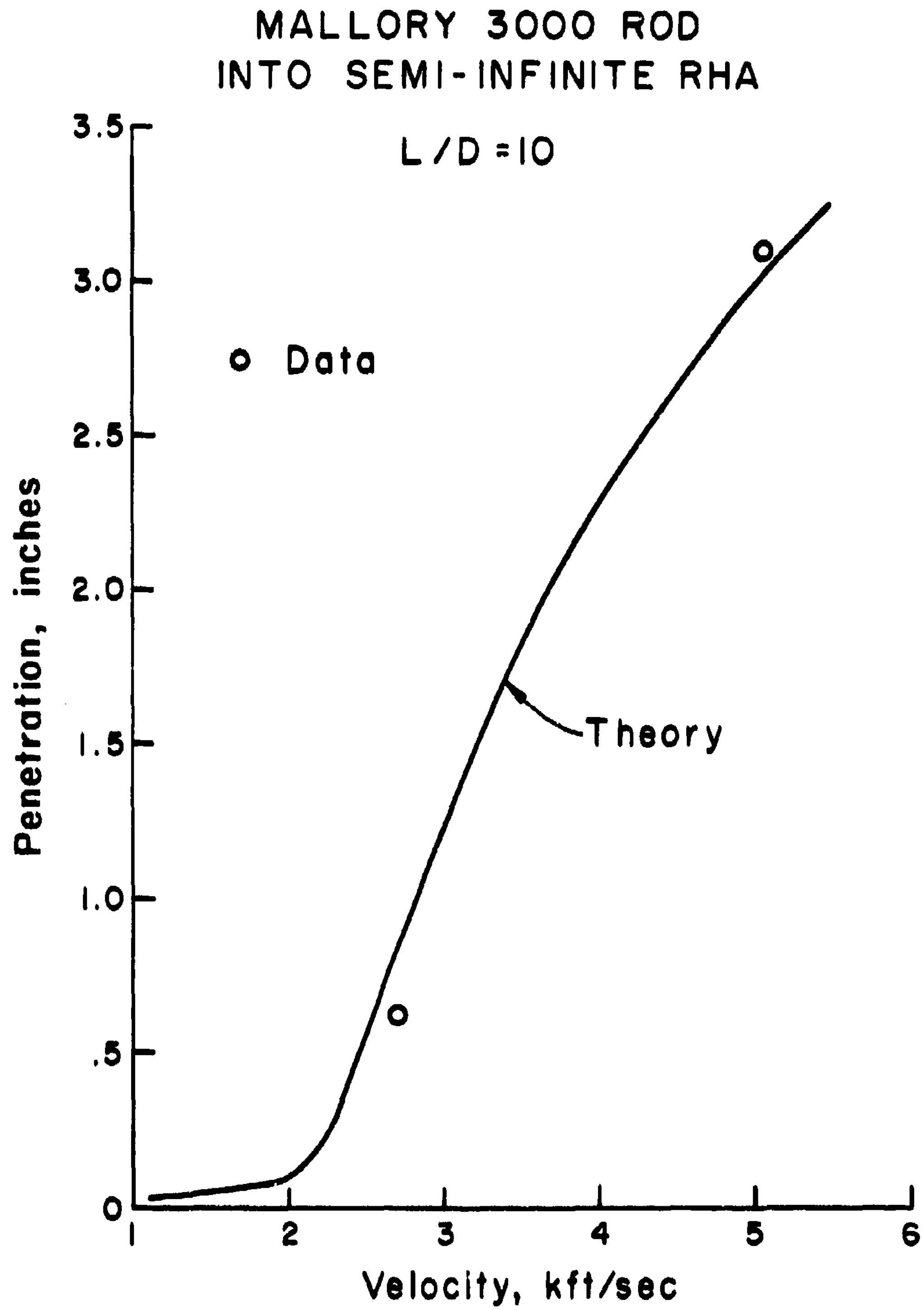
MALLORY 3000 ROD
INTO SEMI-INFINITE RHA
L/D = 10
Data
Theory
Penetration, inches
Velocity, kft/sec
3.5
3.0
2.5
2.0
1.5
1.0
.5
0
1
2
3
4
5
6

Figure 23

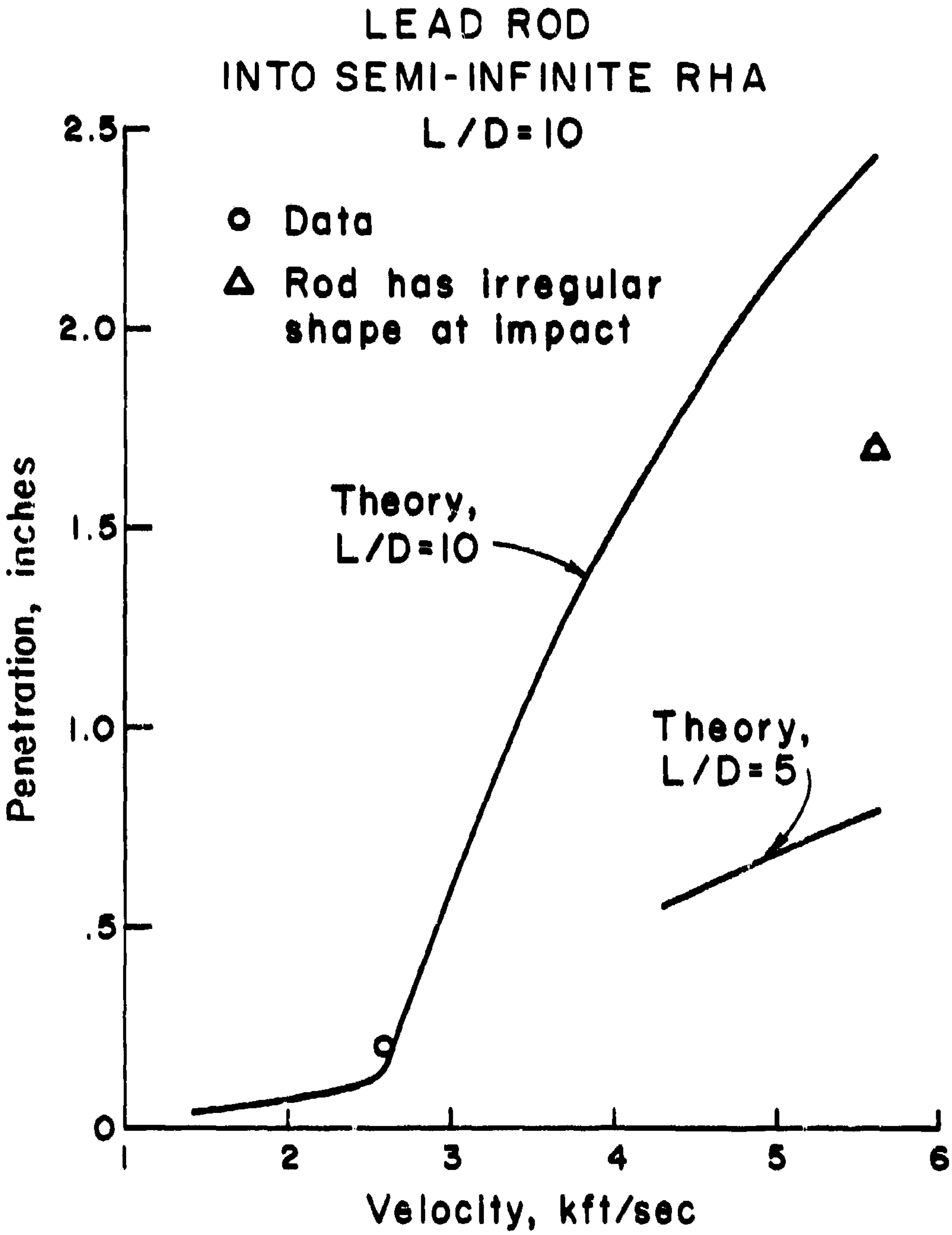
LEAD ROD
INTO SEMI-INFINITE RHA
L/D=10
o Data
Δ Rod has irregular shape at impact
Theory, L/D=10
Theory, L/D=5
Penetration, inches
2.5
2.0
1.5
1.0
.5
0
1
2
3
4
5
6
Velocity, kft/sec

Figure 24

in the vicinity of the backface must be taken into account, as was noted above. Figures 25-28 show some comparisons of theory and data for residual velocity and residual mass. The theoretical prediction for residual velocity is the shaft velocity at the instant the head of the rod reaches the backface. The residual mass is the sum of the mass in the shaft and in the head at this instant. The data are taken from a recent BRL report by Lambert (Ref. 6). Residual mass data are of two kinds: (1) reduced from radiographs; (2) measured from recovered fragments. The residual velocity data were reduced from radiographs. The projectiles were 65 gram Bearcat steel rods (hardness Rockwell C-55) with various L/D ratios. These rods were fired into various thickness targets of Rolled Homogeneous Steel Armor.

Figures 25 and 26 show the results for L/D = 5 rods fired into two different finite thickness targets. Figure 27 shows the residual velocity for an L/D = 10 rod. No residual mass data are available for these tests. Figure 28 is for an L/D = 20 rod. In general, the agreement with data is good, and the model correctly predicts the trends with velocity. For these cases, the model underpredicts the ballistic limit velocity by approximately 10 to 15%.

---

6. Lambert, John P.: The Terminal Ballistics of Certain 65 Gram Long Rod Penetrators Impacting Steel Armor Plate. Rept. No. ARBRL-TR02072, May 1978.

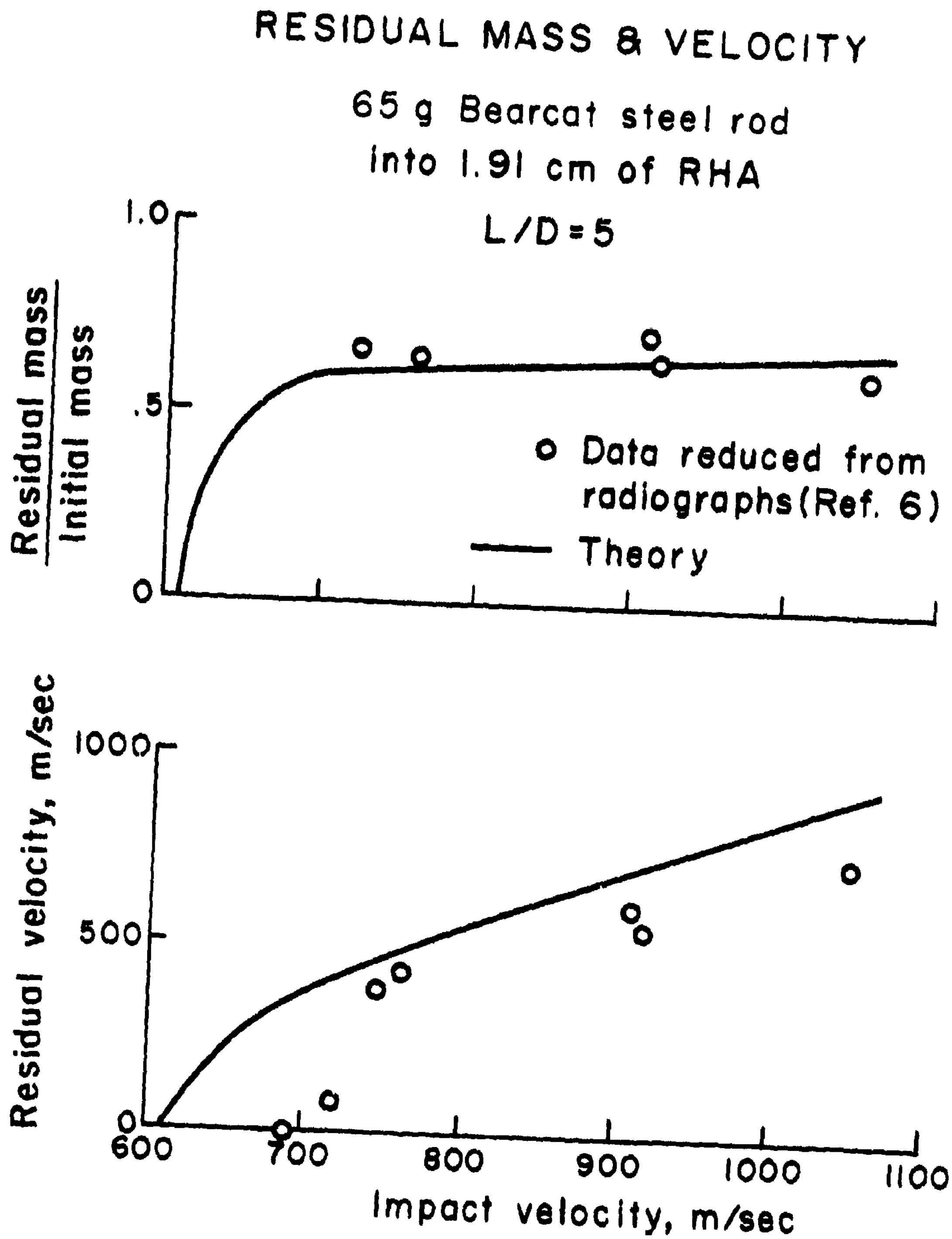
RESIDUAL MASS & VELOCITY
65 g Bearcat steel rod
into 1.91 cm of RHA
L/D=5
Residual mass / Initial mass
1.0
.5
0
Data reduced from radiographs(Ref. 6)
Theory
Residual velocity, m/sec
1000
500
0
600
700
800
900
1000
1100
Impact velocity, m/sec

Figure 25

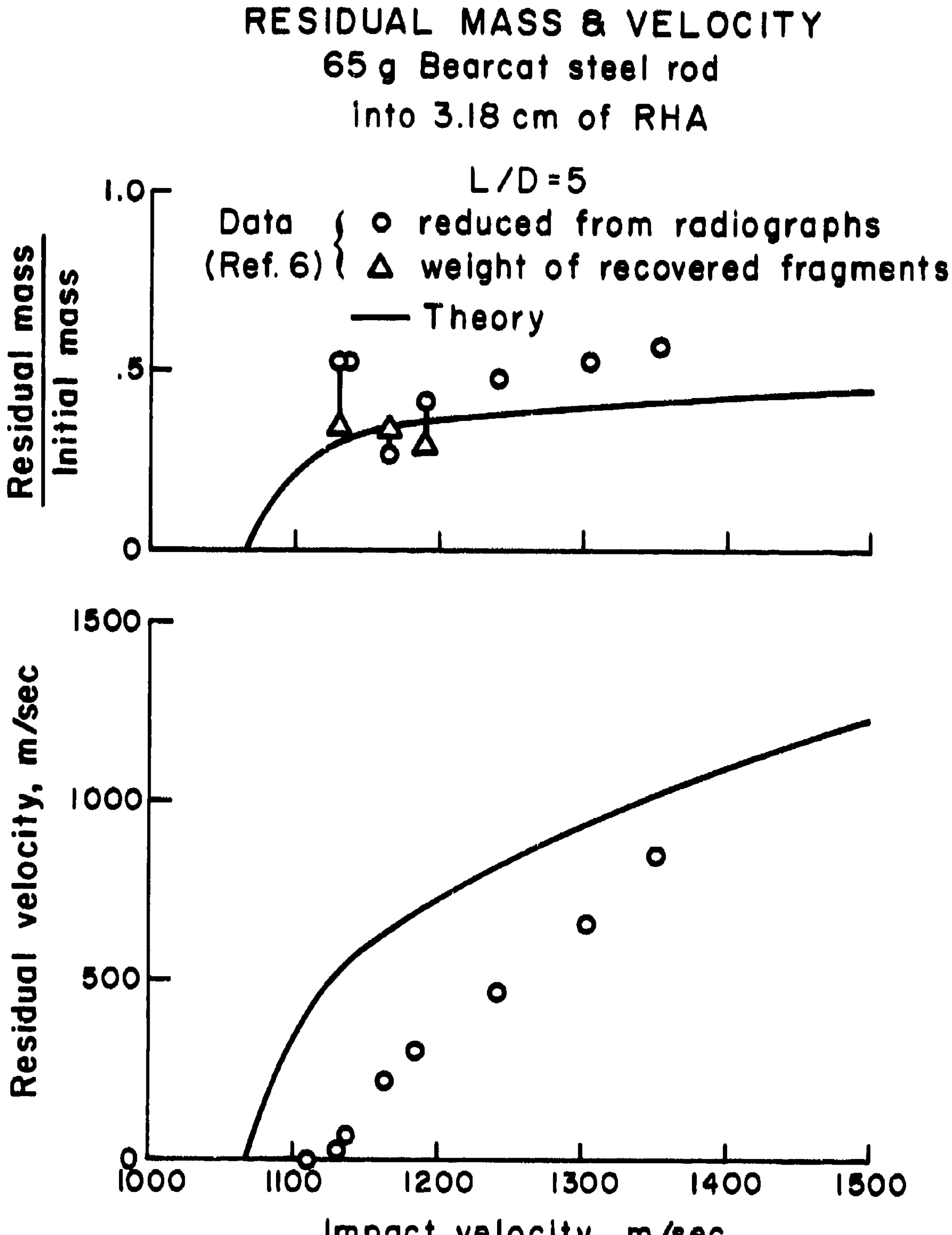
RESIDUAL MASS & VELOCITY
65 g Bearcat steel rod
into 3.18 cm of RHA
L/D = 5
Data (Ref. 6)
o reduced from radiographs
Δ weight of recovered fragments
— Theory
Residual mass / Initial mass
1.0
.5
0
Residual velocity, m/sec
1500
1000
500
0
1000
1100
1200
1300
1400
1500
Impact velocity, m/sec

Figure 26

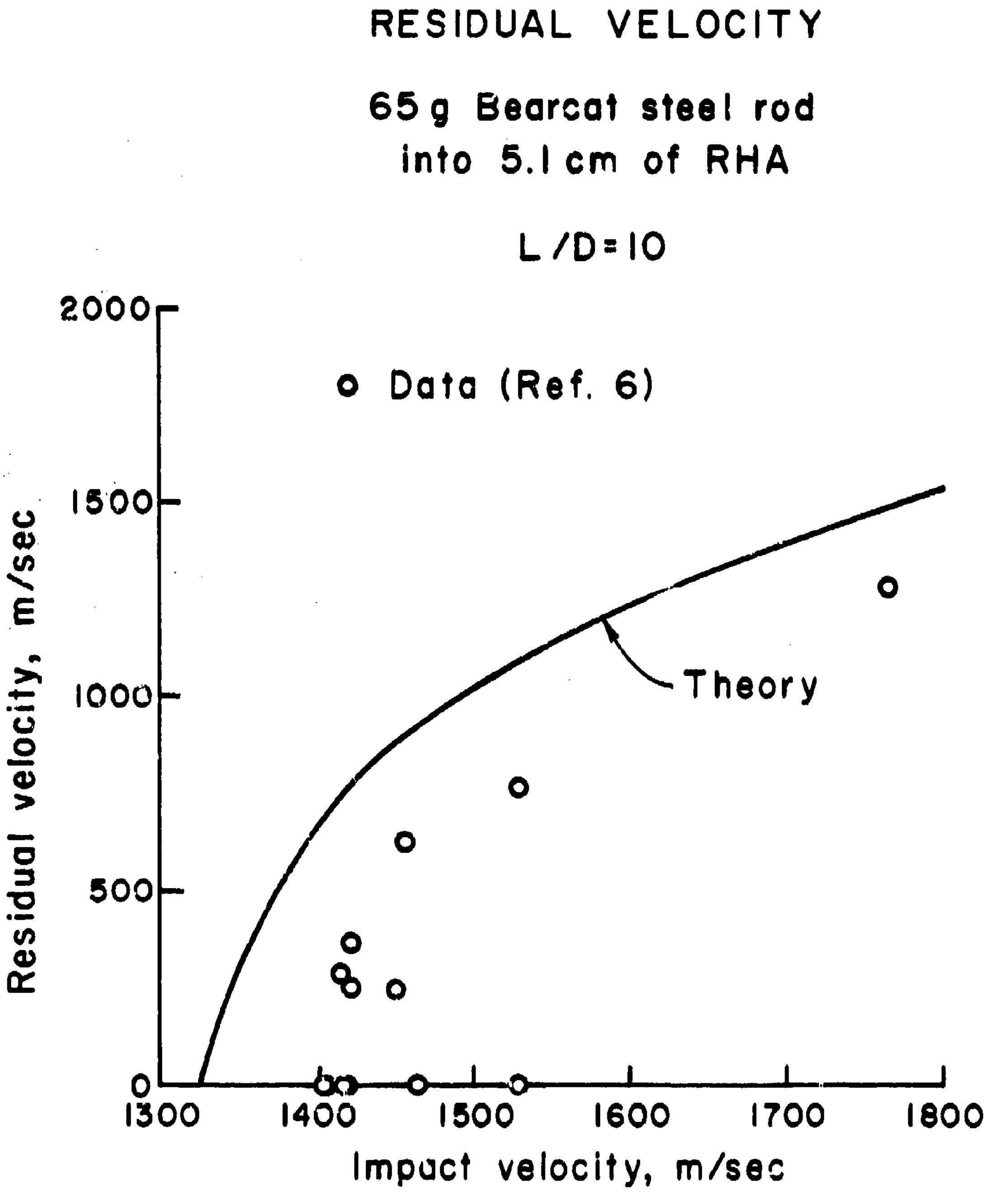
RESIDUAL VELOCITY
65 g Bearcat steel rod
into 5.1 cm of RHA
L/D=10
Data (Ref. 6)
Theory
Residual velocity, m/sec
Impact velocity, m/sec
2000
1500
1000
500
0
1300
1400
1500
1600
1700
1800

Figure 27

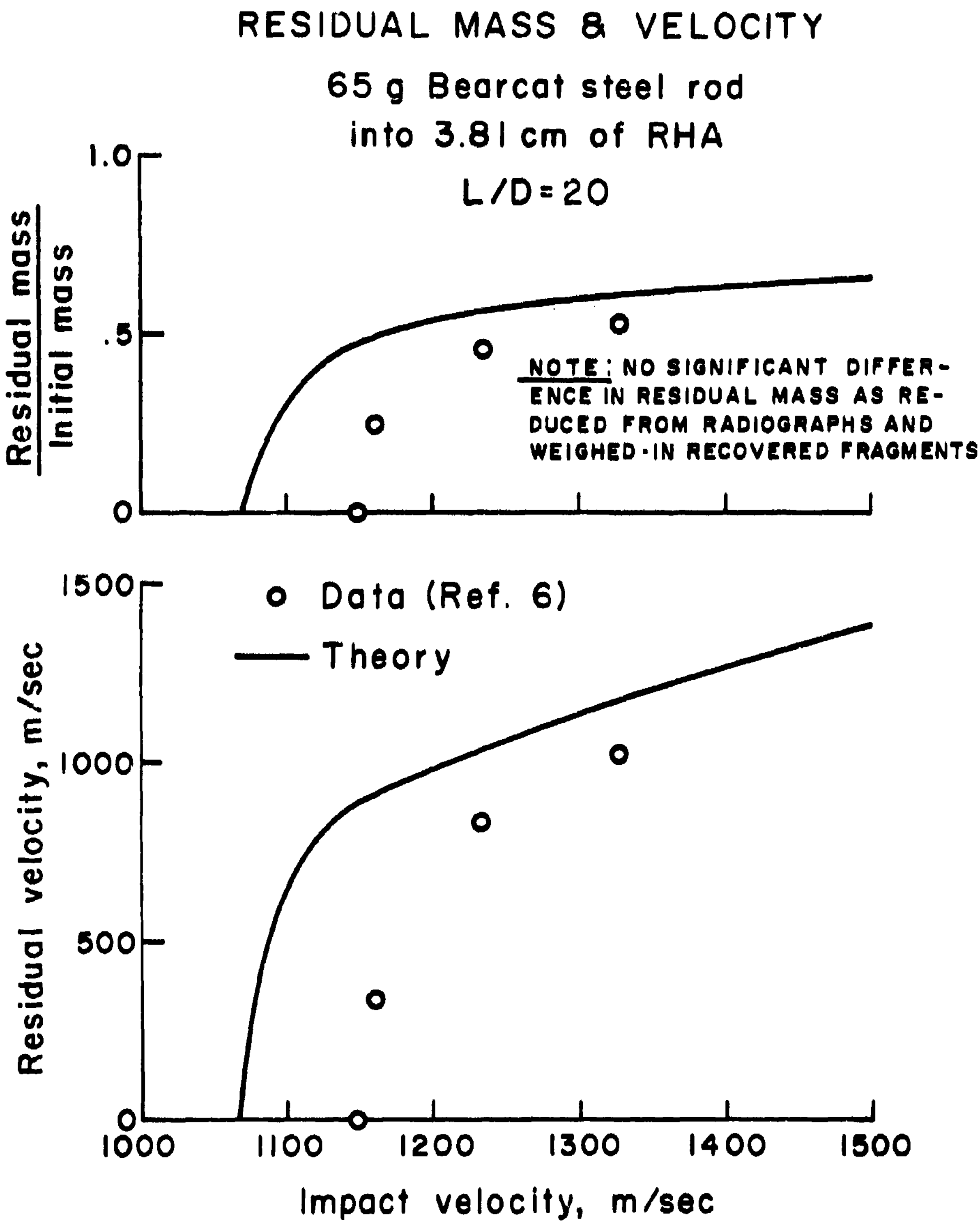
RESIDUAL MASS & VELOCITY
65 g Bearcat steel rod
into 3.81 cm of RHA
L/D=20
Residual mass / Initial mass
1.0
.5
0
NOTE: NO SIGNIFICANT DIFFERENCE IN RESIDUAL MASS AS REDUCED FROM RADIOGRAPHS AND WEIGHED-IN RECOVERED FRAGMENTS
Data (Ref. 6)
Theory
Residual velocity, m/sec
1500
1000
500
0
1000
1100
1200
1300
1400
1500
Impact velocity, m/sec

Figure 28

V. E_{*d} EXPERIMENTS

This chapter contains a description of an experimental program conducted at A.R.A.P. to measure the fundamental quantity E_{*d}. Recall that this quantity represents the dissipated energy absorbed by the penetrator material as it is transformed from the solid to the hydrodynamic state. In essence, E_{*d} is to the penetrator material what E_{*p} is to the target material. An experiment was designed by A.R.A.P. to measure both the total energy input to a material specimen prior to fracture and the residual nondissipated energy of the specimen (kinetic energy in the debris cloud) after fracture. The quantity E_{*d} can be obtained from these measurements.

In the next section, the experimental concept is described in more detail. In the following section, the experiment including apparatus, instrumentation, and test procedure is summarized. This is followed by a discussion of the results.

A. Test Concept

The long rod model which was described in Chapter IV contains the fundamental parameter E_{*d} which represents the dissipated energy absorbed by the penetrator material during impact. In addition, the model contains a parameter σ, the adiabatic yield stress, which is related to E_{*d} ($\sigma = \rho_p E_{*d}$, see Eq. (61)). Computations of long rod penetration are sensitive to σ and, therefore, to the value of E_{*d}.

One method to evaluate E_{*d} is to note that in the impact process for like materials the penetrator and target are undergoing similar pressures and deformations. Therefore, the energy dissipation mechanism in the penetrator material must be similar to that in the target material. The energy dissipation in the target is, of course, given by E_*. Since the flow fields in the target and penetrator are somewhat different, one would not expect that $E_{*d} = E_*$. However, it is reasonable to postulate that E_{*d} might be proportional to E_*. The constant of proportionality, which is denoted by χ in Eq. (60), then becomes a model coefficient and is evaluated by correlation of the model with data. This is the procedure which was described in the preceding chapter.

Another method is to attempt to measure E_{*d} directly. An experiment was designed by A.R.A.P. to measure each of the components of the energy partition associated with penetrator deformation and fracture. By writing an energy balance for the process, it is possible to deduce the value of E_{*d}.

During the impact process, material in the penetrator is being rapidly decelerated in the forward direction and accelerated in the lateral direction, so an inertial term which takes into account the kinetic energy, similar to the $C_D V^2/2$ term in the target material, will be present in the penetrator. Also, the penetrator absorbs elastic and plastic energy as it deforms. Hence, the energy balance prior to fracture may be written

$$W = K + E + P \quad \text{(prior to fracture)} \ , \tag{62}$$

where W denotes the total work done on the penetrator by the target, K is the kinetic energy, E is the elastic energy and P is the plastic energy. All energies are per unit mass.

If fracture occurs, a portion of the elastic work is converted into kinetic energy of the broken fragments. The remainder is dissipated at the tip of the crack and in running the crack and as surface energy of the newly created fracture surfaces. If melting occurs first, none of the elastic work is recovered as kinetic energy, and only plastic dissipation occurs. Thus, any elastic energy stored during impact will be recovered as kinetic energy, converted to fracture surface energy or dissipated plastically or during crack formation as the penetrator breaks. The energy balance after fracture may be written

$$W = K + E_{*d} \quad \text{(after fracture)} \ , \tag{63}$$

where E_{*d} is the total dissipated energy per unit mass. For many materials, E_{*d} may be thought of as consisting of two terms: E_{*dp} which represents the plastic work absorbed per unit mass, and E_{*df} which is the fracture energy per unit mass absorbed in the creation of fracture surfaces. Thus, the final energy balance may also be written as

$$W = K + E_{*dp} + E_{*df} \ . \qquad (64)$$

In this form, E_{*dp} includes the plastic dissipation during loading prior to crack formation as well as the energy dissipated to form the crack.

That E_{*d} should be an important factor in penetrator behavior during impact is clear from Eq. (63). The work done on the penetrator, if it is not absorbed in E_{*d}, goes directly into kinetic energy of the penetrator in the lateral direction. This leads to rapid spreading of the front face. Conversely, a material with a high E_{*d} will absorb the work done by the the target with less lateral spreading of the penetrator.

To simulate the partitioning of energy in the laboratory, an experiment was designed in which a material specimen is compressed between two anvils until fracture occurs. Measurement of the time history of the applied load and the deformation of the specimen yields the total work done on the specimen prior to fracture. Measurement of the kinetic energy associated with the particles in the debris cloud following comminution of the specimen yields a value for K in Eq. (63). The value of E_{*d} can then be obtained by subtracting K from W. Estimates of the energy dissipated during loading and of the fracture surface energy suggest that these two contributions to E_{*d} are small and that the primary energy dissipation mechanism for brittle materials is associated with crack formation.

B. Experimental Program

1. Apparatus - Figure 29 is a sketch of the E_{*d} apparatus. The apparatus consists of a rigid frame, load application hardware, fragment trap hardware, and instrumentation.

The frame consists of standard structural steel components. It measures approximately 55 inches high by 35 inches wide by 18 inches deep. The load application hardware and fragment trap hardware are mounted on and supported by various platforms which are fastened to the frame. To permit easy access to the test specimen, the frame rests on concrete blocks.

A schematic illustration of the load application hardware is shown in Figure 30. The material specimen, which in these tests is a spherical ball, is placed on the centerline of the

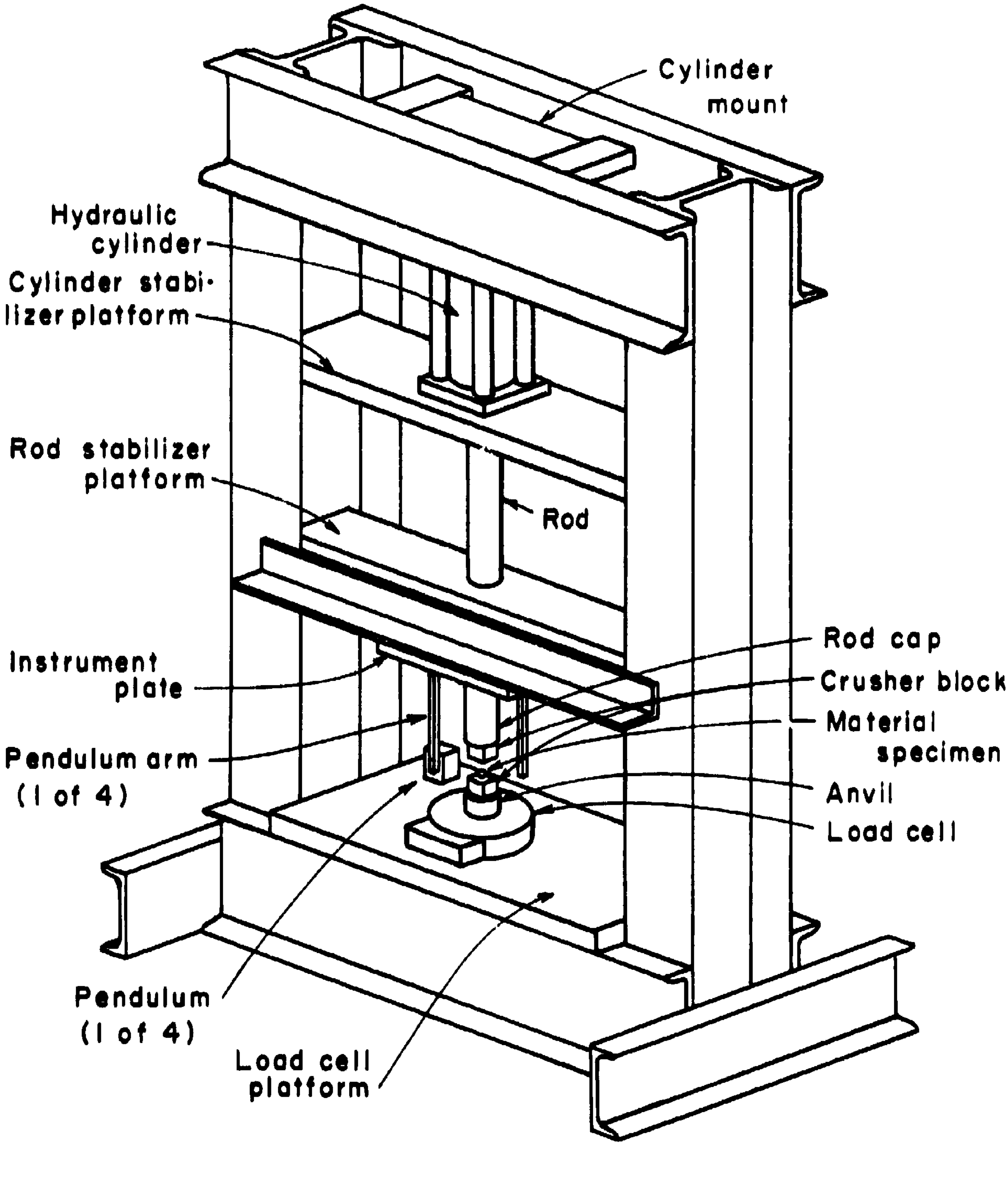

E_{*d} APPARATUS

Figure 29

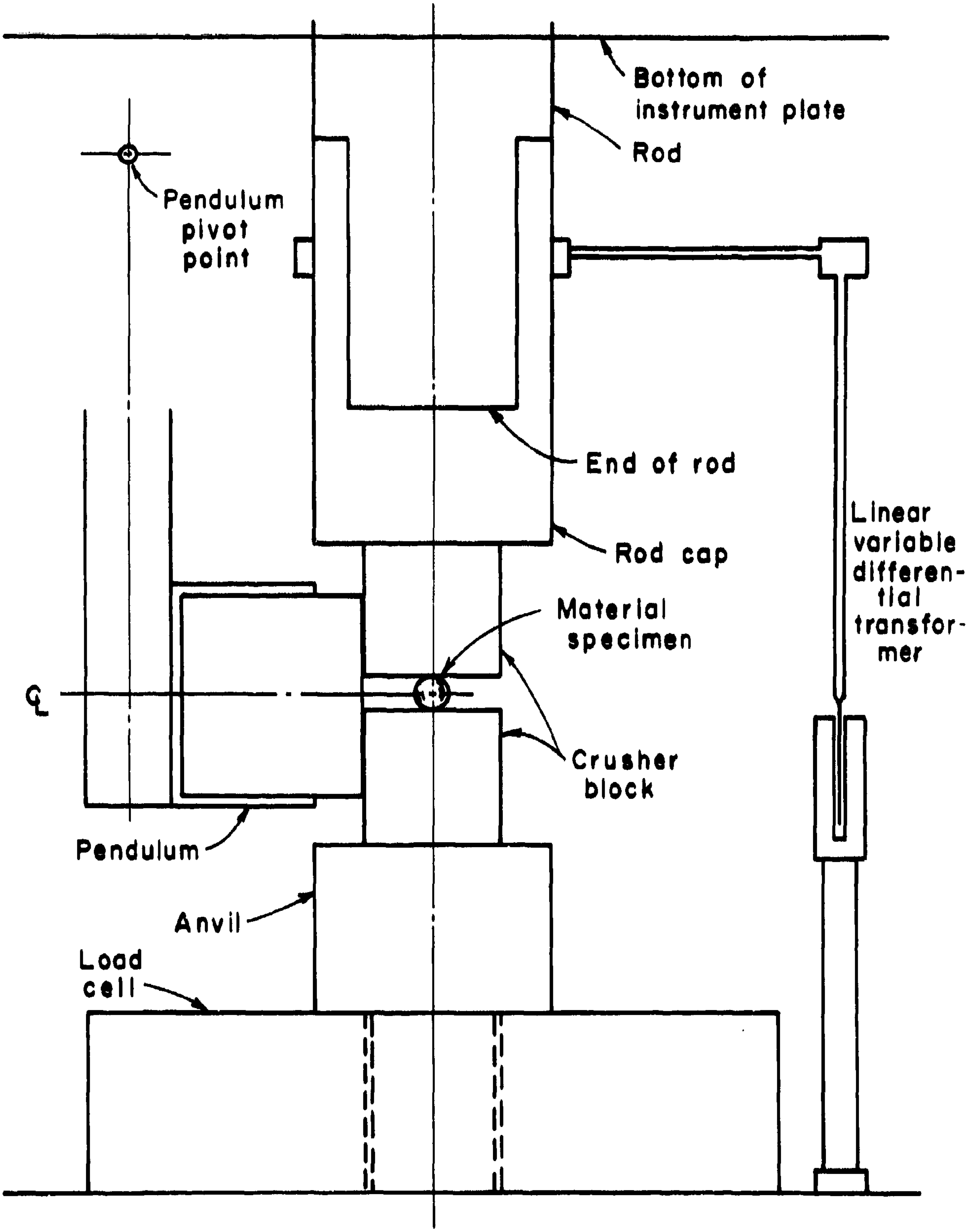

LOAD APPLICATION HARDWARE

Figure 30

apparatus between two crusher blocks. The blocks are 1-inch steel cubes which have a Rockwell hardness of C-55. Since compression of the ball produces a small permanent indentation in the blocks, each surface can be used for only one test.

Load is applied to the ball using a Hanna MT2 Hydraulic Cylinder. The cylinder has a bore diameter of 4.00 inches and a rod diameter of 1.75 inches. It can generate a maximum compressive load of approximately 25,000 lbf. The magnitude and rate of application of the load can be controlled by regulating the hydraulic pressure in the cylinder. The operating range for the cylinder is 200 psig to 2,000 psig. At the maximum cylinder pressure, the rod velocity is approximately 0.2 inches/second.

The cylinder is attached to the upper beams of the steel frame with a trunion mount. A cylinder stabilizer platform, located at the bottom of the cylinder, prevents rotation of the cylinder and maintains vertical alignment. Another platform, the rod stabilizer platform, is used to maintain vertical alignment of the rod. A nylon phenolic bushing in the center of the rod stabilizer platform permits freedom of movement for the rod. A compressive load is applied to the test specimen when the rod moves downward.

Load is transmitted from the rod to the top crusher block through a steel rod cap. This cap has a threaded hole to accept the end of the rod. The face of the rod rests flat on the inside surface of the cap. The top crusher block is ground flat and is pinned to the rod cap.

The bottom crusher block is pinned to a steel anvil which carries the load to the load cell. The anvil has a threaded male connection which fits the load cell. The load cell is, in turn, mounted on a steel platform which is fastened to the bottom beams of the frame.

Attached to the mid-section of the rod is a collar and fixture mount for the linear variable differential transformer (LVDT) which is used to measure the displacement of the rod. The LVDT measures the relative displacement between the rod and the load cell platform.

An instrument plate is mounted to the under side of the rod stabilizer platform. Four ballistic pendulums are hung from this plate. A drawing of one of the pendulums is shown in Figure 31(a). Each pendulum consists of a 1 in^3 balsa wood box with one side removed. A styrofoam block is placed in the box and the front surface - the surface exposed to the test

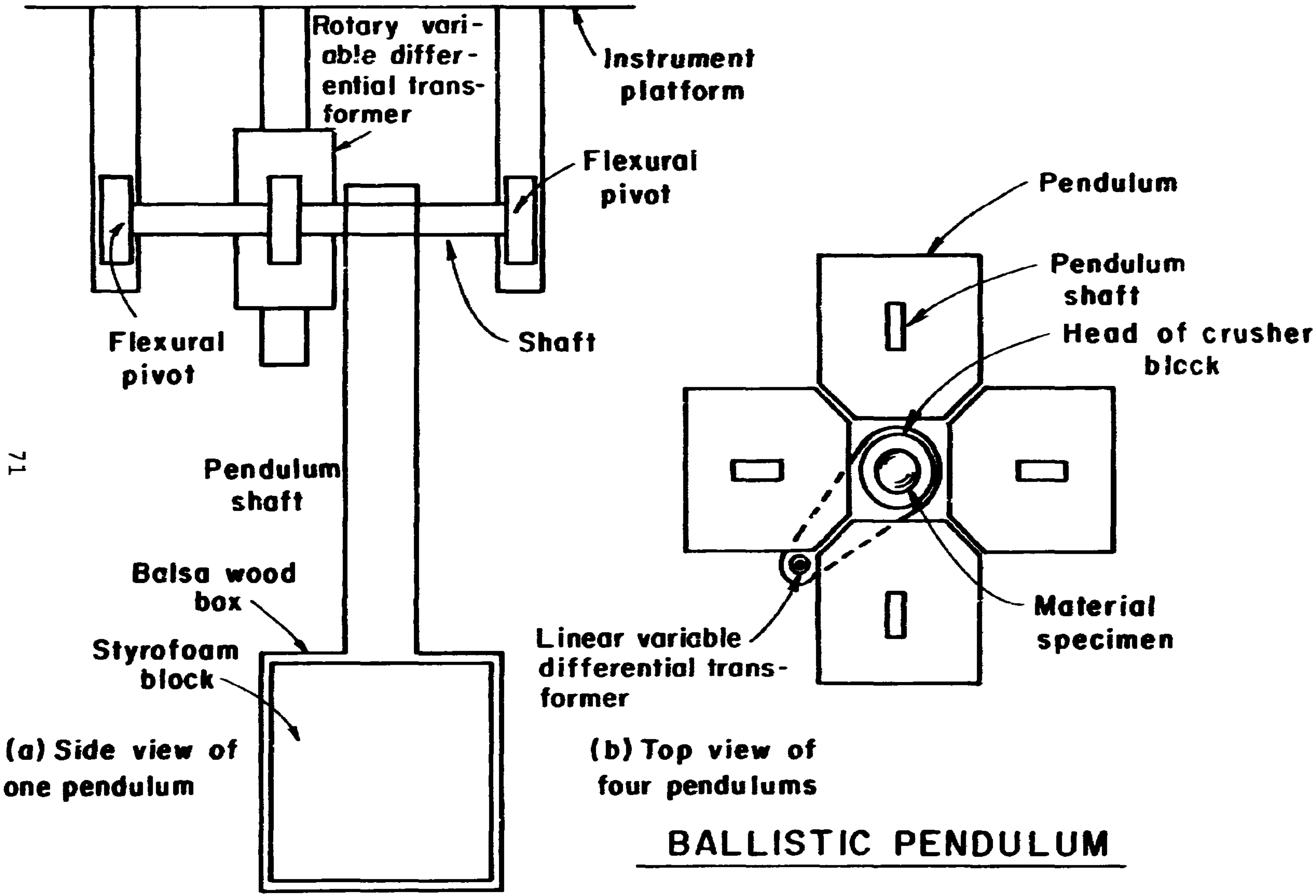

BALLISTIC PENDULUM

Figure 31

specimen - is coated with Dow silicone grease. The mass of the box and styrofoam is approximately 2.5 grams. Prior to impact, the front face of the styrofoam block is adjacent to but does not touch the crusher blocks (as shown in Figure 30). The four pendulums completely encircle the test specimen as shown by the schematic in Figure 31(b). For most of the tests, the pendulums captured more than 75% of the mass of the test specimen.

The arm of each pendulum is approximately four inches long and is made of plastic. For rigidity, the cross-section of the arm is made by gluing two I-beam cross-sections together at the flanges. Each pendulum hangs from a separate shaft which rotates when the pendulum is struck. Each end of the shaft is mounted in a frictionless pivot (Bendix Model 5008-400 Flexural Pivot) which acts as a torsional spring. The torsional spring rate of each pivot is 6.54 in-lbf/radian. The springs are designed to produce a 15 degree rotation when the pendulum is hit by a 1 gram fragment traveling at 75 feet per second. Also attached to each shaft is a rotary variable differential transformer (RVDT) to measure the angular rotation of the shaft.

2. Instrumentation - The instrumentation consists of one load cell, one LVDT, four RVDT's, and one recording device.

The load cell is a Strainsert Universal Flat Load Cell (Model No. FL25U-3SG). It is a single bridge design with a maximum capacity of 25,000 lbf. The cell is excited by a 12 V battery and produces a DC-voltage output. It has been calibrated against a Bourdon pressure gauge which measures the pressure in the hydraulic cylinder and is linear over the full range of application within 0.5% of full scale.

The displacement of the test specimen is measured with a Trans-Tek Model 241-000 Displacement Transducer. The transducer is an integrated package consisting of a precision linear variable differential transformer, a solid state oscillator, and a phase-sensitive demodulator. The LVDT is a transducer that converts mechanical displacement into electrical output. The core, when displaced axially within the coil assembly, produces a voltage change in the output directly proportional to the displacement of the core. This model which is excited by a 12 V battery has a working range of 0.1 inches and is accurate to 0.5% of full scale.

The rotation of the shaft is measured by a Pickering Model No. 21300 Precision Rotary Variable Differential Transformer.

This transducer converts a mechanical angular displacement into an electrical output by means of an electrical input carrier. It consists of a rotor assembly to which the shaft is attached and a stator assembly in which all windings are contained. The electrical input is a 10 KHz, 3 V RMS AC signal which is generated by a Hewlett-Packard Oscillator. The output signal is also AC and is converted to DC external to the transducer using a separate demodulation circuit. The RVDT is linear over a displacement range of ± 10°.

The voltage output from each of the six instruments is applied to a separate mirror galvanometer circuit. Each RVDT uses a Honeywell M40-120A galvanometer. The load cell uses an M40-350A and the LVDT used an M400-120. The current which passes through the galvanometer circuit is controlled by external series and shunt resistances. The galvanometers are extremely sensitive to small changes in the signal current.

The galvanometers are contained in a Honeywell (Model 906C) Direct Recording Visicorder Oscillograph. This device transforms the input signal into a moving beam of light through use of the mirror galvanometers. It uses an ultraviolet light source which is focused by an optical system on recording paper which is highly sensitive to ultra-violet light. Thus, data readout is immediately available. The paper speed is controllable and, since the device has 14 channel capability, each output trace can be placed on the same strip of paper.

3. Test procedure - Prior to a test, each test specimen is carefully weighed and measured and is then placed at the center of the bottom crusher block. A thin coat of Dow silicone grease is applied to one surface of each styrofoam block, and the block is then weighed. The rod is positioned such that the top crusher block is approximately one inch above the test specimen and the pressure in the cylinder is set to give the desired loading rate.

The oscillograph is actuated at the instant the cylinder rod begins moving. Note that the top crusher block is moving downward when it comes in contact with the test specimen. Load is applied until the ball fractures or the rod bottoms-out.

After the test, the styrofoam blocks are carefully removed and weighed to determine the mass of the pieces which impacted the blocks. Any debris which remains on the crusher blocks is also collected and weighed. Finally, the crusher blocks are removed, and the depth of the indentation is

measured using a dial indicator gauge.

4. Data analysis - The oscillograph provides a continuous time history of the load and deflection. Recall that the LVDT shown in Figure 30 actually measures the position of the bottom of the rod relative to the top of the load cell platform. Therefore, the deflection measurement includes the indentation of the crusher blocks. (The displacement of the rod cap, anvil and load cell are negligible.) The area beneath the force-deflection curve up to rupture represents the total work done on the ball and the crusher blocks.

Equation (62) which describes the energy balance based on a rigid crusher block must be modified to account for energy absorption by the blocks. Both elastic and plastic work is done on the blocks. It is assumed that the stored elastic energy is returned to the ball when the ball fractures. However, the plastic work is dissipated in the blocks. Hence, for a non-rigid crusher block the energy equation may be written

$$W = K + E_{*d} + E_{db} , \tag{65}$$

where E_{db} represents the energy dissipation in the crusher blocks.

The quantity E_{db} can be estimated by testing a rigid ball. Figure 32 shows the load-deflection response of the system when a tungsten carbide ball is compressed through five cycles of loading and unloading. At the end of each cycle there is no measureable plastic deformation of the ball so that the measured deflection represents the total indentation of the crusher blocks. For each cycle, the area beneath the loading curve is the total work done on the system; the area beneath the unloading curve is the recovered elastic energy. The difference between the two represents the energy dissipation in the blocks. Figure 33 shows this result as a function of the depth of the indentation.

The oscillograph trace of the RVDT response is essentially a step pulse followed by a damped oscillation. The magnitude of the pulse which is calibrated to the rotation of the pendulum can be used to estimate the kinetic energy of the impacting particles. It is assumed that all of the pieces which impact a given pendulum can be lumped together to form an average particle which has a mass, m_{proj}, equal to the total mass of all the pieces and a translational velocity, V_{proj}, normal to the face of the pendulum. The lumping of all

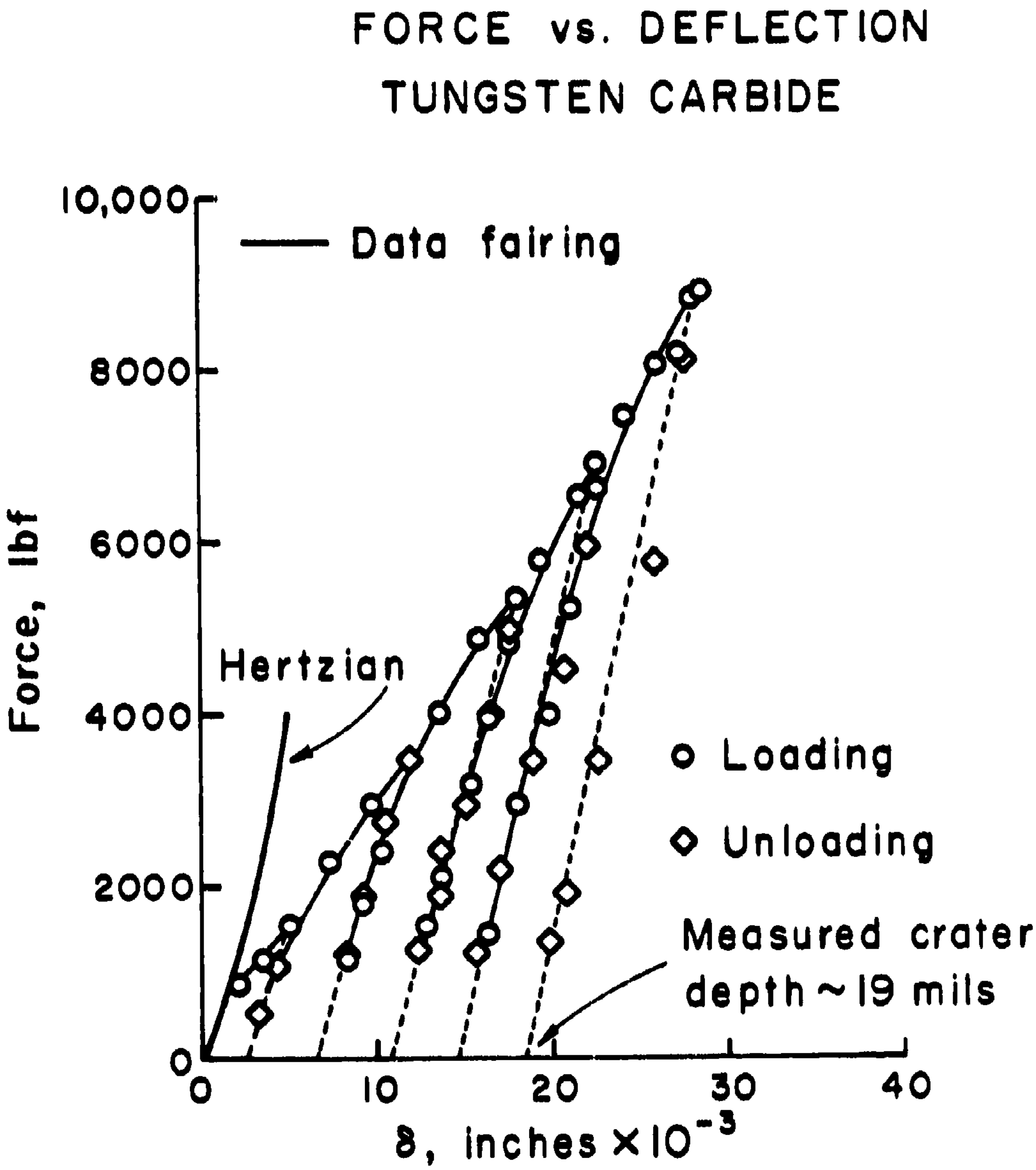
FORCE vs. DEFLECTION
TUNGSTEN CARBIDE
10,000
8000
6000
4000
2000
0
Force, lbf
— Data fairing
Hertzian
o Loading
◇ Unloading
Measured crater
depth ~ 19 mils
0
10
20
30
40
δ, inches × 10⁻³

Figure 32

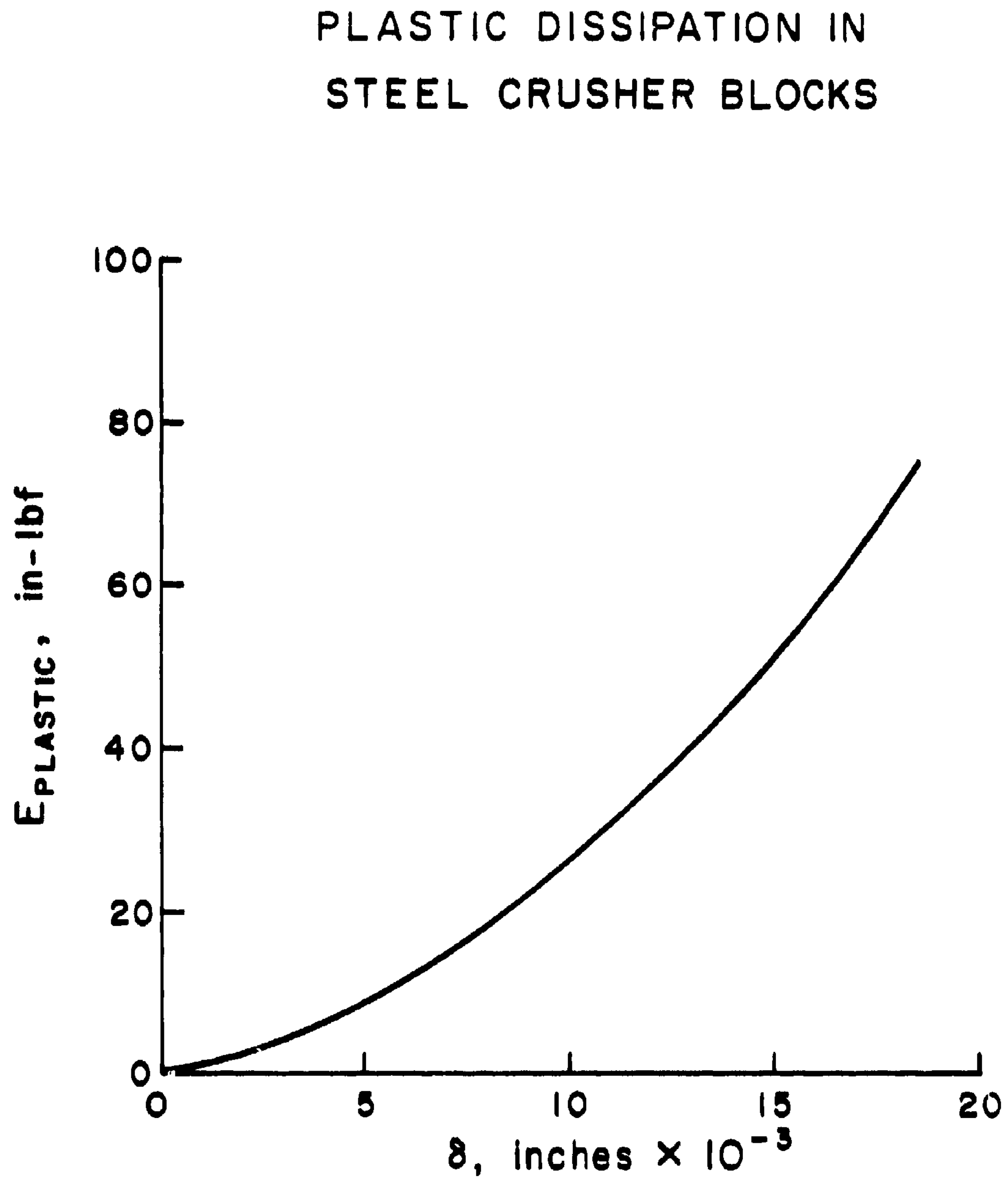
PLASTIC DISSIPATION IN
STEEL CRUSHER BLOCKS
100
80
60
40
20
0
0
5
10
15
20
E PLASTIC, in-lbf
δ, inches × 10⁻³

Figure 33

of the debris into one average piece is admittedly a simplification. However, the error is minimized by removing from consideration those tests in which the RVDT loading pulse was jagged. Neglect of the tangential component of the impact velocity introduces an error of approximately 15% in the estimate for V_{proj}. This error was estimated based on an angle of approximately 45° between the center of the ball and the side of the styrofoam block and an angle of less than 15° to the top of the block.

The kinetic energy of the debris can be obtained from the conservation equations as follows. The momentum equation may be written

$$m_{proj} V_{proj} = (m_{proj} + m_{box}) V_{box} , \tag{66}$$

where m_{box} is the mass of the pendulum and V_{box} is the initial velocity of the pendulum. The energy equation may be written

$$\frac{1}{2}(m_{proj} + m_{box})V_{box}^2 = (m_{proj} + m_{box})gL(1-\cos\theta_m)+\frac{1}{2}k_s\theta_m^2 , \tag{67}$$

where the first term on the right accounts for the change in potential energy as the pendulum swings through an arc of θ_m degrees (L is the length of the pendulum). The second term represents the torsional energy stored in the springs of the flexural pivots. Frictional losses in the system are accounted for by using a calibration value for k_s. This value is within 4% of the nominal spring constant for each pendulum. For small rotations (i.e., less than 10°) the potential energy term in Eq. (67) can be ignored. Thus,

$$V_{box}^2 = \frac{k_s\theta_m^2}{m_{proj} + m_{box}} \tag{68}$$

The initial velocity of the pendulum can be obtained from the measured mass, the angular displacement of the pendulum and the known spring constant. Thus V_{proj} can be obtained from Eq. (66) and K , the kinetic energy of the particles, can

be obtained from

$$K = \frac{1}{2} m_{proj} V^2_{proj} . \qquad (69)$$

5. Test program - Table 4 summarizes the materials which were investigated and the pertinent results. A detailed discussion of the results is presented in the next section.

C. Test Results

1. Borosilicate (Pyrex) glass - Figures 34 - 36 show the force-deflection data for borosilicate glass (Corning 7740 polished pyrex) spheres for three strain rate regimes. For the purposes of this report, the strain rate is defined as an average value for the entire test

$$\dot{\varepsilon} = \frac{\delta / d_o}{t_r} , \qquad (70)$$

where δ is the measured displacement, d_o is the initial diameter of the ball and t_r is the time to rupture. Figure 34 shows the data for four tests which were performed at approximately the same strain rate. This figure suggests the degree of repeatability of the data. Three of the four loading curves virtually overlap. However, the rupture load differs by approximately 350 lbf, and the deflection at rupture by approximately .002 inches between the tests. For reference purposes, the classical solution to the problem is also shown. This solution which was first derived by Hertz can be found in Ref. 7.

Figure 35 shows the loading data for tests at three intermediate strain rates, and Figure 36 shows the data for the highest strain rates which were achieved. The rupture load and the deflection at rupture for each of these tests is shown in Figure 37. Although there is considerable scatter

7. Bergstrom, B. H. and Sollenberger, C. L.: Kinetic Energy Effect in Single Particle Crushing; Presented at the AIME Meeting, St. Louis, February 1961.

TABLE 4.

E_{*d} TEST PROGRAM

MATERIAL	DIAMETER (in)	NO. OF TESTS	STRAIN RATE (sec^{-1})	E_{*d}/W
Alumina (99.9% pure)	.25"	5	.01-.58	.96-.99
Borosilicate Glass (Pyrex)	.25"	14	.003-.3	.82-.88
Soda Lime Glass	.25"	11	.01-.35	.85-.91
Soda Lime Glass	.5 "	5	.004-.1	.62-.78
Steel (1013)	.25"	2	~1	1
Steel (52100)	.25"	6	.03-.11	~1
Tungsten Carbide	.25"	3	.06-.09	~.99
Aluminum (1100)	.25"	2	~1	1
Aluminum (2017)	.25"	2	~1	1
Polycarbonate (Lexan)	.25"	2	~1	1
Cast Acrylic	.25"	1	.69	~1
Cast Phenolic	.25"	2	.18-.40	.97-1

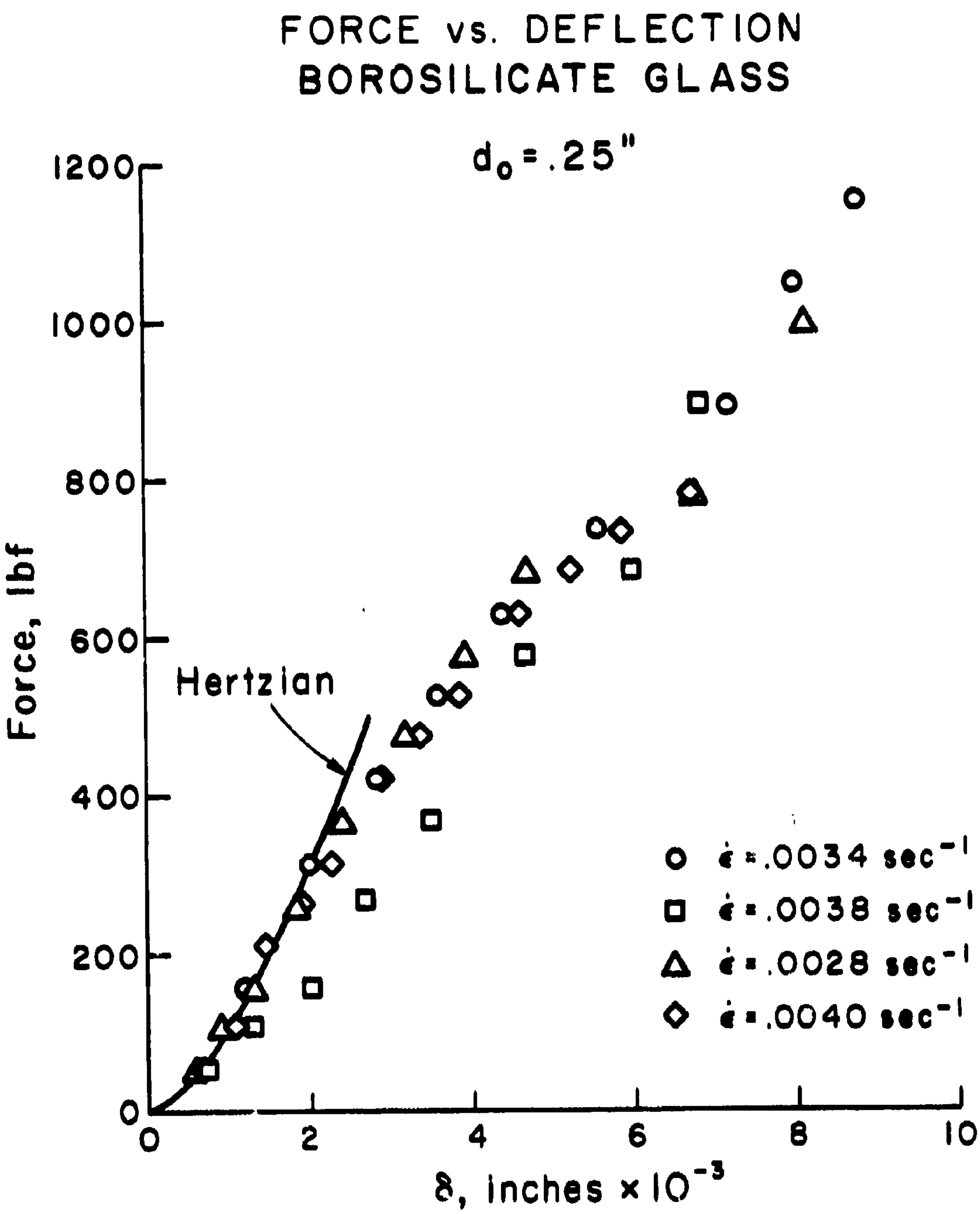
FORCE vs. DEFLECTION
BOROSILICATE GLASS
d₀ = .25"
Force, lbf
δ, inches × 10⁻³
Hertzian
ε̇ = .0034 sec⁻¹
ε̇ = .0038 sec⁻¹
ε̇ = .0028 sec⁻¹
ε̇ = .0040 sec⁻¹
0
200
400
600
800
1000
1200
2
4
6
8
10

Figure 34

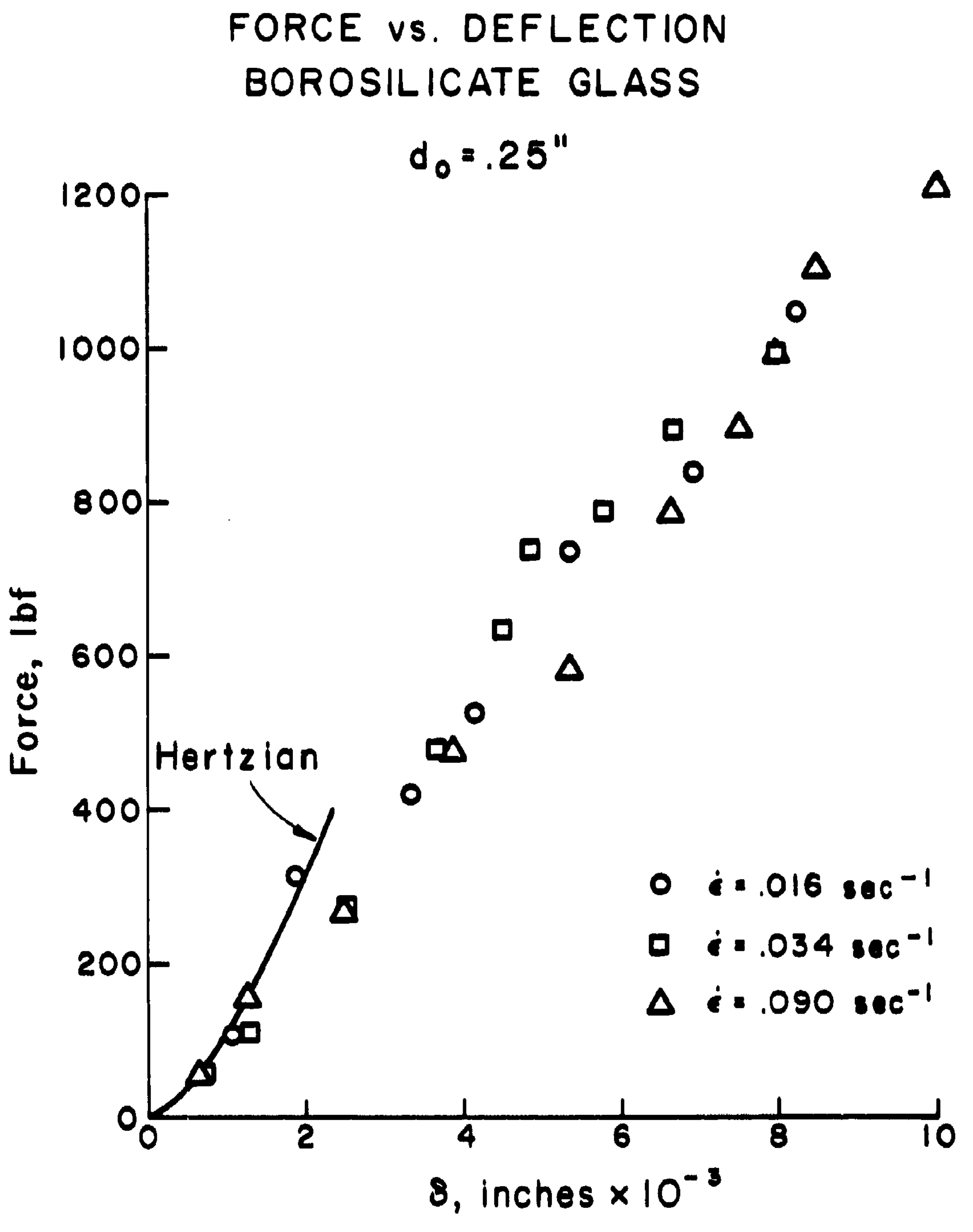
FORCE vs. DEFLECTION
BOROSILICATE GLASS
d_o = .25"
1200
1000
800
600
400
200
0
Force, lbf
Hertzian
0
2
4
6
8
10
δ, inches × 10^{-3}
$\dot{\epsilon}$ = .016 sec^{-1}
$\dot{\epsilon}$ = .034 sec^{-1}
$\dot{\epsilon}$ = .090 sec^{-1}

Figure 35

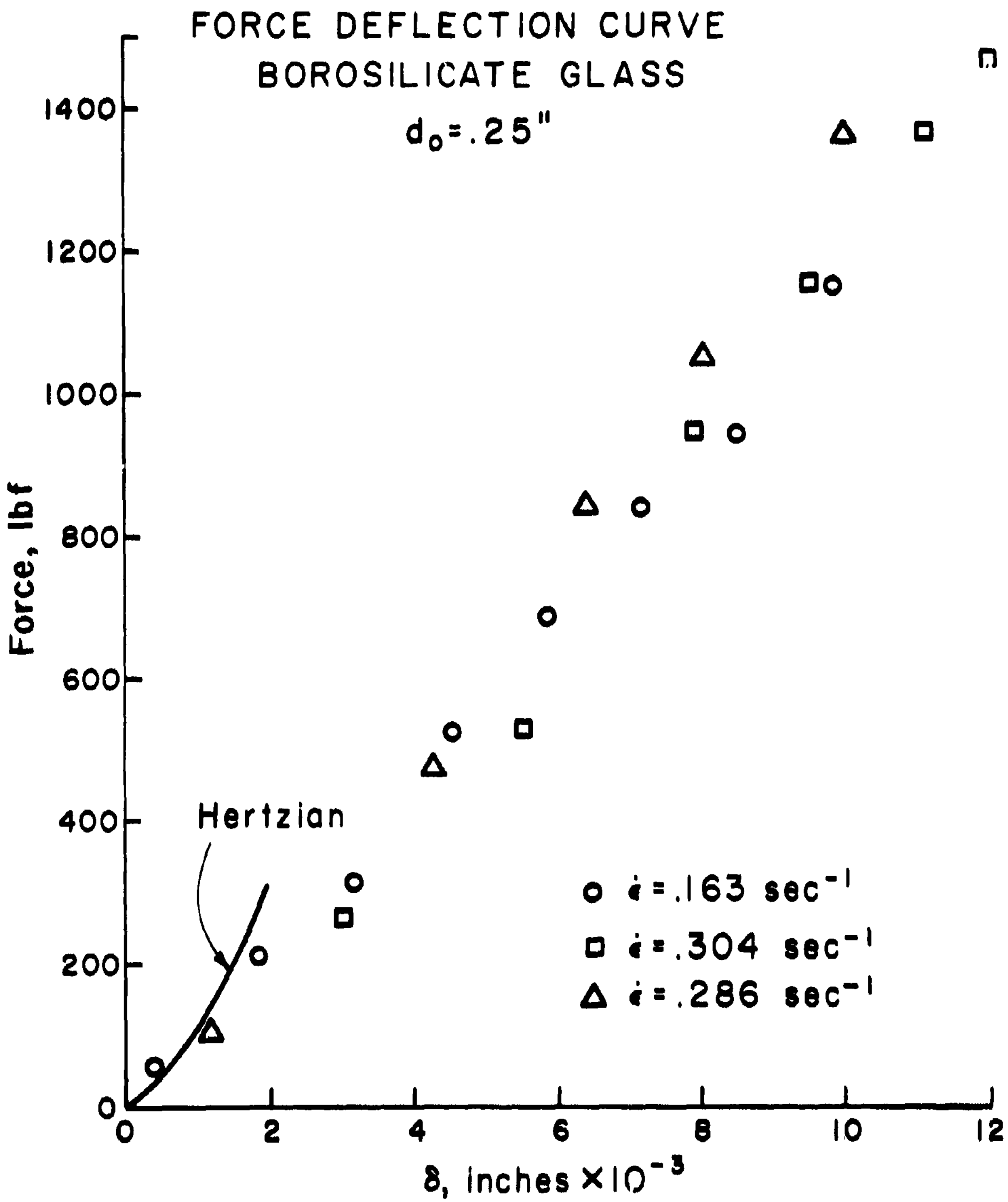
FORCE DEFLECTION CURVE
BOROSILICATE GLASS
$d_o = .25''$
Force, lbf
1400
1200
1000
800
600
400
200
0
Hertzian
$\dot{\epsilon} = .163\ sec^{-1}$
$\dot{\epsilon} = .304\ sec^{-1}$
$\dot{\epsilon} = .286\ sec^{-1}$
0
2
4
6
8
10
12
δ, inches $\times 10^{-3}$

Figure 36

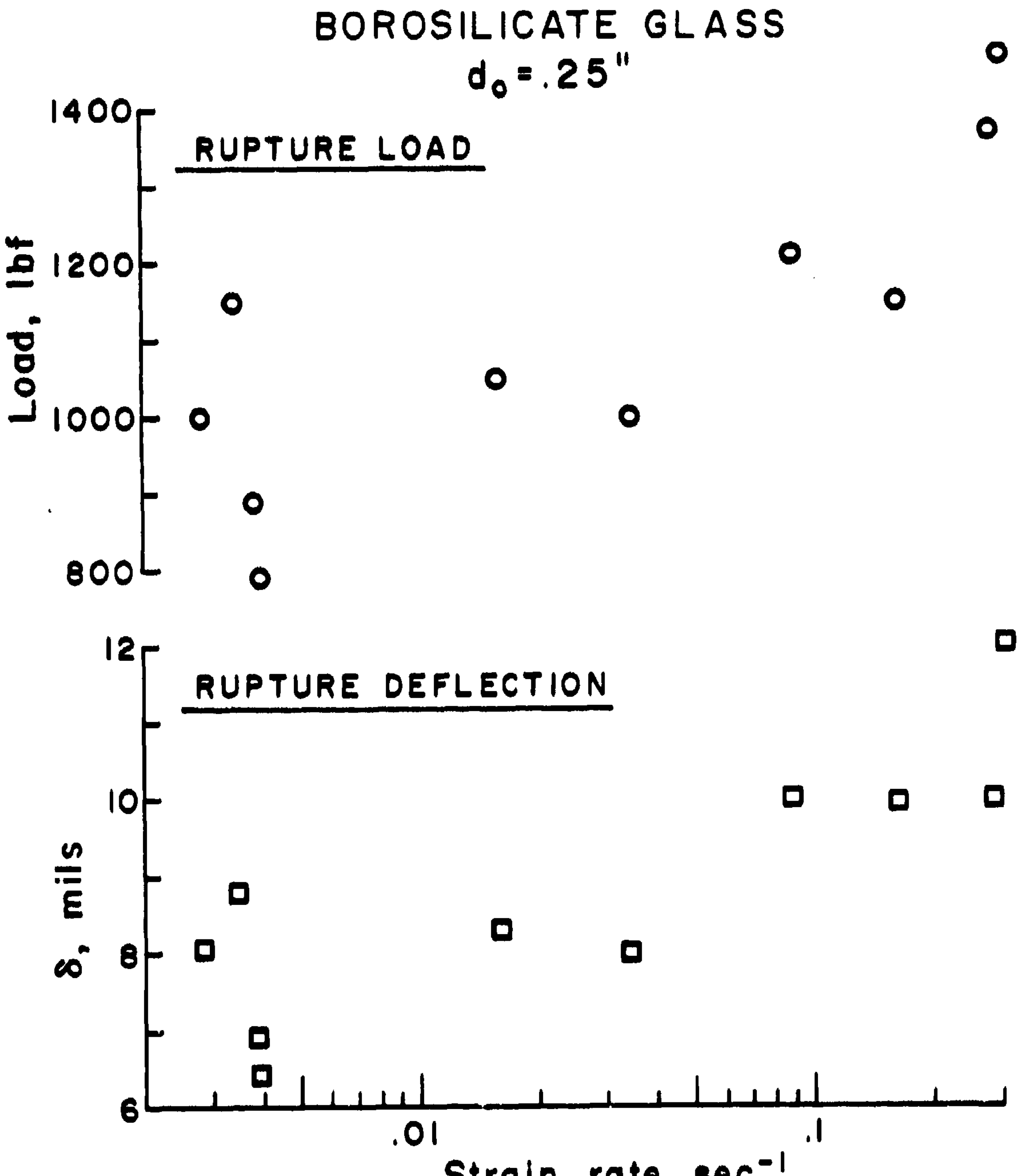

BOROSILICATE GLASS
d_o=.25"
RUPTURE LOAD
Load, lbf
1400
1200
1000
800
RUPTURE DEFLECTION
δ, mils
12
10
8
6
.01
.1
Strain rate, sec^{-1}

Figure 37

in the data, there does appear to be a discernable trend toward increasing rupture load and deflection at the higher strain rates.

The area beneath the loading curve represents the total work done on the test specimen and crusher blocks. Figure 38(a) shows these results and, again, there appears to be a tendency for W to increase with strain rate. Where does this energy go when the ball is fractured? Figure 38(b) shows the measured kinetic energy and Figure 38(c) shows the ratio of the kinetic energy to the work done. For this material and these strain rates, approximately 15% of the work is recovered as non-dissipative kinetic energy. It is important to note that this percentage appears to be roughly constant for this range of strain rates. Keep in mind that this percentage is probably somewhat low for the reasons discussed earlier, and also because the kinetic energy associated with particles which rebound between the crusher blocks is not measured. The mass not captured by the pendulums is generally less than 20% of the ball mass so this error cannot be much larger than 20%. Even if the kinetic energy measurement is in error by a factor of two, however, it is clear that more than 70% of the work is dissipated.

Energy can be dissipated in various modes such as heat or in free surface energy or to initiate and run cracks. Estimates for the energy dissipation via some of these modes can be made. Figure 39 shows one cycle for a test in which the load was released prior to fracture. The unloading curve overlaps the loading curve. Hence, there is no plastic dissipation in the ball prior to fracture. The indentation in the crusher blocks was less than .001 inches. Hence, the dissipation in the crusher blocks was less than 10% of the total work. An estimate was also made of the energy associated with the surface area created during the fracture. A test was conducted in which all of the broken pieces were collected, and an estimate was made of the total surface area. Based on a theoretical value for the free surface energy per unit area for glass of 1.7×10^3 ergs/cm^2, it was estimated that less than 1% of the total work was converted to free surface energy. Thus, nearly all of the dissipated energy was associated with the formation and running of the cracks.

2. Soda lime glass - The loading curves for soda lime glass (d_o = .25 inches) are shown in Figures 40 and 41 for two strain rate regimes. The rupture load and the total deflection at rupture for these tests is summarized in Figure 42. In general, the rupture load is considerably

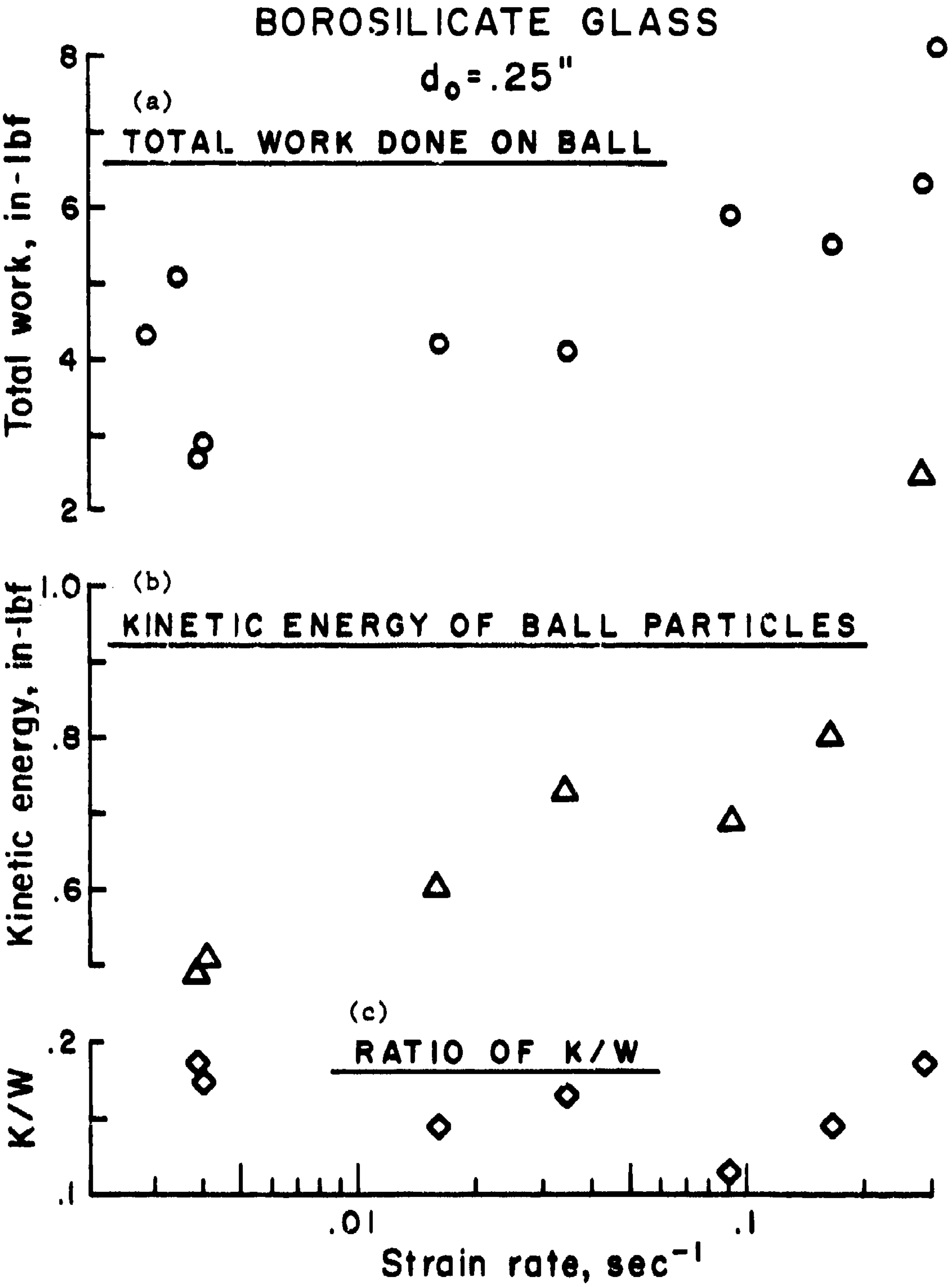
BOROSILICATE GLASS
d_o=.25"
(a)
TOTAL WORK DONE ON BALL
Total work, in-lbf
8
6
4
2
(b)
KINETIC ENERGY OF BALL PARTICLES
Kinetic energy, in-lbf
1.0
.8
.6
(c)
RATIO OF K/W
K/W
.2
.1
.01
.1
Strain rate, sec^{-1}

Figure 38

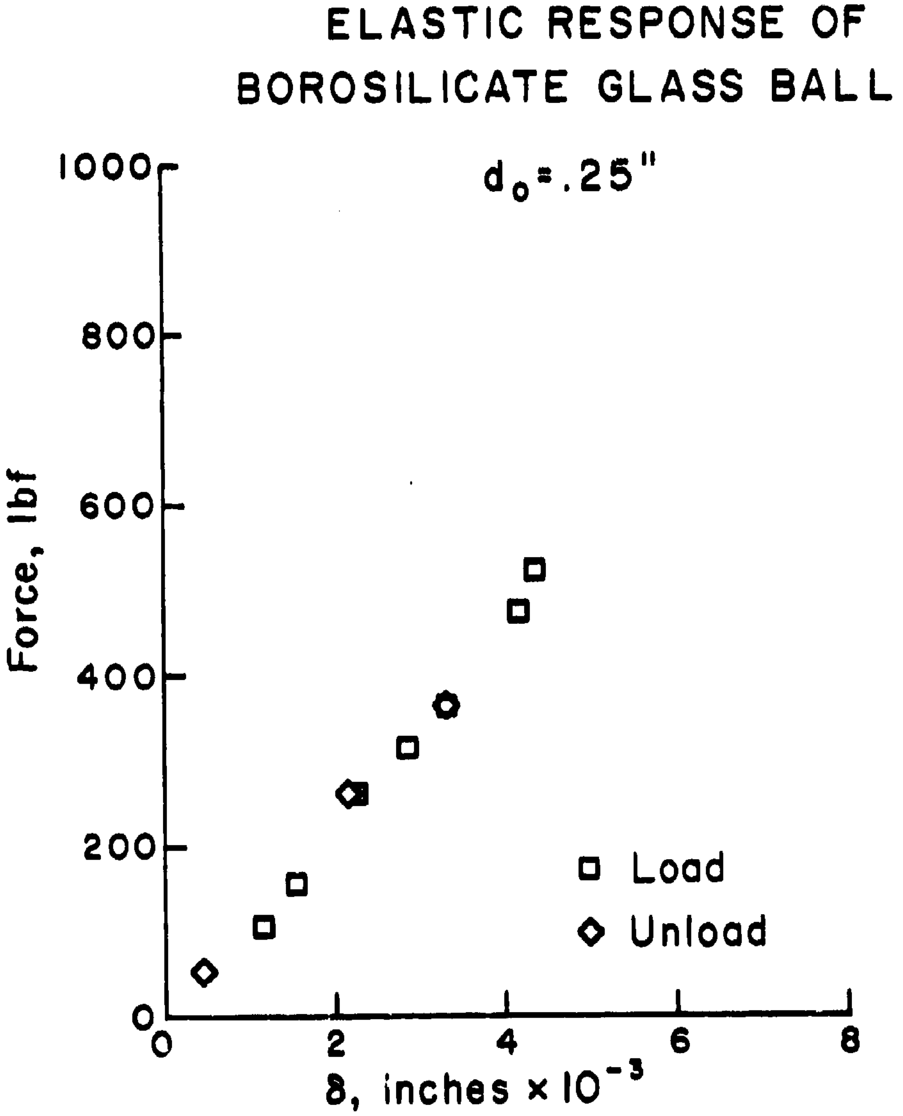
ELASTIC RESPONSE OF
BOROSILICATE GLASS BALL
d₀=.25"
1000
800
600
400
200
0
Force, lbf
0
2
4
6
8
δ, inches × 10⁻³
Load
Unload

Figure 39

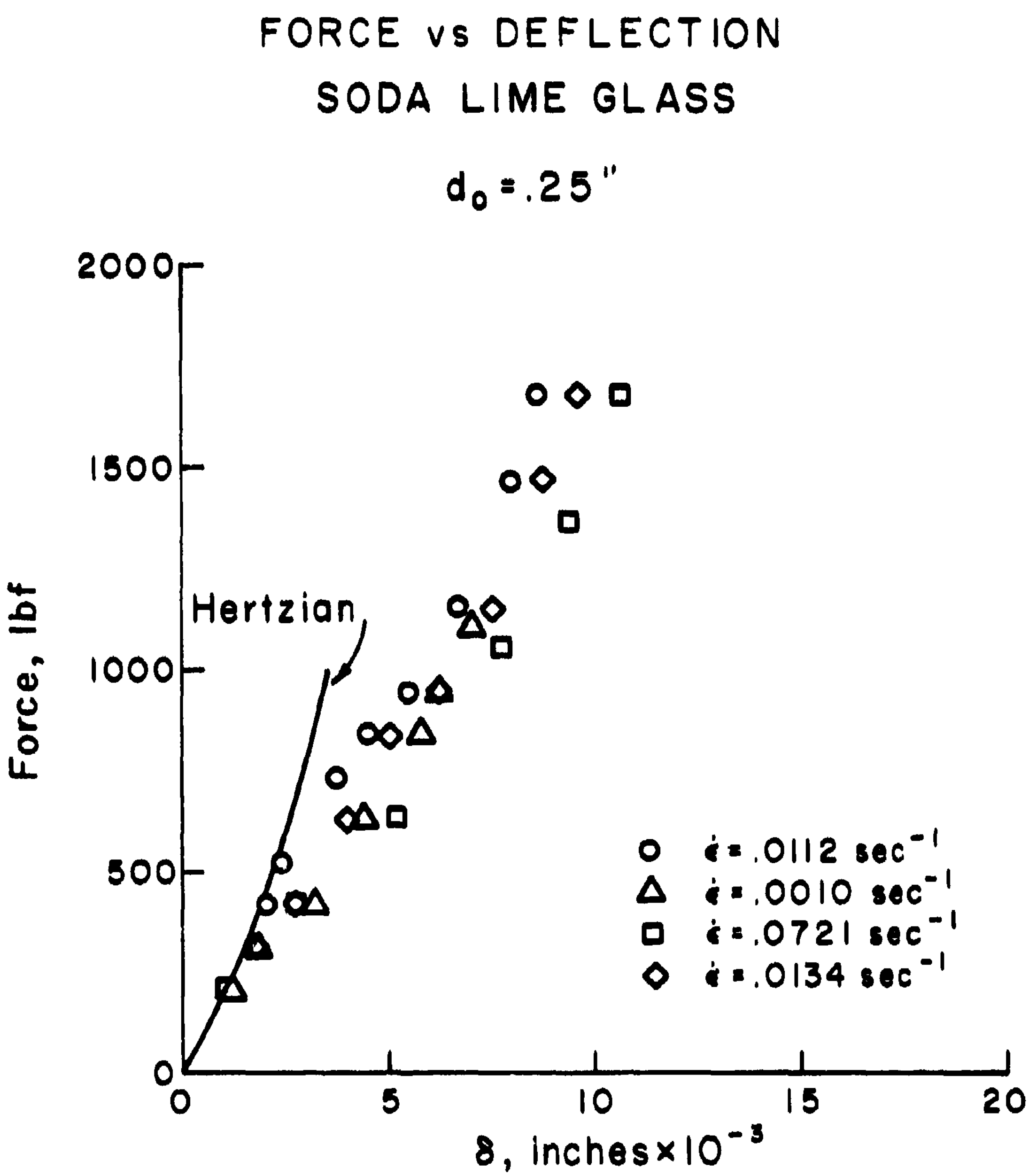

FORCE vs DEFLECTION
SODA LIME GLASS
d₀ = .25"
2000
1500
1000
500
0
Force, lbf
Hertzian
ε̇ = .0112 sec⁻¹
ε̇ = .0010 sec⁻¹
ε̇ = .0721 sec⁻¹
ε̇ = .0134 sec⁻¹
0
5
10
15
20
δ, inches×10⁻³

Figure 40

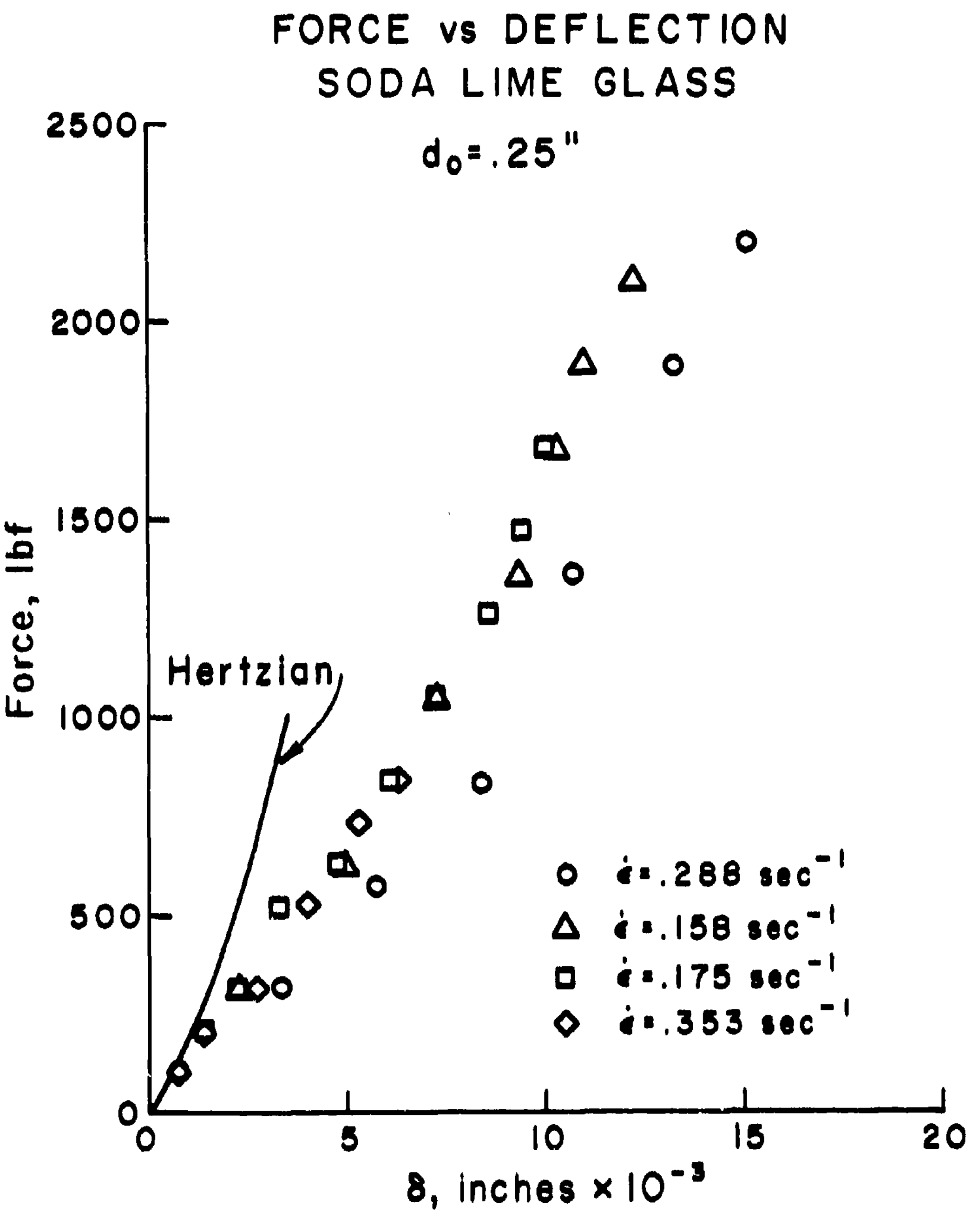
FORCE vs DEFLECTION
SODA LIME GLASS
d_o=.25"
Force, lbf
2500
2000
1500
1000
500
0
Hertzian
$\dot{\epsilon}$=.288 sec^{-1}
$\dot{\epsilon}$=.158 sec^{-1}
$\dot{\epsilon}$=.175 sec^{-1}
$\dot{\epsilon}$=.353 sec^{-1}
0
5
10
15
20
δ, inches × 10^{-3}

Figure 41

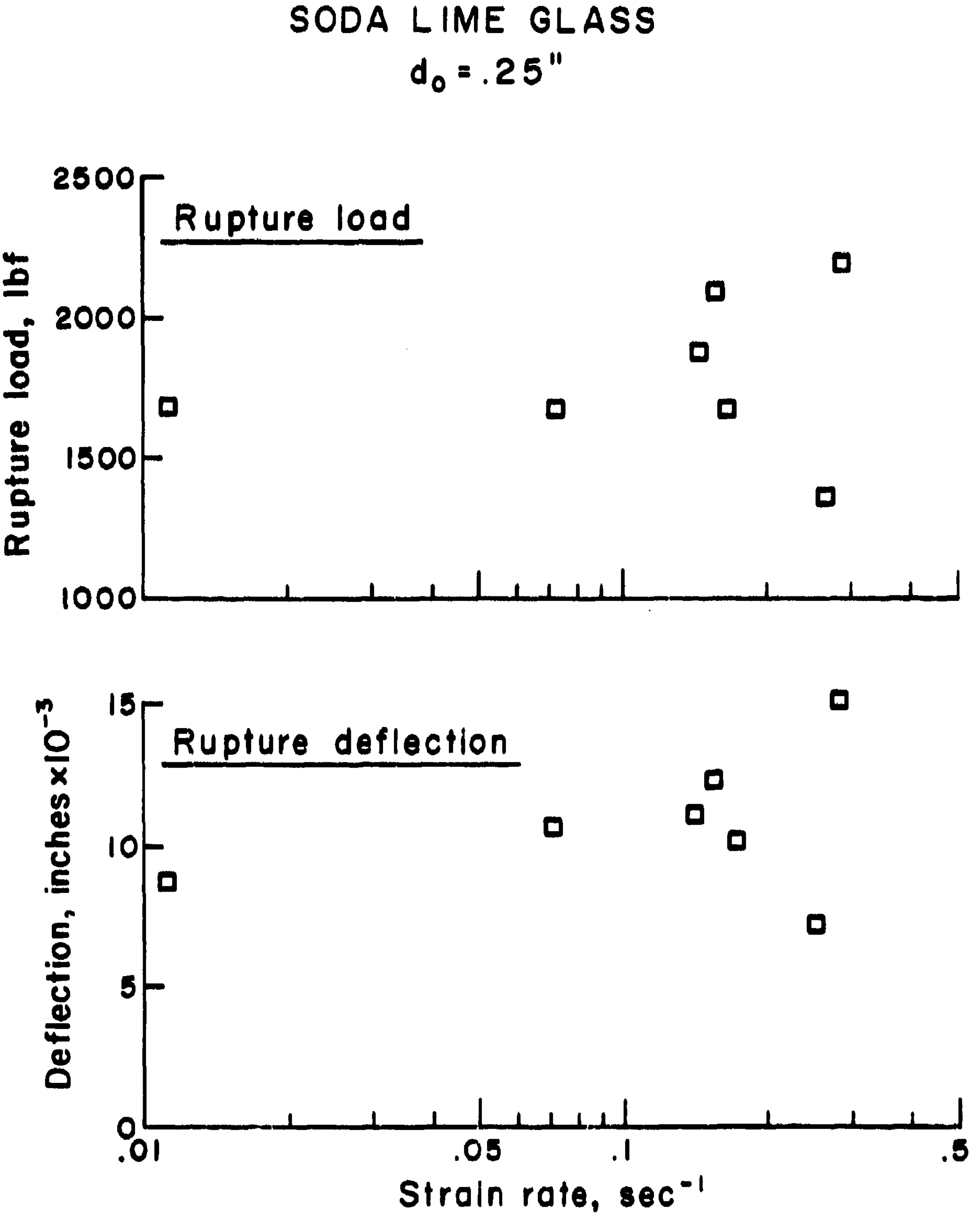
SODA LIME GLASS
d₀ = .25"
Rupture load
Rupture load, lbf
2500
2000
1500
1000
Rupture deflection
Deflection, inches x10⁻³
15
10
5
0
.01
.05
.1
.5
Strain rate, sec⁻¹

Figure 42

higher for this glass than for the borosilicate glass, although the deflections at rupture are comparable. The partitioning of energy is shown in Figure 43. It is clear that less than 15% of the total work was recovered as non-dissipative energy. Thus, nearly 85% of the energy was dissipated. Again, the plastic dissipation during deformation, the plastic dissipation in the crusher blocks, and the fracture surface energy were a small percentage of the total energy dissipation. The bulk of the energy was dissipated during the formation and running of the cracks. Also note that the ratio of K/W is approximately constant for this range of strain rates.

A series of tests was also conducted on larger soda lime glass balls (d_o = 0.5 inches). The loading data for these tests are shown in Figure 44. There appears to be a definite tendency for the rupture load to increase with strain rate. Note that these loads are roughly four times the rupture loads for the 0.25 inch balls so that the rupture load approximately scales with the area. In addition, the displacements are roughly twice the values for the 0.25 inch balls so that displacement roughly scales with diameter.

In these tests, the non-dissipated kinetic energy which was recovered varied between 22% and 38% of the total stored energy. Thus, the dissipated energy varied between roughly 60% and 80% of the stored energy. Again, this dissipated energy could only be associated with the formation and running of the cracks.

3. Aluminum oxide - Five tests were conducted on alumina (99.9% pure) balls. The loading data are shown in Figure 45. There was approximately a 20% increase in the rupture load and the displacement at rupture for this range of strain rates. The recovered kinetic energy never exceeded 4% of the total stored energy. Thus, the dissipated energy was at least 96% of the stored elastic energy.

4. Tungsten carbide - The tests on tungsten carbide balls also showed a very small nondissipative energy component. The loading curve for one of the tests is shown in Figure 46. The work done on the ball during this test was approximately 112 in-lbf. The total indentation in the crusher blocks was approximately 0.019 inches and, using Figure 33, approximately 80 in-lbf were dissipated in the blocks. Approximately 50% of the ball was captured in the pendulums, and the kinetic energy of these particles was less than 1 in-lbf. Thus, of the 32 in-lbf of work done on the ball, more than 97% was dissipated during fracture.

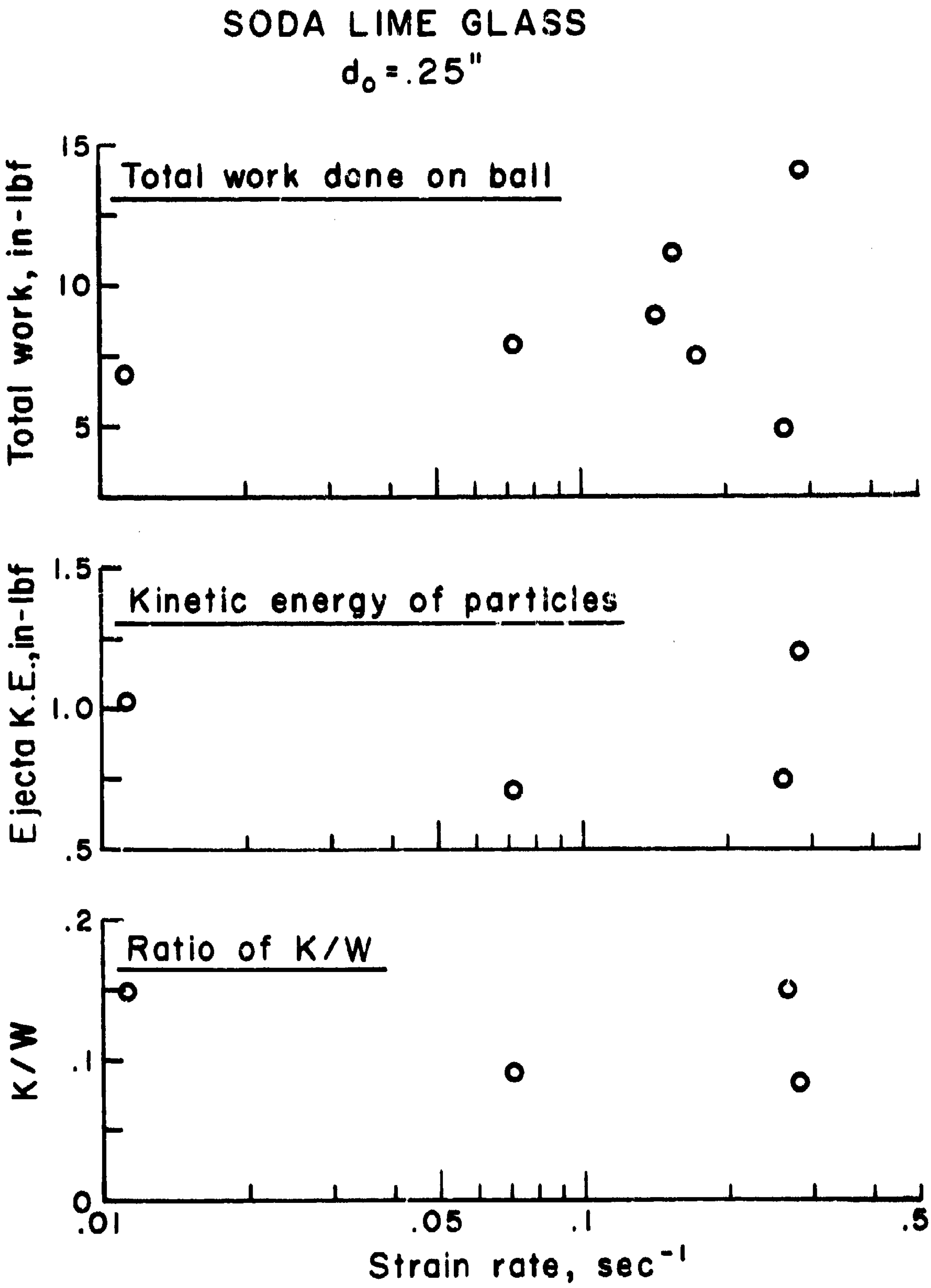
SODA LIME GLASS
d_o = .25"
Total work done on ball
Total work, in-lbf
15
10
5
Kinetic energy of particles
Ejecta K.E., in-lbf
1.5
1.0
.5
Ratio of K/W
K/W
.2
.1
0
.01
.05
.1
.5
Strain rate, sec^{-1}

Figure 43

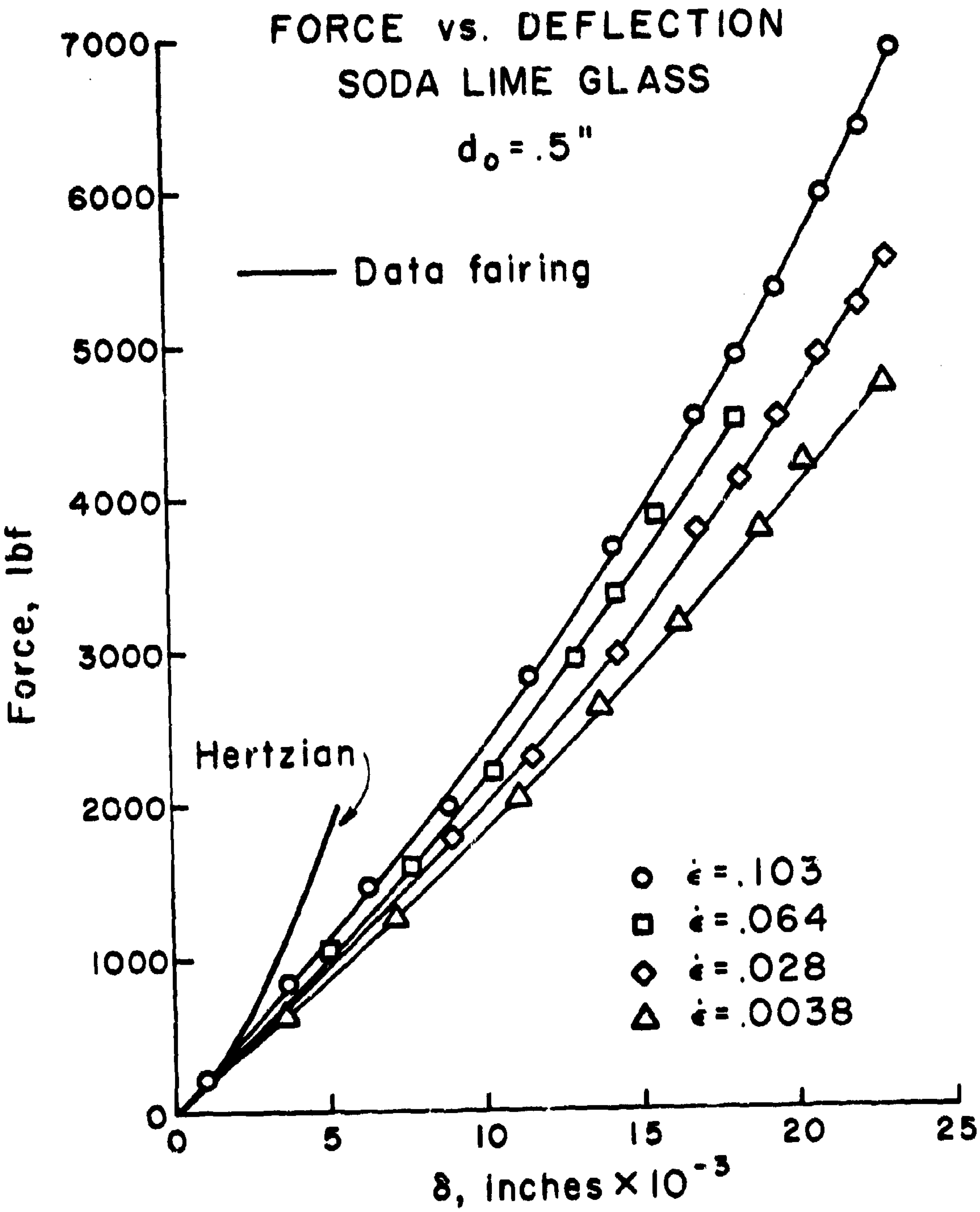
FORCE vs. DEFLECTION
SODA LIME GLASS
$d_o = .5''$
Data fairing
Hertzian
Force, lbf
δ, inches × 10⁻³
7000
6000
5000
4000
3000
2000
1000
0
0
5
10
15
20
25
$\dot{\epsilon} = .103$
$\dot{\epsilon} = .064$
$\dot{\epsilon} = .028$
$\dot{\epsilon} = .0038$

Figure 44

FORCE vs. DEFLECTION
ALUMINUM OXIDE
$d_o = .25''$

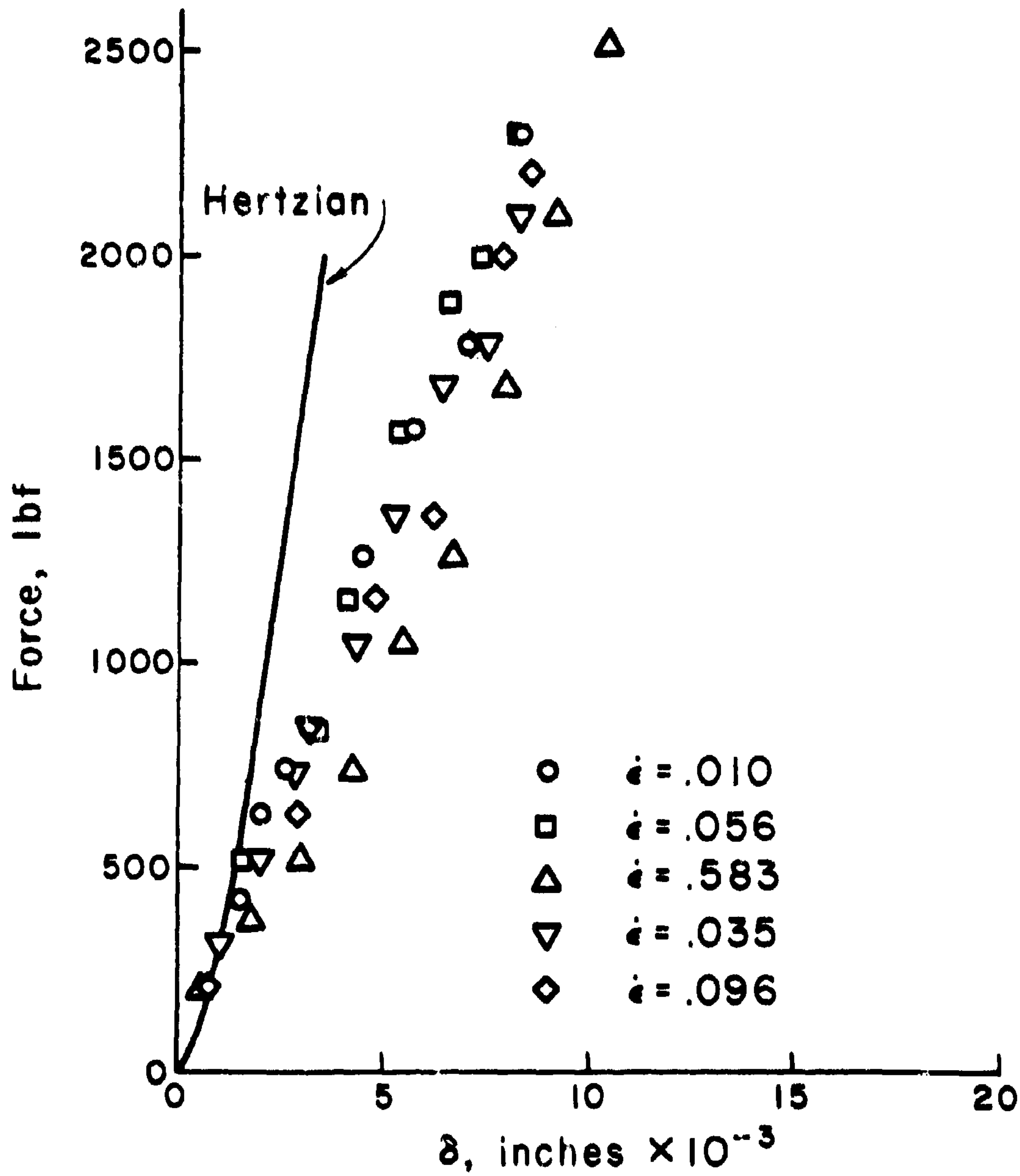

Figure 45

FORCE vs. DEFLECTION
TUNGSTEN CARBIDE

$d_o = .25''$

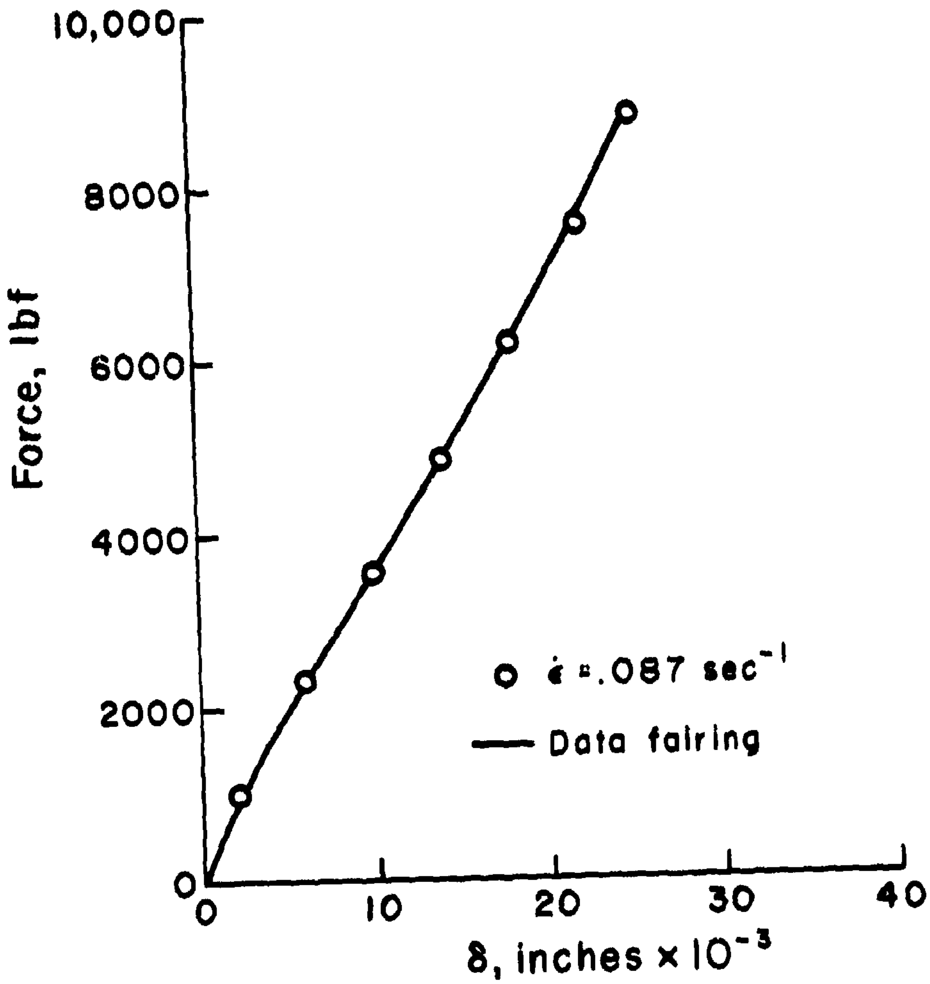

Figure 46

5. Metals - A number of tests were conducted on metal balls. For the soft metals such as 1013 steel, 1100-F aluminum, and 2717-T4 aluminum the ball failure was ductile, i.e., the ball was compressed into a flat disk and did not fracture. Hence, all of the energy was plastically dissipated during deformation.

However, the hard chrome steel balls (AISI 52100) did exhibit brittle fracture. Figure 47 shows the loading data for one of the tests conducted with this material. The rupture load was approximately 13,000 lbf. The total work was approximately 370 in-lbf. Of this total, approximately 1 in-lbf was recovered as nondissipated kinetic energy. Thus, virtually all of the work done on the ball was dissipated.

6. Plastics - Tests were conducted on several plastic balls including polycarbonate (Lexan), acrylic (Lucite), and phenolic. For the polycarbonate, the loading rates were too low to produce brittle fracture; the ball was compressed into a flat disk.

Figure 48 shows the loading data for the phenolic ball. For this test, the total work was approximately 5 in-lbf. The recovered kinetic energy was only 0.13 in-lbf. Thus more than 97% of the energy was dissipated.

Figure 49 shows the loading data for the acrylic ball. The results for this material were similar to those for the phenolic. The total work was approximately 4.3 in-lbf and less than 1% of this energy was recovered as kinetic energy. The remainder was dissipated.

A summary of the results of these tests is given in Table 4. For the range of strain rates tested, the dissipative energy E_{*d} is always much larger than the recoverable kinetic energy. The primary component of the dissipated energy appears to be the energy associated with the formation and running of cracks when the ball fractures. Extrapolation of these results to impact strain rates is difficult, and it is not clear that the partitioning obtained in the laboratory will occur during impact. However, it is clear that an efficient penetrator materia. must be able to dissipate most of the work done on it by the target; the recoverable kinetic energy must be kept to a minimum.

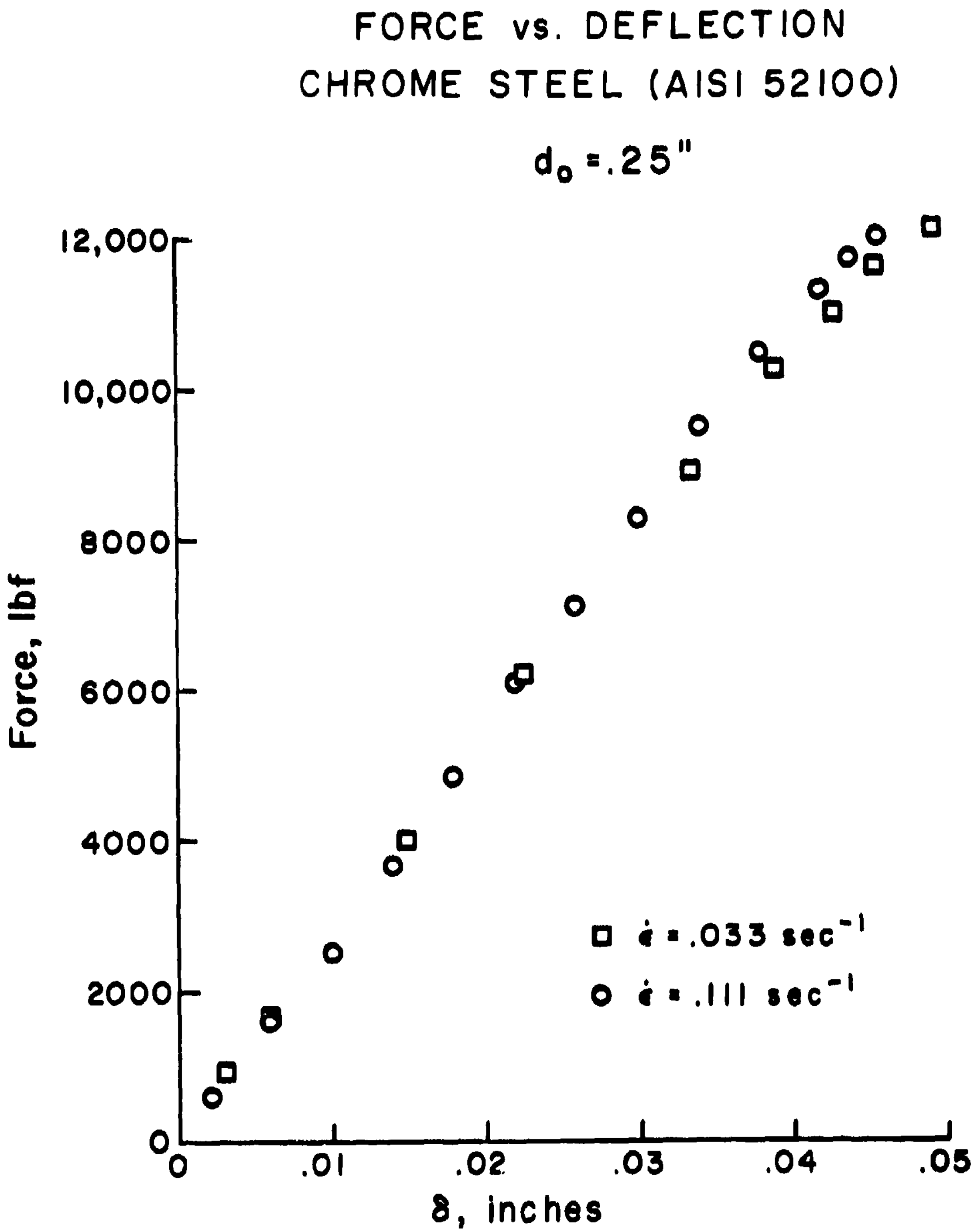
FORCE vs. DEFLECTION
CHROME STEEL (AISI 52100)
d_o = .25"
12,000
10,000
8000
6000
4000
2000
0
Force, lbf
0
.01
.02
.03
.04
.05
δ, inches
$\dot{\epsilon}$ = .033 sec^{-1}
$\dot{\epsilon}$ = .111 sec^{-1}

Figure 47

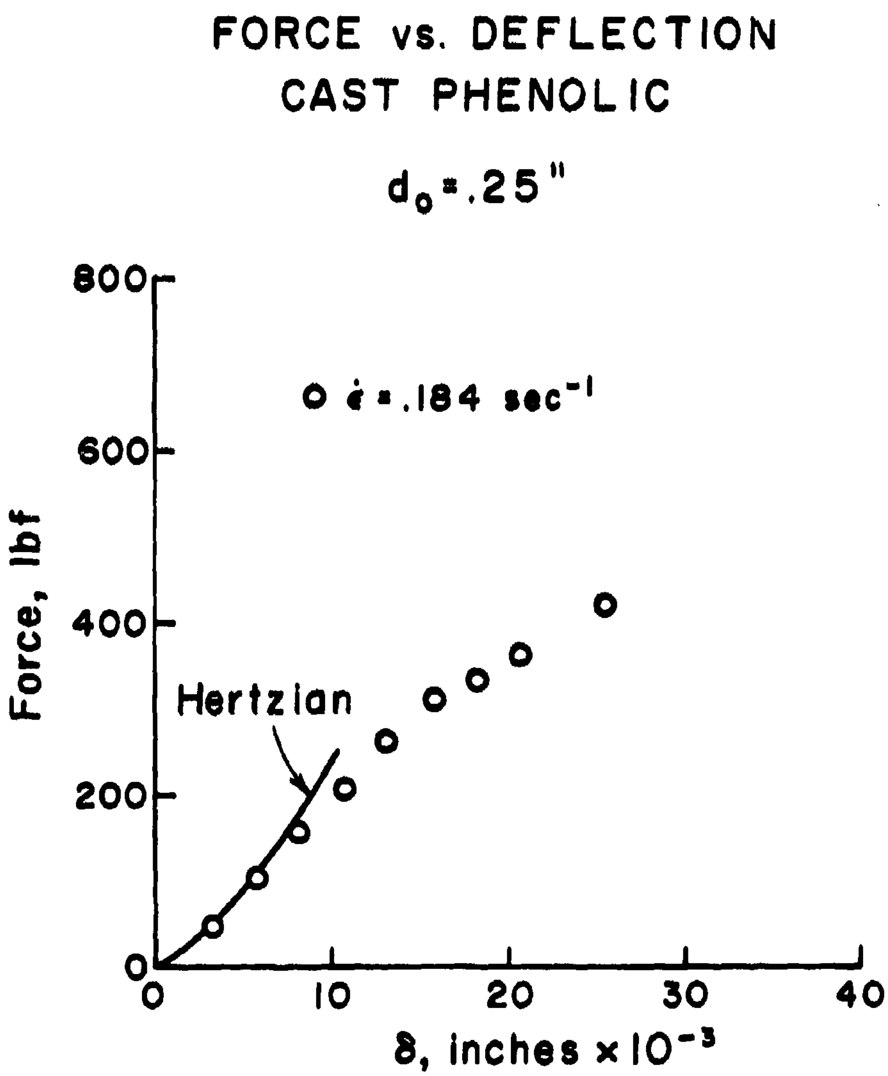
FORCE vs. DEFLECTION
CAST PHENOLIC
d₀=.25"
Force, lbf
800
600
400
200
0
o ė=.184 sec⁻¹
Hertzian
0
10
20
30
40
δ, inches ×10⁻³

Figure 48

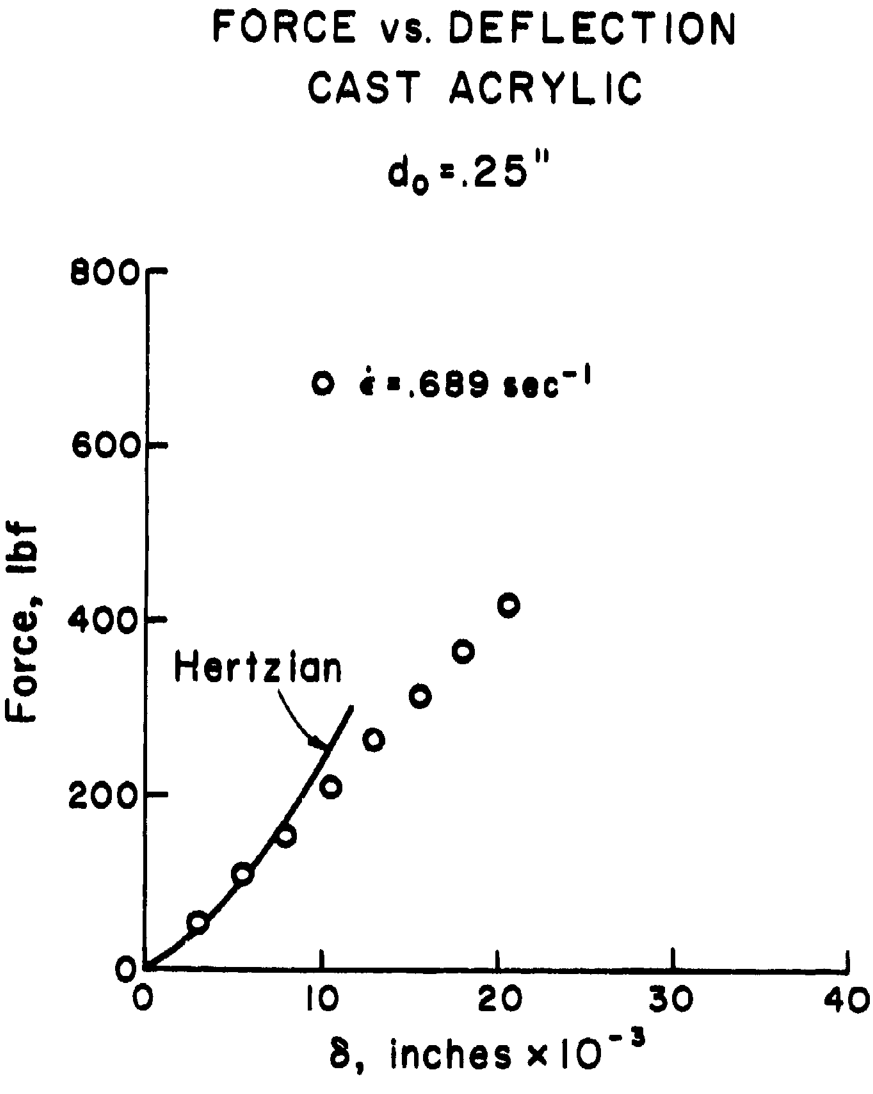
FORCE vs. DEFLECTION
CAST ACRYLIC
d₀ = .25"
o ε̇ = .689 sec⁻¹
Hertzian
Force, lbf
δ, inches × 10⁻³
0
200
400
600
800
0
10
20
30
40

Figure 49

VI. CONCLUSIONS

1. A wide range of target materials has been tested in the A.R.A.P. Impact Facility, and their impact properties have been evaluated using the integral theory of impact. The materials tested include soft and hard metals, ceramics, metal alloys, plastics and composites. The results demonstrate that the impact performance of a target material can be characterized using the two material properties E_{*p} and E_{*e} .

2. A theory has been developed which relates E_{*p} and E_{*e} to more fundamental material properties. The theory yields simple equations which can be used as a preliminary screening tool to suggest candidate materials for particular impact applications.

3. A long rod penetrator model has been developed. The model contains two cells, satisfies global conservation equations, and accounts for material strength using the A.R.A.P. concept of adiabatic hardness ρE_* . The numerical code based on this model predicts penetration depth, ballistic limit velocity, residual mass and residual velocity in good agreement with data for the high velocity impact of homogeneous rods.

4. A fundamental experiment has been performed at laboratory strain rates which demonstrates that most of the strain energy stored in a penetrator during compression is dissipated when the penetrator fractures. The primary dissipation mechanism appears to be associated with the formation and running of cracks.

VII. REFERENCES

1. Donaldson, Coleman duP., Contiliano, Ross M., and McDonough, Thomas B.: The Qualification of Target Materials Using the Integral Theory of Impact. A.R.A.P. Rept. No. 295, Aeronautical Research Associates of Princeton, Inc., December 1976.

2. Swanson, Claude V. and Donaldson, Coleman duP.: Application of the Integral Impact Theory to Modeling Long-Rod Penetrators. A.R.A.P. Rept. No. 333, Aeronautical Research Associates of Princeton, Inc., March 1978.

3. Donaldson, Coleman duP., McDonough, Thomas B., and Contiliano, Ross M.: Application of the Integral Impact Theory to the Design of Specialized Tactical Ordnance. A.R.A.P. Rept. No. 279, Aeronautical Research Associates of Princeton, Inc., May 1976.

4. Donaldson, Coleman duP., Contiliano, Ross M., and McDonough Thomas B.: A Study of Water Drop Displacement and Deformation in Aerodynamic Shock Layers. A.R.A.P. Rept. No. 265, Aeronautical Research Associates of Princeton, Inc., March 1978.

5. McClintock, F. A. and Argon, A. S., *Mechanical Behavior of Materials*, Chapter 13, Addison-Wesley, Reading, Mass., 1966.

6. Lambert, John P.: The Terminal Ballistics of Certain 65 Gram Long Rod Penetrators Impacting Steel Armor Plate. Rept. No. ARBRL-TR02072, May 1978.

7. Bergstrom, B. H. and Sollenberger, C. L.: Kinetic Energy Effect in Single Particle Crushing; Presented at the AIME Meeting, St. Louis, February 1961.

8. IBM large computer scientific subroutine package.

APPENDIX A

MATERIAL QUALIFICATION TEST DATA

This appendix contains a summary of the data obtained during the material qualification tests. For each material, the following items are tabulated:

(1) Test number

(2) Target identification number

(3) Target thickness, inches

(4) Projectile material, WC = tungsten carbide
ST = chrome steel
STB = soft steel

(5) Projectile mass, grams

(6) Projectile diameter, inches

(7) Projectile velocity, feet/second

(8) Crater depth, inches

(9) Note for test anomalies

A = Projectile remained embedded in target

B = Projectile broken

C = Target backface cracked

D = Penetration greater than half the target thickness

E = Target backed with rubber.

Note that the data are tabulated in both metric and English standard units. The conversion factors between the systems are

$$1 \text{ gram} = 2.205 \times 10^{-3} \text{ lbm}$$

$$1 \text{ meter} = 3.281 \text{ feet}$$

TARGET MATERIAL	TEST NUMBER	TARGET*		PROJECTILE				CRATER DEPTH (in)	NOTE
		NUMBER	THICKNESS (in)	MATERIAL	MASS (gm)	DIAMETER (in)	VELOCITY (ft/sec)		
ACRYLIC (American Cyanimide Acrylite)	61	12-1	.92	ST	.250	.156	291	0	
	62	12-2	.92	ST	.25	.156	454	0	
	63	12-3	.92	ST	.25	.156	578	0	
	64	12-4	.92	ST	.25	.156	162	0	
	68	12-5	.93	WC	2.01	.25	1043	.14	
	120	12-6	.95	WC	2.01	.25	1397	.563	C,D
	102	12-7	.93	WC	.485	.156	452	0	
	133	12-8	.92	ST	.345	.174	743	0	
	178	12-10	.96	WC	2.01	.25	635	.013	
	119	12-11	.92	WC	2.01	.25	949	.041	
	121	12-2b	1.02	WC	2.01	.25	691	.006	
	179	12-13	.96	WC	2.01	.25	868	.063	
	180	12-12	.95	WC	2.01	.25	742	.004	
	182	12-4b	1.02	WC	2.01	.25	1377	.194	C
		*All targets were circular disks (d ≅ 6-1/4").							
ALUMINUM (1100-F Plate)	6	7-2	1.07	WC	2.01	.25	1701	.512	A,D
	7	7-3	1.06	WC	2.01	.25	1219	.331	
	8	7-4	1.07	WC	2.01	.25	903	.214	
	10	7-5	1.07	WC	2.01	.25	1613	.472	A
	39	7-6	1.07	ST	.25	.156	365	.028	
	43	7-7	1.07	ST	.25	.156	160	.012	
	44	7-8	1.02	ST	.25	.156	593	.051	
	83	7-9	1.07	WC	.485	.156	454	.053	
	84	7-10	1.07	WC	.485	.156	198	.023	
	43a	7-7	1.07	ST	8.23	.50	28	.007	
	43b	7-7	1.07	WC	2.01	.25	28	.004	
		*All targets were circular disks (d ≅ 6-1/8").							

TARGET MATERIAL	TEST NUMBER	TARGET* NUMBER	TARGET* THICKNESS (in)	PROJECTILE MATERIAL	PROJECTILE MASS (gm)	PROJECTILE DIAMETER (in)	PROJECTILE VELOCITY (ft/sec)	CRATER DEPTH (in)	NOTE
ALUMINUM (5083, Rockwell B-75)	123	13-1	1.02	WC	2.01	.25	838	.087	
	124	13-2	1.02	WC	2.01	.25	1446	.181	
	125	13-3	1.02	WC	2.01	.25	1806	.251	A
	129	13-4	1.02	WC	.485	.156	196	.010	
	130	13-5	1.02	WC	.485	.156	457	.026	
	134	13-6	1.02	WC	2.01	.25	1115	.127	
	135	13-7	1.02	WC	2.01	.25	2326	.330	A
		*All targets were rectangles (3.9" x 4.5").							
CADMIUM (99.9% Pure, Open Cast)	41	3-1	1.11	ST	.25	.156	365	.024	
	55	3-2	1.02	ST	.25	.156	597	.041	
	56	3-3	0.98	ST	.25	.155	159	.012	
	69	3-4	1.02	WC	2.01	.25	1048	.257	A
	71	3-5	1.12	WC	2.01	.25	1086	.234	
	75	3-6	1.06	WC	2.01	.25	699	.127	
	80	3-7	1.06	WC	2.01	.25	1491	.368	A
	95	3-8	1.10	WC	.485	.156	200	.020	
	96	3-9	1.06	WC	.485	.156	455	.044	
	110	3-10	1.09	WC	2.01	.25	888	.176	
	56a	3-3	0.98	ST	8.23	.50	28	.006	
	56b	3-3	0.98	WC	2.01	.25	28	.003	
		*All targets were circular disks (d ≃ 6").							

TARGET MATERIAL	TEST NUMBER	TARGET*		PROJECTILE				CRATER DEPTH (in)	NOTE
		NUMBER	THICKNESS (in)	MATERIAL	MASS (gm)	DIAMETER (in)	VELOCITY (ft/sec)		
COPPER (Hot Rolled, ETP Plate)	25	2-1	1.02	WC	2.01	.25	648	.104	
	26	2-2	1.02	WC	2.01	.25	1080	.172	
	27	2-3	1.02	WC	2.01	.25	1823	.367	
	28	2-4	1.00	WC	2.01	.25	2483	.575	A,D
	29	2-5	1.03	WC	2.01	.25	1557	.301	
	38	2-6	1.03	ST	.25	.156	352	.021	
	47	2-7	1.02	ST	.25	.156	161	.009	
	48	2-8	1.03	ST	.25	.156	525	.031	
	93	2-9	1.03	WC	.485	.156	204	.021	
	94	2-10	1.03	WC	.485	.156	455	.045	
	47a	2-7	1.02	ST	8.23	.50	28	.005	
	47b	2-7	1.02	WC	2.01	.25	28	.004	
		*All targets were circular disks (d $\tilde{=}$ 6-1/8").							
GLASS (Corning Pyrex 7740)	40	9-3	.95	STB	.25	.156	367	.033	
	53	9-4	.95	STB	.25	.156	500	.022	
	54	9-5	.95	STB	.25	.156	292	.036	
	70	9-6	.96	WC	2.01	.25	1087	.125	C
	74	9-7	.91	WC	2.01	.25	754	.110	E
	100	9-8	.90	WC	.485	.156	198	.019	E
	101	9-9	.89	WC	.485	.156	446	.055	
	177	9-10	.92	ST	.25	.156	526	.045	
		*All targets were circular disks (d $\tilde{=}$ 5-15/16")							

TARGET MATERIAL	TEST NUMBER	TARGET* NUMBER	TARGET* THICKNESS (in)	PROJECTILE MATERIAL	PROJECTILE MASS (gm)	PROJECTILE DIAMETER (in)	PROJECTILE VELOCITY (ft/sec)	CRATER DEPTH (in)	NOTE
IRON (Class 40 - Gray Cast)	15	5-1	1.03	WC	2.01	.25	1757	.184	
	16	5-2	1.05	WC	2.01	.25	2892	.405	A,B
	17	5-3	1.03	WC	2.01	.25	1115	.090	
	18	5-4	1.05	WC	2.01	.25	747	.062	
	19	5-5	1.05	WC	2.01	.25	2257	.224	A
	88	5-6	1.04	ST	.25	.156	167	.005	
	89	5-7	1.03	ST	.25	.156	374	.011	
	90	5-8	1.05	ST	.25	.156	606	.022	
	91	5-9	1.06	WC	.485	.156	204	.011	
	106	5-10	1.05	WC	2.01	.25	759	.066	
	122	5-11	1.04	WC	2.01	.25	1287	.126	
	18a	5-4	1.05	ST	8.23	.50	28	.003	
	18b	5-4	1.05	WC	2.01	.25	28	.0015	
		*All targets were circular disks (d ≈ 6-1/4").							
KEVLAR (Rigid, Epoxy Resin)	138	15-1	1.1	WC	2.01	.25	1235	.360	A
	143	15-2	1.08	WC	2.01	.25	1291	.408	A
	144	15-3	1.07	WC	2.01	.25	1100	.305	A
	146	15-4	1.10	WC	.485	.156	446	.030	
	145	15-5	1.09	WC	2.01	.25	2059	.804	A,D
	147	15-6	1.07	WC	2.01	.25	1164	.338	A
	148	15-7	1.08	WC	2.01	.25	1034	.294	A
	149	15-8	1.09	WC	.485	.156	198	.004	
	150	15-9	1.08	WC	.485	.156	301	.007	
	151	15-10	1.08	WC	2.01	.25	612	.115	
	157	15-11	1.08	WC	2.01	.25	871	.198	A
	158	15-12	1.08	WC	.485	.156	369	.010	
		*All targets were squares (4.0" × 4.0"). Targets consisted of 3 layers-stacked and unbonded.							

TARGET MATERIAL	TEST NUMBER	TARGET* NUMBER	TARGET* THICKNESS (in)	PROJECTILE MATERIAL	PROJECTILE MASS (gm)	PROJECTILE DIAMETER (in)	VELOCITY (ft/sec)	CRATER DEPTH (in)	NOTE
LEAD (99.9% Pure, Open Cast)	11	1-1	1.05	WC	2.01	.25	1007	.703	A,D
	12	1-2	1.05	WC	2.01	.25	637	.364	A
	13	1-3	1.07	WC	2.01	.25	916	.606	A,D
	14	1-4	1.06	WC	2.01	.25	729	.443	A
	36	1-5	1.07	ST	.25	.156	353	.063	
	49	1-6	1.07	ST	.25	.156	151	.026	
	50	1-7	1.06	ST	.25	.156	492	.094	
	97	1-8	1.06	WC	.485	.156	201	.045	
	98	1-9	1.07	WC	.485	.156	451	.131	
	99	1-10	1.07	ST	.25	.156	416	.076	
	49a	1-6	1.07	ST	8.23	.50	28	.017	
	49b	1-6	1.07	WC	2.01	.25	28	.012	
	111	1-11	2.17	WC	2.01	.25	1003	.680	A
	112	1-12	2.26	WC	2.01	.25	909	.608	A
	113	1-13	2.14	WC	2.01	.25	765	.493	
	114	1-14	2.33	WC	2.01	.25	1174	.848	A
	155	1-15	2.14	WC	2.01	.25	622	.360	
	156	1-16	2.14	WC	2.01	.25	1042	.722	A
		*All targets were circular disks (d ≅ 6").							
POLYCARBONATE (G.E. Lexan)	57	11-1	1.01	ST	.25	.156	295	.004	
	58	11-2	1.02	ST	.25	.156	457	.010	
	59	11-3	1.02	ST	.25	.156	584	.014	
	60	11-4	1.01	ST	.25	.156	162	.001	
	67	11-5	1.02	WC	2.01	.25	1111	.327	A
	73	11-7	1.03	WC	2.01	.25	1293	.485	A
	92	11-8	1.01	WC	.485	.156	312	.009	
	108	11-9	1.02	WC	2.01	.25	1019	.255	A
	109	11-10	1.02	WC	2.01	.25	728	.061	
		*All targets were circular disks (d ≅ 6").							

TARGET MATERIAL	TEST NUMBER	TARGET* NUMBER	TARGET* THICKNESS (in)	PROJECTILE MATERIAL	PROJECTILE MASS (gm)	PROJECTILE DIAMETER (in)	PROJECTILE VELOCITY (ft/sec)	CRATER DEPTH (in)	NOTE
SALT (Polycrystalline Sodium Chloride)	30	10-1	1.05	ST	.35	.174	468	.046	
	31	10-2	1.05	ST	.35	.174	456	.067	
	32	10-3	1.04	ST	.35	.174	283	.030	
	33	10-4	1.01	ST	.35	.174	717	.078	
	42	10-5	1.0	ST	.25	.156	371	.029	
	51	10-6	.98	ST	.25	.156	161	.015	
	51a	10-6	.98	ST	8.23	.5	28	.012	
	51b	10-6	.98	WC	2.01	.25	28	.007	
	52	10-7	1.04	ST	.25	.156	593	.042	
	103	10-8	1.10	WC	.485	.156	201	.025	
	104	10-9	1.08	WC	.485	.156	345	.048	
	105	10-10	1.10	WC	.485	.156	453	.073	
	107	10-11	1.11	WC	2.01	.25	1282	.431	
	116	10-12	1.05	WC	2.01	.25	795	.235	
	117	10-13	1.05	WC	2.01	.25	1098	.330	
	118	10-14	1.10	WC	2.01	.25	942	.310	
		*All targets were circular disks (d ≈ 6-5/16").							
SILICON (Porous, .5% Fe)	76	8-1	3.25	WC	2.01	.25	1013	.174	
	77	8-2	2.84	WC	2.01	.25	1283	.255	
	78	8-3	3.5	WC	2.01	.25	916	.175	
	79	8-4	4.12	WC	2.01	.25	1381	.25	
		*Targets were large chunks of irregular shape and cast in concrete.							

TARGET MATERIAL	TEST NUMBER	TARGET* NUMBER	TARGET* THICKNESS (in)	PROJECTILE MATERIAL	PROJECTILE MASS (gm)	PROJECTILE DIAMETER (in)	PROJECTILE VELOCITY (ft/sec)	CRATER DEPTH (in)	NOTE
STEEL (1020 - Hot Rolled Plate)	1	4-1	1.01	WC	2.01	.25	2266	.219	B
	2	4-2	1.0	WC	2.01	.25	3386	.332	B
	3	4-3	1.01	WC	2.01	.25	1294	.103	
	4	4-4	1.01	WC	2.01	.25	4336	.399	B
	9	4-5	1.01	WC	2.01	.25	805	.058	
	65	4-6	1.0	ST	.345	.173	731	.024	
	66	4-7	1.0	ST	.345	.173	294	.010	
	85	4-8	1.01	ST	.250	.156	163	.005	
	86	4-9	1.01	WC	.485	.156	201	.008	
	87	4-10	1.01	WC	.485	.156	451	.016	
	66a	4-7	1.0	ST	8.23	.50	28	0	
	66b	4-7	1.0	WC	2.01	.25	28	0	
		*All targets were circular disks (d ≅ 6-1/8").							
STEEL (Rolled Homogeneous Armor)	127	14-1	1.0	WC	2.01	.25	751	.041	
	126	14-2	1.0	WC	2.01	.25	1319	.082	
	128	14-3	1.0	WC	2.01	.25	2082	.146	B
	131	14-4	1.0	WC	.485	.156	193	.007	
	132	14-5	1.0	WC	.485	.156	457	.015	
	136	14-6	1.0	WC	2.01	.25	606	.033	
	137	14-7	1.01	WC	2.01	.25	1623	.108	B
		*All targets were rectangles (4.5" x 3.9").							

TARGET MATERIAL	TEST NUMBER	TARGET* NUMBER	TARGET* THICKNESS (in)	PROJECTILE MATERIAL	PROJECTILE MASS (gm)	PROJECTILE DIAMETER (in)	PROJECTILE VELOCITY (ft/sec)	CRATER DEPTH (in)	NOTE
TITANIUM (Ti-6Al-4V)	216	19-1	.68	WC	2.01	.25	1047	.076	
	217	19-2	.68	WC	2.01	.25	1947	.16	
	218	19-3	.68	WC	2.01	.25	3015	.294	B
	225	19-4	.68	WC	2.01	.25	2677	.250	B
	226	19-5	.68	WC	2.01	.25	1520	.115	
	227	19-6	.68	WC	2.01	.25	794	.050	
	228	19-7	.68	WC	.485	.156	307	.012	
	229	19-8	.68	ST	.250	.156	432	.010	
	228b	19-7	.68	WC	.485	.156	259	.010	
	228c	19-7	.68	WC	.485	.156	287	.011	
	228d	19-7	.68	WC	.485	.156	472	.013	
	229b	19-8	.68	ST	.25	.156	403	.009	
	229c	19-8	.68	ST	.25	.156	406	.009	
	229d	19-8	.68	ST	.25	.156	616	.011	
		*All targets were square (4-3/8" x 4-3/8").							
ZINC (99.9% Pure, Open Cast)	20	6-1	1.04	WC	2.01	.25	1381	.211	
	21	6-2	1.07	WC	2.01	.25	756	.103	
	22	6-3	1.08	WC	2.01	.25	2078	.385	A
	23	6-4	.99	WC	2.01	.25	1011	.148	
	24	6-5	.97	WC	2.01	.25	2680	.615	A,D
	37	6-6	1.03	ST	.25	.156	353	.020	
	45	6-7	1.01	ST	.25	.156	164	.009	
	46	6-8	1.08	ST	.25	.156	552	.029	
	81	6-9	1.03	WC	.485	.156	459	.036	
	82	6-10	1.09	WC	.485	.156	197	.015	
	45a	6-7	1.01	ST	8.23	.5	28	.0065	
	45b	6-7	1.01	WC	2.01	.25	28	.004	
		*All targets were circular disks (d ≅ 5-7/8").							

APPENDIX B

E_* EVALUATION

The results of the E_* evaluations for each of the target materials which were qualified are shown in Figures B-1 to B-14. The procedure by which these values were obtained was described in Chapter II. Briefly, these values of E_* when used in the integral theory result in a computed penetration which matches the measured penetration for a given impact velocity. The data are plotted versus nondimensional penetration depth because of the functional dependence of E_{*e} on p/d_o which was noted in Chapters II and III.

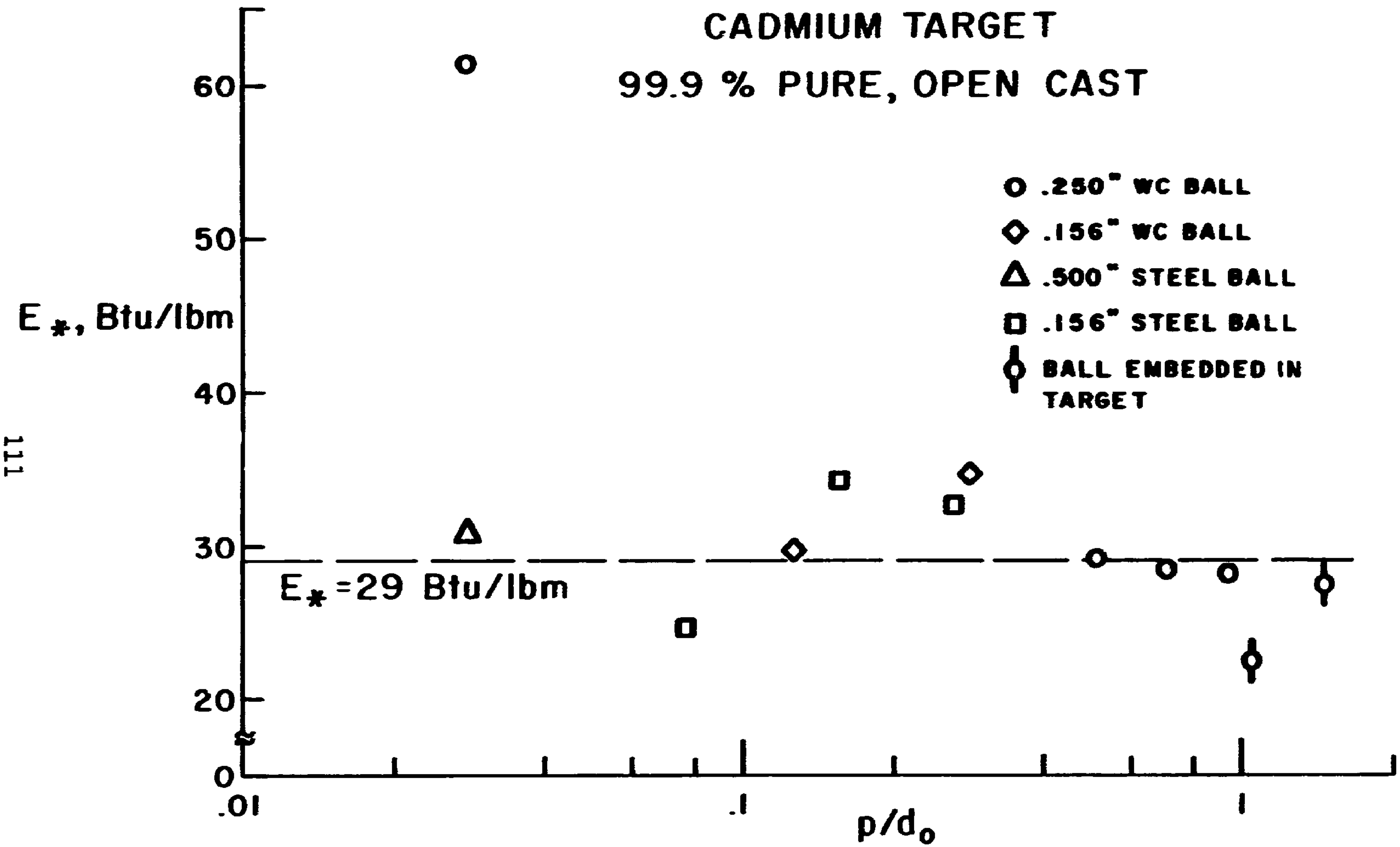
CADMIUM TARGET
99.9 % PURE, OPEN CAST
.250" WC BALL
.156" WC BALL
.500" STEEL BALL
.156" STEEL BALL
BALL EMBEDDED IN TARGET
E*, Btu/lbm
60
50
40
30
20
0
E* =29 Btu/lbm
.01
.1
1
p/do

Figure B-1

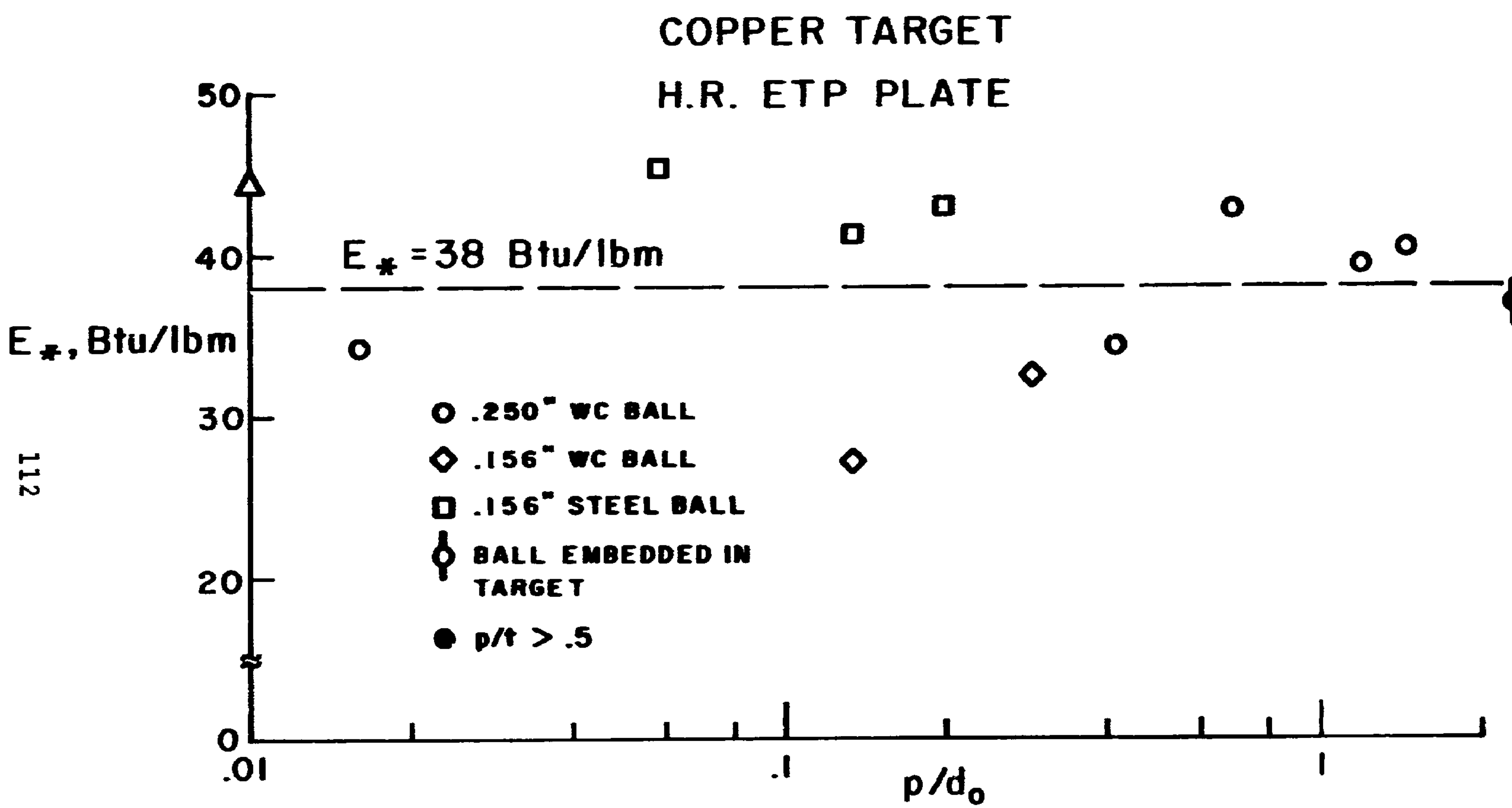
COPPER TARGET
H.R. ETP PLATE
E* = 38 Btu/lbm
E*, Btu/lbm
50
40
30
20
0
.01
.1
1
p/d₀
.250" WC BALL
.156" WC BALL
.156" STEEL BALL
BALL EMBEDDED IN TARGET
p/t > .5

Figure B-2

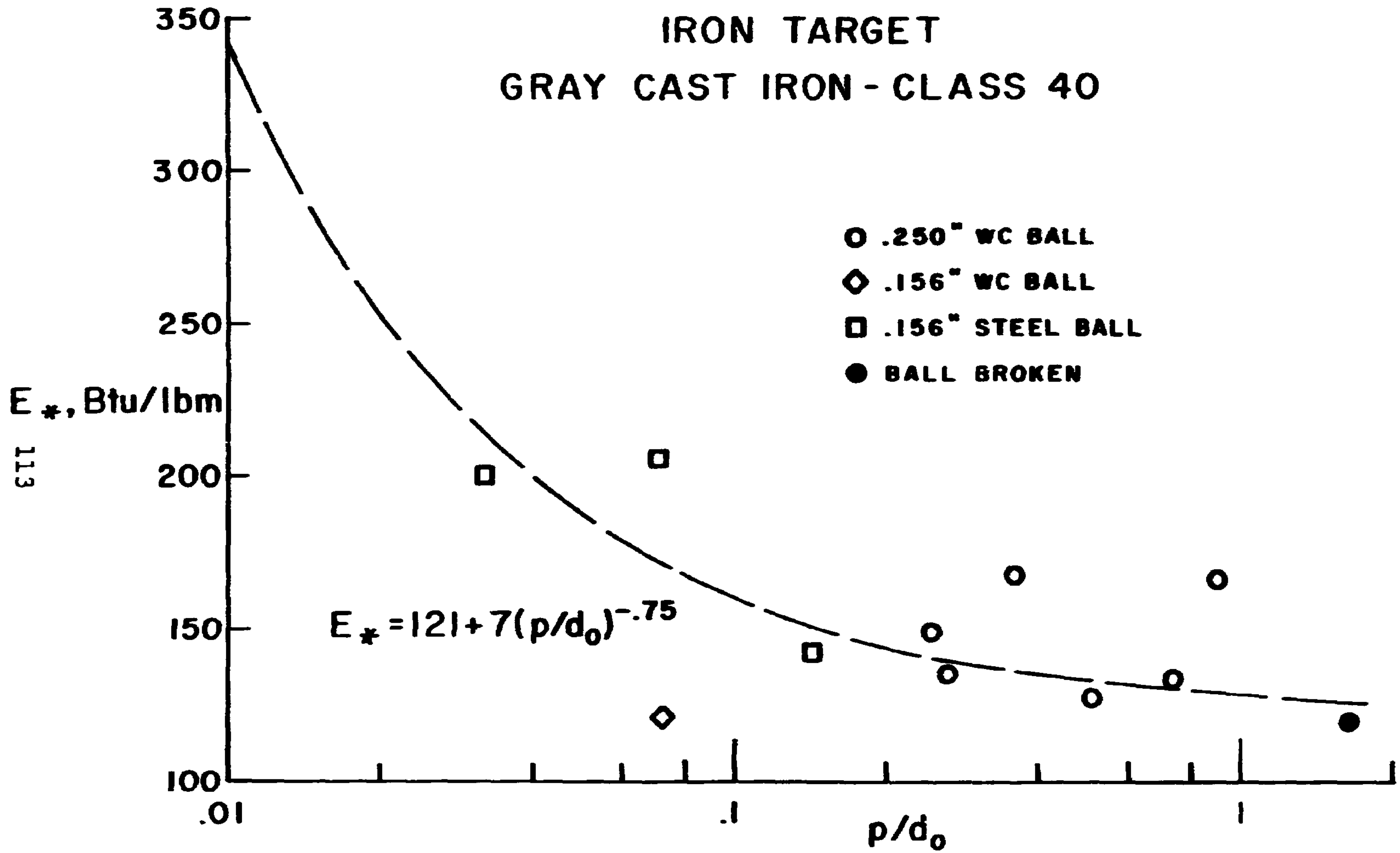
IRON TARGET
GRAY CAST IRON - CLASS 40
O .250" WC BALL
◇ .156" WC BALL
□ .156" STEEL BALL
● BALL BROKEN
E_*, Btu/lbm
350
300
250
200
150
100
.01
.1
1
p/d_o
$E_* = 121 + 7(p/d_o)^{-.75}$

Figure B-3

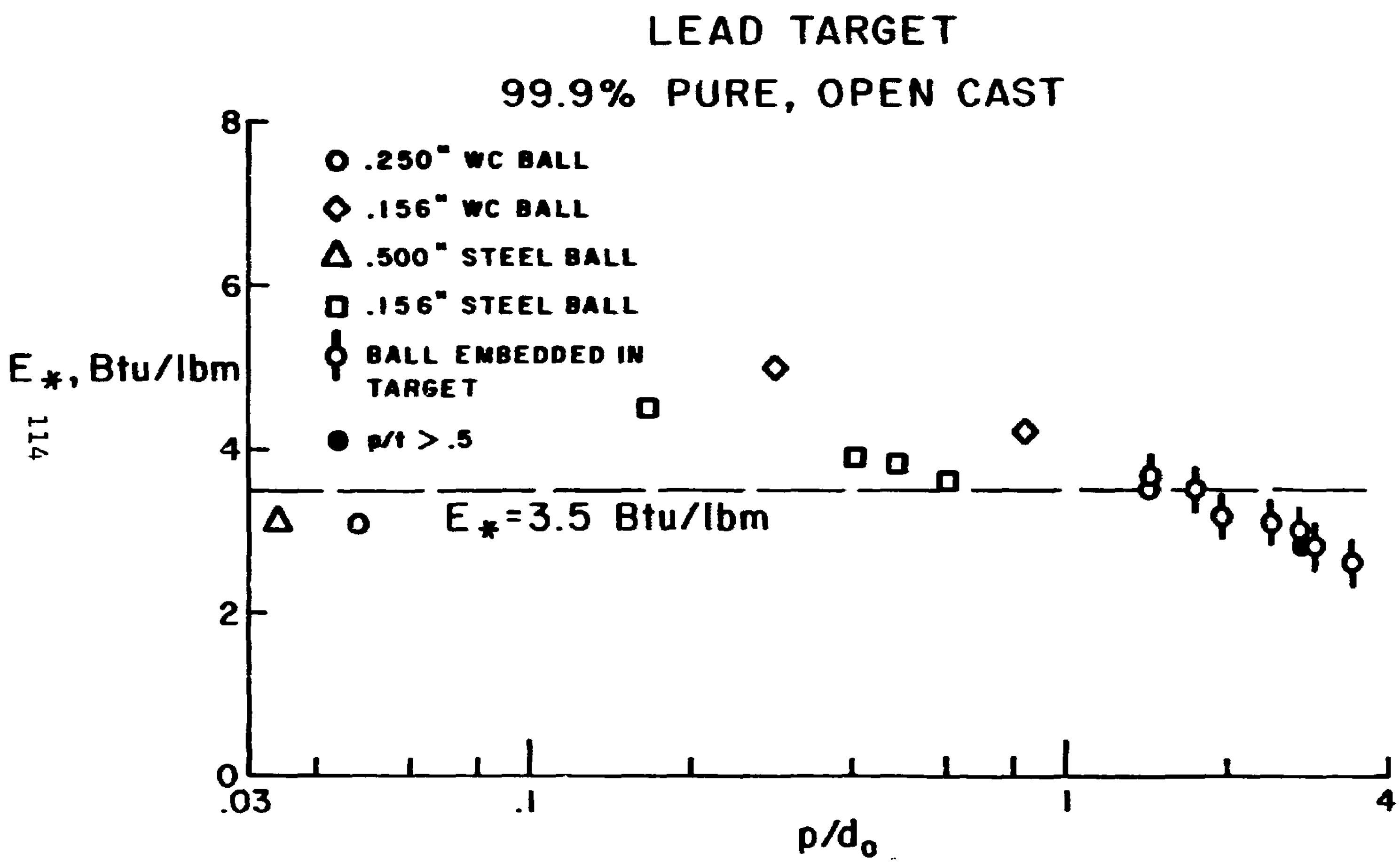
LEAD TARGET
99.9% PURE, OPEN CAST
.250" WC BALL
.156" WC BALL
.500" STEEL BALL
.156" STEEL BALL
BALL EMBEDDED IN TARGET
p/t > .5
E*=3.5 Btu/lbm
E*, Btu/lbm
0
2
4
6
8
.03
.1
1
4
p/d0

Figure B-4

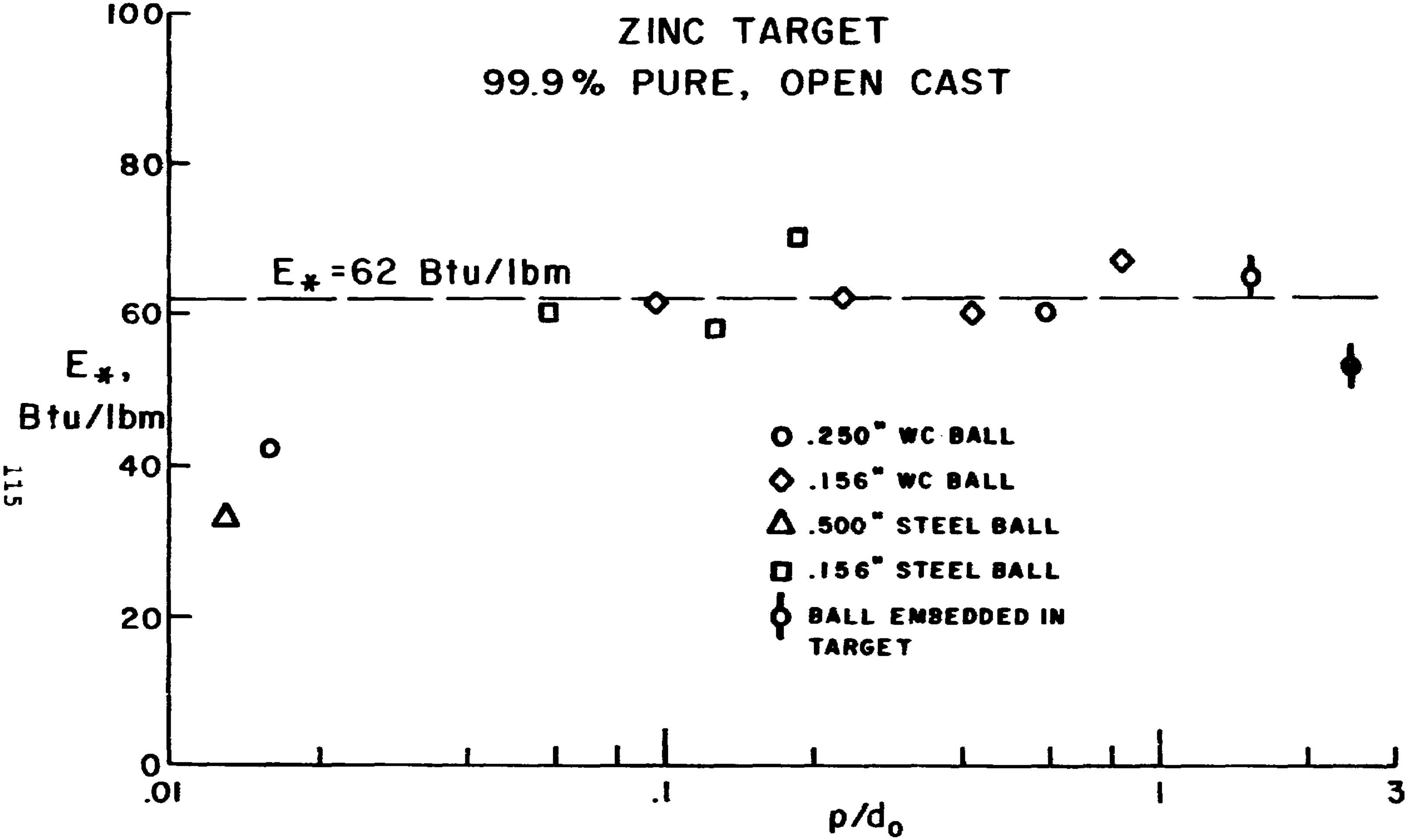
ZINC TARGET
99.9% PURE, OPEN CAST
E* =62 Btu/lbm
E*,
Btu/lbm
100
80
60
40
20
0
.01
.1
1
3
p/do
.250" WC BALL
.156" WC BALL
.500" STEEL BALL
.156" STEEL BALL
BALL EMBEDDED IN
TARGET

Figure B-5

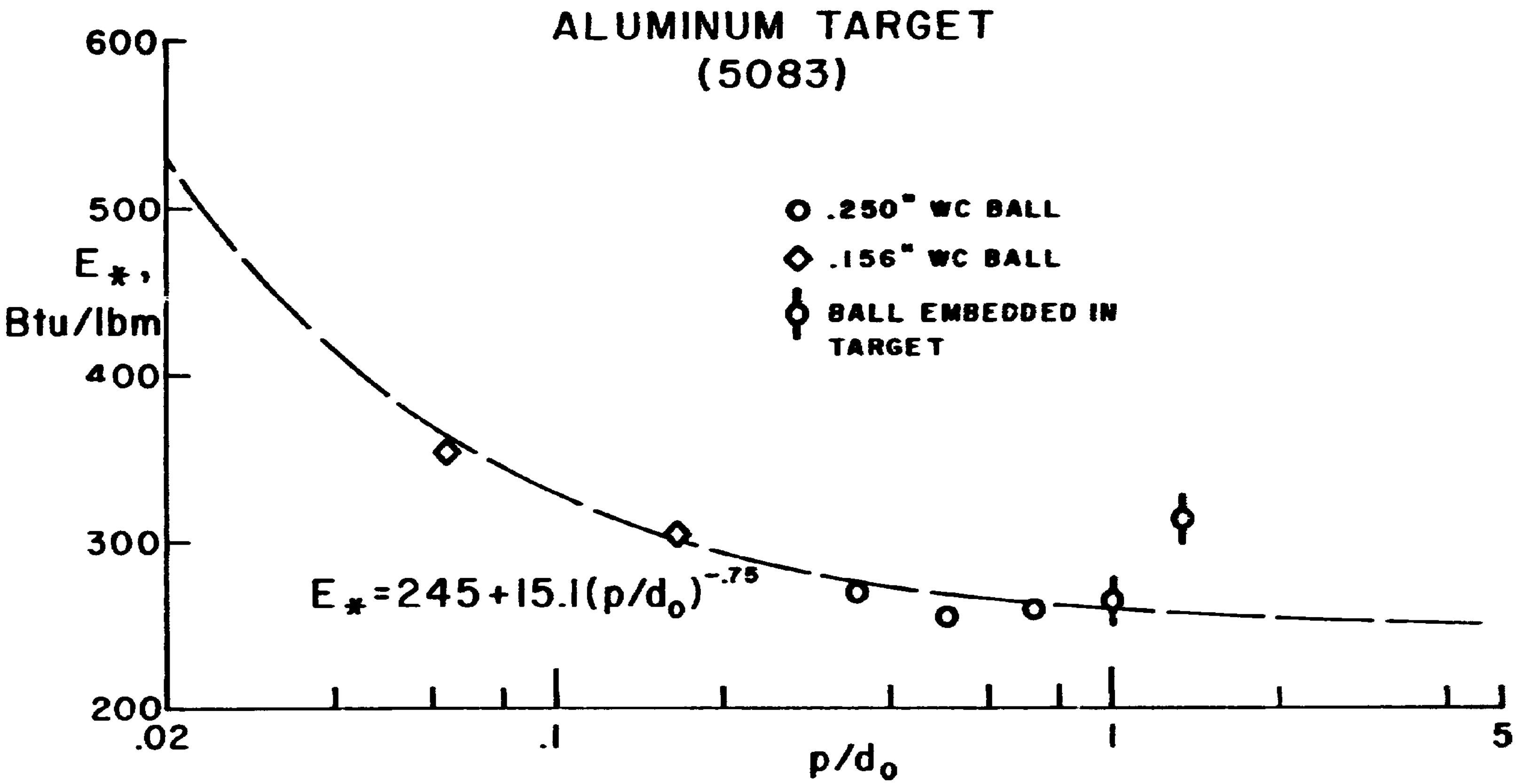

ALUMINUM TARGET
(5083)
600
500
400
300
200
E*,
Btu/lbm
.250" WC BALL
.156" WC BALL
BALL EMBEDDED IN TARGET
$E_* = 245 + 15.1(p/d_o)^{-.75}$
.02
.1
1
5
p/d_o

Figure B-6

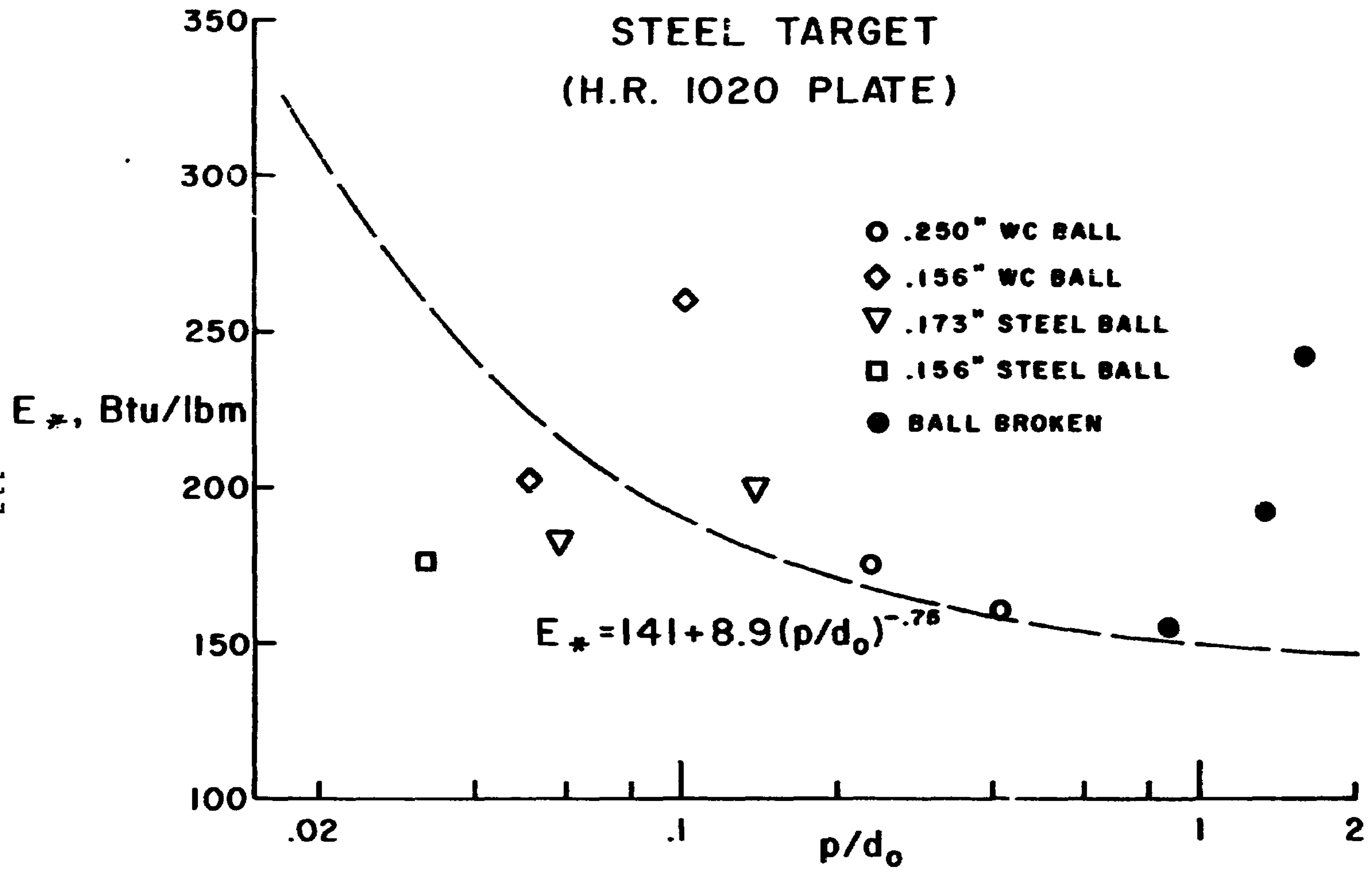
STEEL TARGET
(H.R. 1020 PLATE)
○ .250" WC BALL
◇ .156" WC BALL
▽ .173" STEEL BALL
□ .156" STEEL BALL
● BALL BROKEN
E*=141+8.9(p/d_o)^-.76
E*, Btu/lbm
350
300
250
200
150
100
.02
.1
1
2
p/d_o

Figure B-7

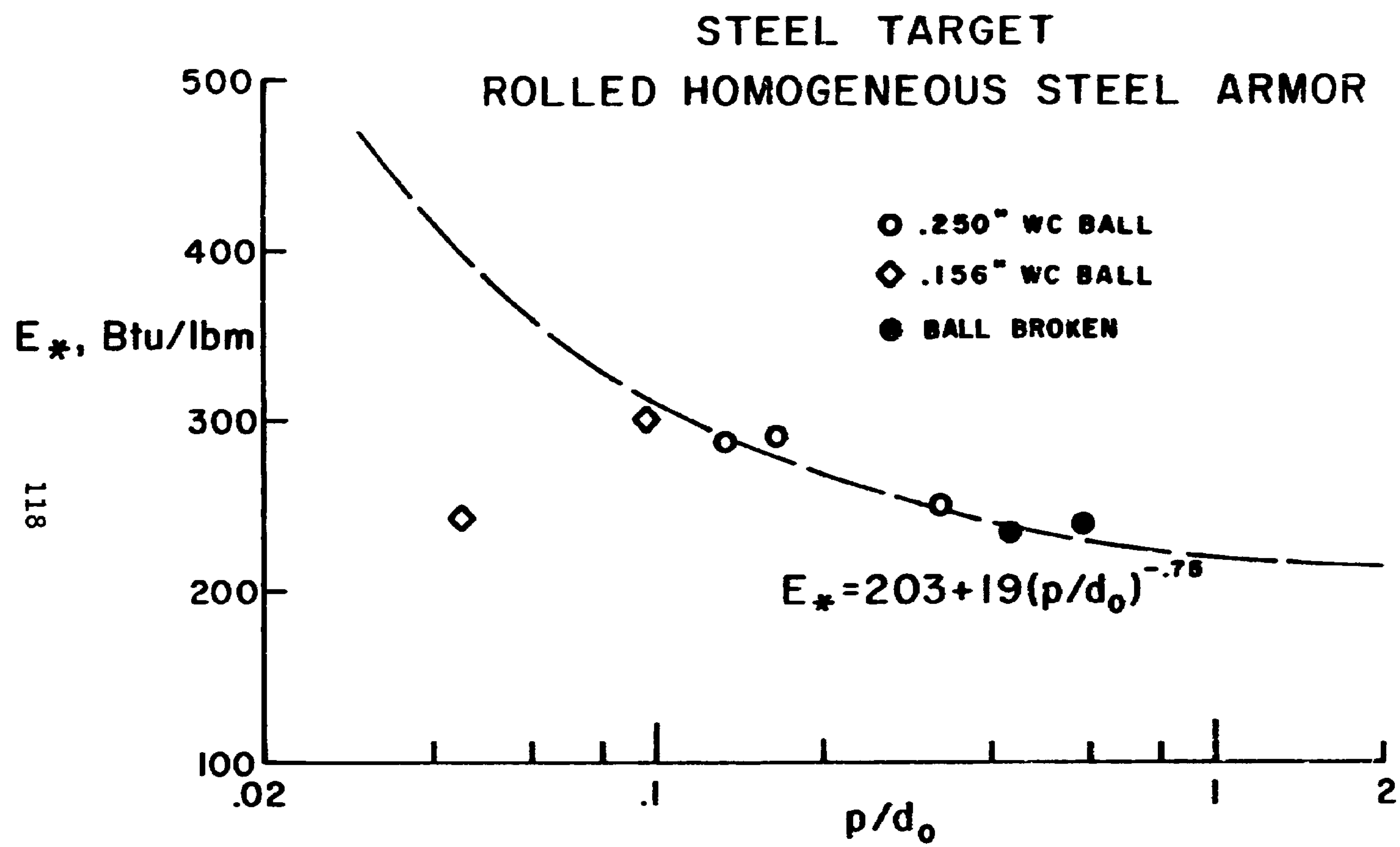
STEEL TARGET
ROLLED HOMOGENEOUS STEEL ARMOR
.250" WC BALL
.156" WC BALL
BALL BROKEN
E*, Btu/lbm
500
400
300
200
100
.02
.1
1
2
p/do
E*=203+19(p/do)^-.75

Figure B-8

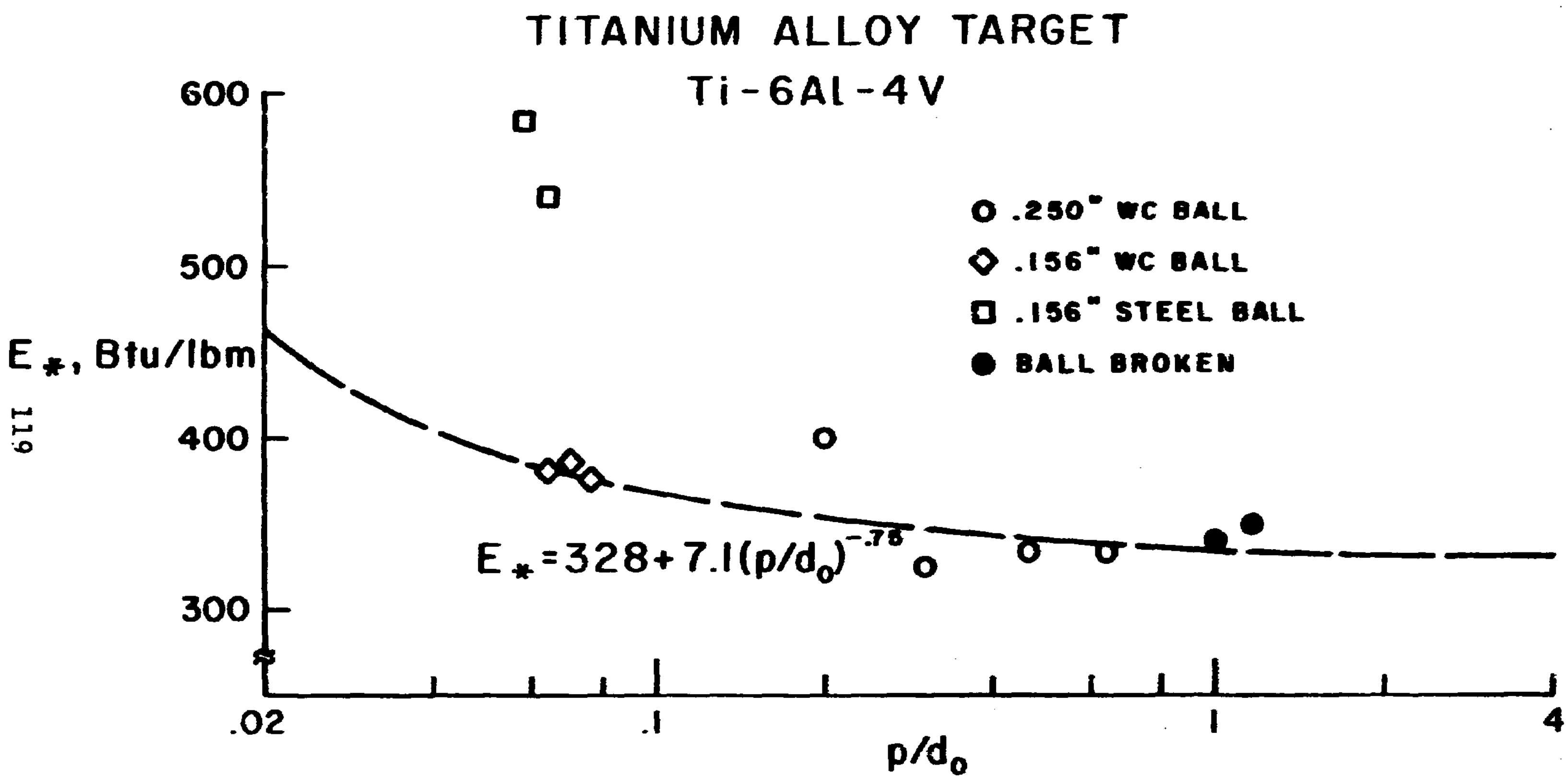
TITANIUM ALLOY TARGET
Ti-6Al-4V
600
500
400
300
E*, Btu/lbm
.02
.1
1
4
p/do
○ .250" WC BALL
◇ .156" WC BALL
□ .156" STEEL BALL
● BALL BROKEN
E* = 328 + 7.1(p/do)^-.75

Figure B-9

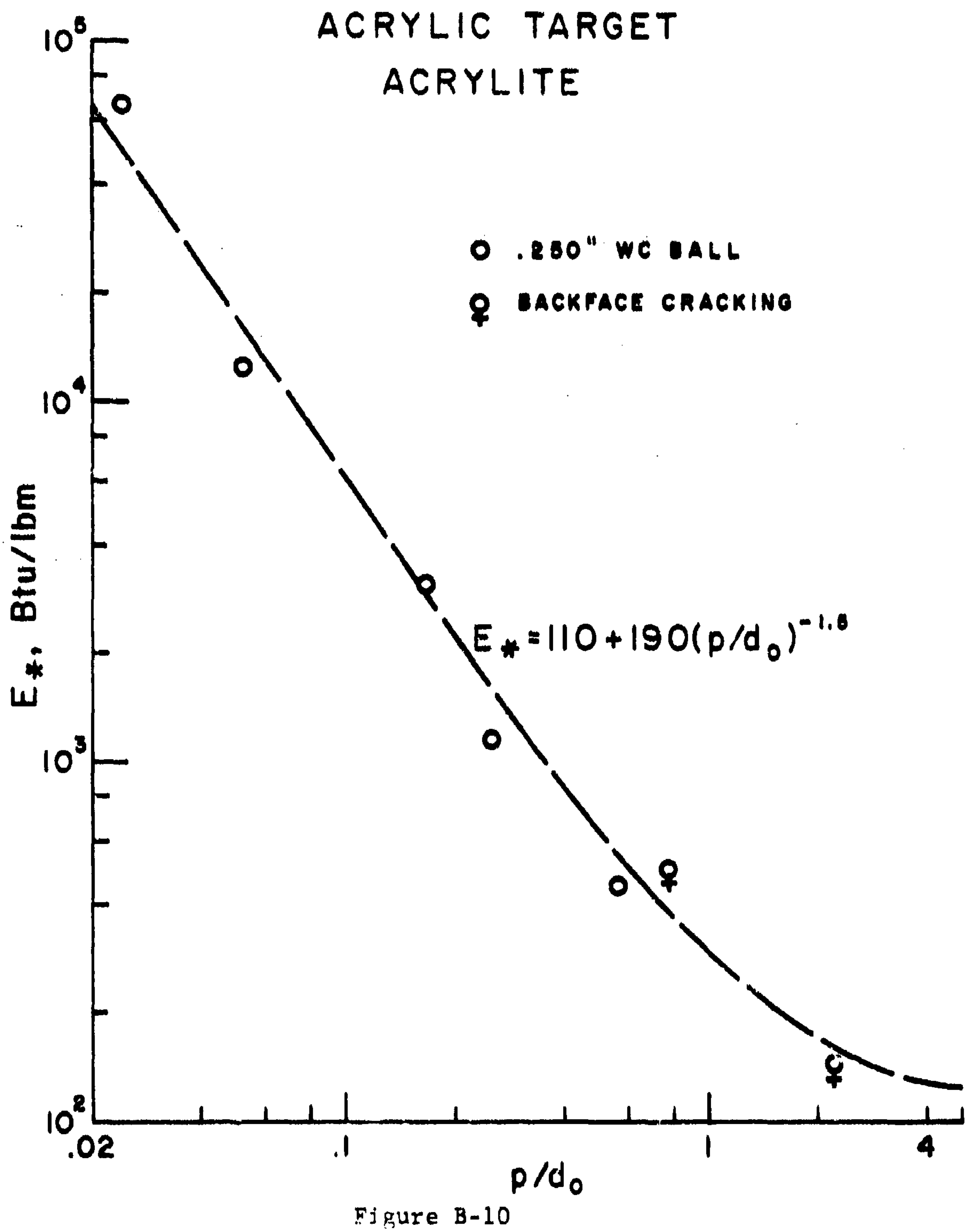
ACRYLIC TARGET
ACRYLITE
.250" WC BALL
BACKFACE CRACKING
$E_* = 110 + 190(p/d_o)^{-1.8}$
E_*, Btu/lbm
10^5
10^4
10^3
10^2
.02
.1
1
4
p/d_o

Figure B-10

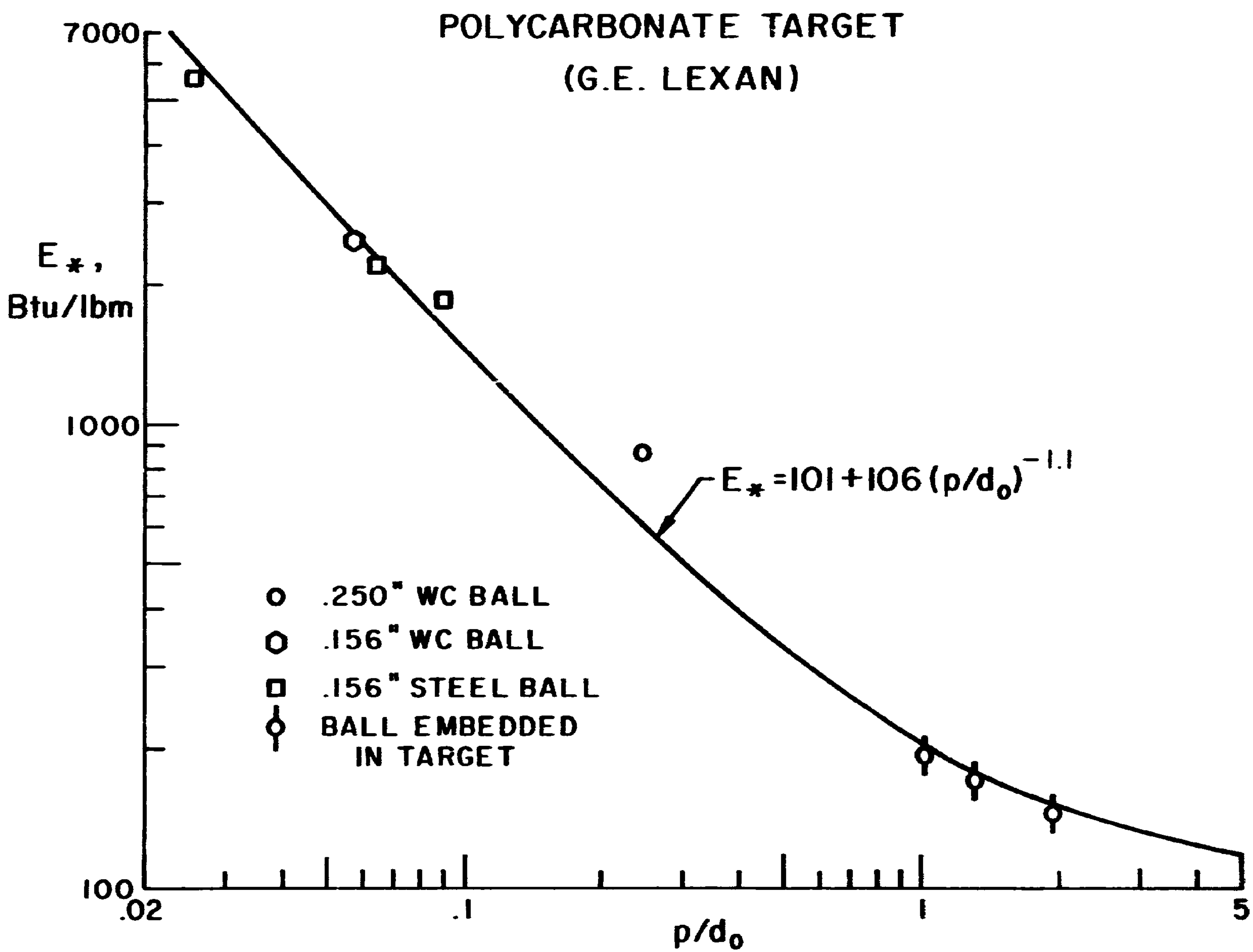
POLYCARBONATE TARGET
(G.E. LEXAN)
E*,
Btu/lbm
7000
1000
100
.02
.1
1
5
p/do
E* = 101 + 106 (p/do)^-1.1
.250" WC BALL
.156" WC BALL
.156" STEEL BALL
BALL EMBEDDED IN TARGET

Figure B-11

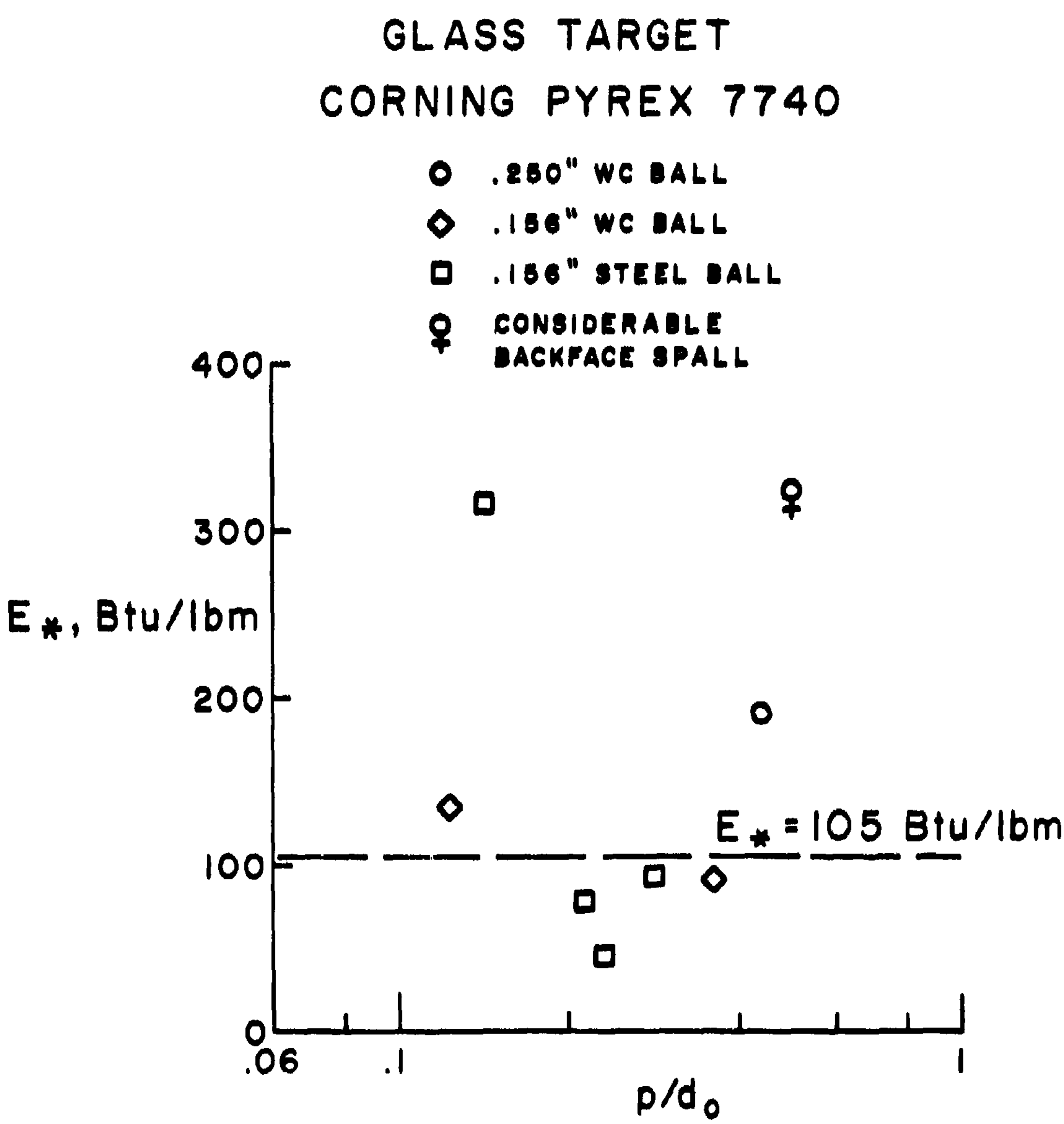
GLASS TARGET
CORNING PYREX 7740
.250" WC BALL
.156" WC BALL
.156" STEEL BALL
CONSIDERABLE BACKFACE SPALL
400
300
200
100
0
E_*, Btu/lbm
$E_* = 105$ Btu/lbm
.06
.1
1
p/d_o

Figure B-12

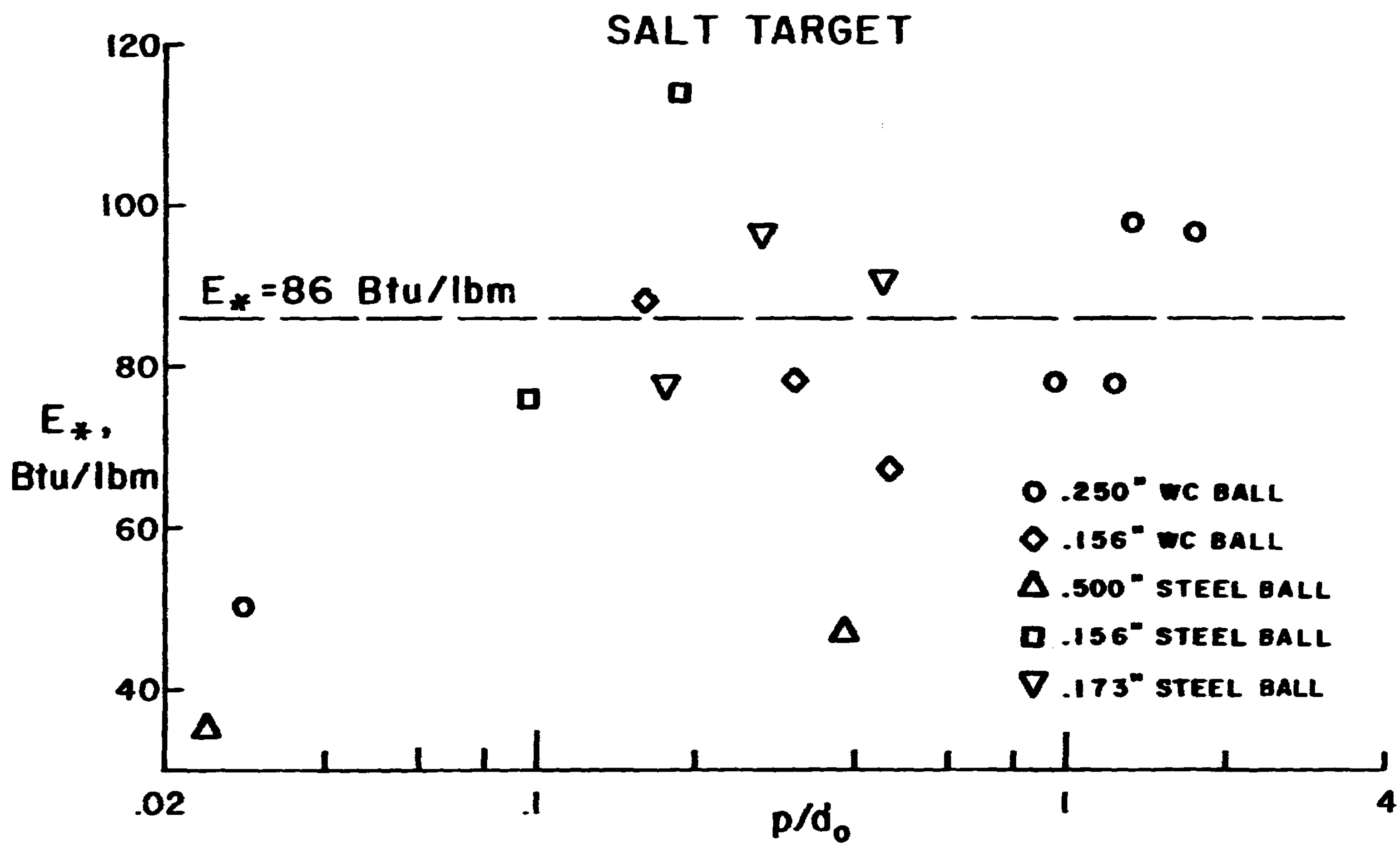
SALT TARGET
120
100
80
60
40
E*, Btu/lbm
E* =86 Btu/lbm
.250" WC BALL
.156" WC BALL
.500" STEEL BALL
.156" STEEL BALL
.173" STEEL BALL
.02
.1
1
4
p/do

Figure B-13

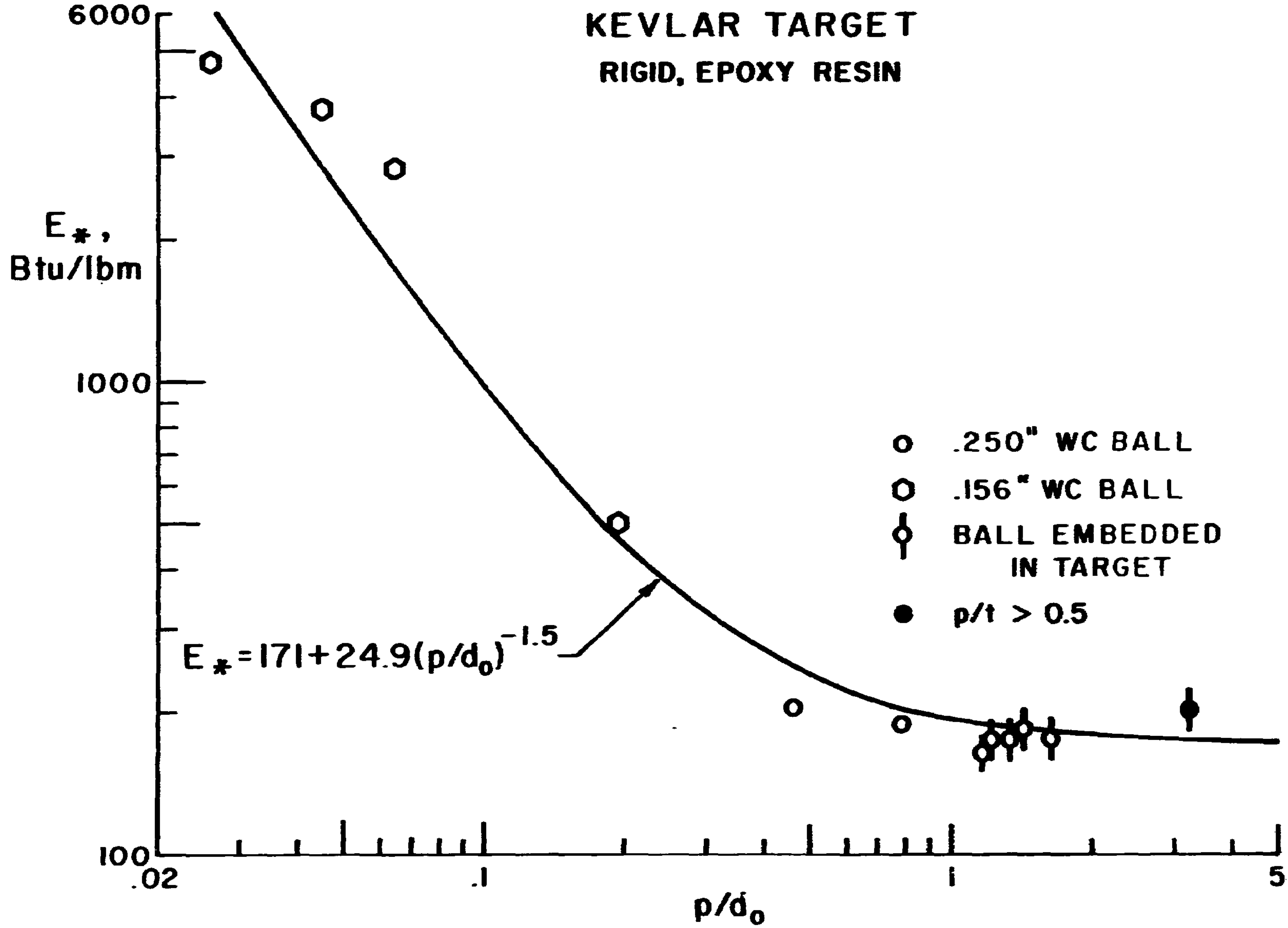

KEVLAR TARGET
RIGID, EPOXY RESIN
6000
1000
100
E*, Btu/lbm
.02
.1
1
5
p/d_o
.250" WC BALL
.156" WC BALL
BALL EMBEDDED IN TARGET
p/t > 0.5
E* = 171 + 24.9(p/d_o)^-1.5

Figure B-14

APPENDIX C

USER'S GUIDE TO ROD CODE

This appendix is a user's guide for the ROD code. It contains:

(1) a summary of the system of nondimensional equations;

(2) an explanation of the method of solution;

(3) FORTRAN listings of the mainline program and all subroutines;

(4) input specifications;

(5) output translation; and

(6) a sample case.

A. Nondimensional Equations

The system of equations which defines the penetration of a long rod projectile is summarized in Table 3. This system consists of 14 first-order ordinary differential equations. It is convenient to solve these equations in nondimensional form. The nondimensional parameters are summarized in Table C-1.

The solution technique requires that the differential equations be in the form

$$Y' = \frac{dY}{dx} = F(x,Y) \quad , \tag{C.1}$$

where Y denotes a column vector of the dependent variables, and x is the independent (time variable). Without going into the details of the algebraic manipulations, it is possible to rearrange the equations to obtain the system summarized in Table C-2. In the order in which the equations are written, each derivative is expressed in terms of the independent variable and the preceding dependent variables as required by Eq. (C.1).

TABLE C-1

NORMALIZATION PARAMETERS

Quantity	Dimensional Symbol	Nondimensional Symbol
Shaft Velocity	V_s	$\bar{V}_s = V_s/V^+$
Head Center of Mass Velocity	V_{cm}	$\bar{V}_{cm} = V_{cm}/V^+$
Head Front Face Velocity	$V_\perp$	$\bar{V}_\perp = V_\perp/V^+$
Head Edge Velocity	V_T	$\bar{V}_T = V_T/V^+$
Interface Velocity	V_b	$\bar{V}_b = V_b/V^+$
Mass in shaft	m_s	$\bar{m}_s = m_s/m_p$
Mass in head	m_h	$\bar{m}_h = m_h/m_p$
Mass eroded	m_b	$\bar{m}_b = m_b/m_p$
Radius of head	b	$\bar{b} = b/\ell_p$
Half thickness of head	ℓ	$\bar{\ell} = \ell/\ell_p$
Depth of Penetration	p	$\bar{p} = p/\ell_p$
Total Kinetic Energy	K	$\bar{K} = K/K_p$
Shaft Kinetic Energy	K_s	$\bar{K}_s = K_s/K_p$
Head Center of Mass Kinetic Energy	K_{cm}	$\bar{K}_{cm} = K_{cm}/K_p$
Head Relative Kinetic Energy	K_r	$\bar{K}_r = K_r/K_p$
Density Ratio		$\bar{\rho} = \rho_t/\rho_p$
Rod L/D		$\bar{L} = \ell_p/2a$
Hydrodynamic Mode Energy of Target	E_*	$\bar{E}_* = E_*/V^{+2}$
Rod Energy Dissipation	E_{*d}	$\bar{E}_{*d} = E_{*d}/V^{+2}$
Adiabatic Yield Strength of Rod	σ	$\bar{\sigma} = \sigma/\rho_p V^{+2}$
Time	t	$\tau = \frac{V^+}{\ell_p} t$

Normalization Parameters are

V^+ = characteristic velocity = 1,000 ft/sec

m_p = initial mass of rod = $\pi a^2 \ell_p \rho_p$

ℓ_p = initial length of rod

K_p = characteristic energy = $\frac{1}{2} m_p V^{+2}$

a = radius of rod

TABLE C-2

NONDIMENSIONAL SYSTEM OF EQUATIONS

$$\bar{V}_s = -\frac{\bar{\sigma}}{\bar{m}_s} f_s$$

$$\bar{m}_b' = 16\, L^2\, \bar{b}\, \bar{\ell}\, \bar{V}_t\, f_h$$

$$\bar{m}_h' = \bar{\delta}\, f_s - \bar{m}_b'$$

$$\bar{m}_s' = -\bar{\delta}\, f_s$$

$$\bar{V}_{cm}' = \frac{1}{\bar{m}_s}\left[-\bar{V}_{cm}\bar{m}_b' - \bar{V}_s\,\bar{m}_s' - \bar{m}_s\,\bar{V}_s' - \bar{V}_{cm}\,\bar{m}_h' - 4\,\bar{b}^2 L^2 \bar{\rho}\left(\bar{E}_* + \frac{C_D}{2}\bar{V}_\perp^2\right)\right]$$

$$\bar{K}_s' = \bar{V}_s^2\,\bar{m}_s' + 2\,\bar{m}_s\,\bar{V}_s\,\bar{V}_s'$$

$$\bar{K}_{cm}' = \bar{V}_{cm}^2\,\bar{m}_h' + 2\,\bar{m}_h\,\bar{V}_{cm}\,V_{cm}'$$

$$\bar{K}_r' = -\bar{m}_b'\left[\bar{V}_T^2 + \frac{1}{3}\left(\bar{V}_\perp - \bar{V}_{cm}\right)^2\right] f_h + 8\,\bar{\rho}\,\bar{b}^2 L^2\left(\bar{V}_{cm} - \bar{V}_\perp\right)\left(\bar{E}_* + \frac{C_D}{2}\bar{V}_\perp^2\right)$$
$$+\, 2\,\bar{\sigma}\, f_s\left(\bar{V}_s - \bar{V}_{cm}\right) - 2\,\bar{m}_s'\left[\frac{\bar{V}_s - \bar{V}_{cm}}{2}^{2} - \bar{E}_{*d}\right]$$

$$K = \bar{K}_s' + \bar{K}_{cm}' + \bar{K}_r'$$

$$\bar{b}' = \bar{V}_t\left(1 - f_h\right)$$

$$\bar{\ell}' = \bar{V}_\perp - \bar{V}_{cm}$$

$$\bar{V}_\perp' = \bar{V}_{cm}' + \frac{2\,\bar{A}\,\bar{D} - 3\,\bar{V}_t\,\bar{C}}{4\,\bar{D}\,\bar{\xi} - 3\,\bar{V}_t\,\bar{E}}$$

$$\bar{V}_T' = \frac{\bar{C} - \bar{E}\bar{\xi}}{2\bar{D}}$$

$$\bar{p}' = \bar{V}_\perp$$

---

where

$f_s = 0 \quad m_s = 0$

$f_s = 1 \quad m_s > 0$

$$\bar{A} = \frac{1}{\bar{m}_h}\left\{3\,\bar{K}_r' - \bar{m}_h'\left[\frac{3}{2}\bar{V}_t^2 + \left(\bar{V}_\perp - \bar{V}_{cm}\right)^2\right]\right\}$$

$f_h = 0 \quad \bar{b} < (1+\varepsilon_o)\bar{b}_o$

$f_h = 1 \quad \bar{b} \geq (1+\varepsilon_o)\bar{b}_o$

$$\bar{D} = 1/\bar{b}$$

$$L = \ell_p/2a$$

$$\bar{E} = 1/\bar{\ell} - f_s/\bar{m}_h$$

$$\bar{\delta} = \bar{V}_s - \bar{V}_b$$

$$\bar{\xi} = \bar{V}_\perp - \bar{V}_{cm}$$

$$C = \left(\frac{\bar{V}_s' - \bar{V}_{cm}'}{\bar{m}_h}\right) f_s - \frac{2}{\bar{b}}\left[\frac{\bar{b}'V_t}{\bar{b}} + \frac{\bar{\xi}}{\bar{\ell}}\left(\bar{b}' + \bar{V}_t\right)\right]$$

B. Method of Solution

The numerical problem is to solve a system of simultaneous first-order ordinary differential equations given the initial value for each variable. The solution technique uses Hamming's modified predictor-corrector method for the solution of general initial value problems. This method is a stable, fourth-order integration procedure that requires the evaluation of the right-hand side of the system only two times per step. This is a great advantage over other methods with the same order of accuracy, such as the Runge-Kutta method, which requires four evaluations of the right-hand side per step. However, the method is not self-starting; that is, the functional values at a single previous point are not enough to get the functional values ahead. Therefore, to get the starting values, a special Runge-Kutta procedure followed by one iteration step is added to the predictor-corrector method. In the ROD code, the subroutine which performs the integration is HPCG - a listing of which is provided later in this appendix. The routine is part of IBM's scientific software package, and precise details of the numerical procedure are available (Ref. 8).

The ROD Code is run in discrete time steps; the size of the steps is controlled by an input parameter. The predictor-corrector method is used to solve an initial value problem for each time interval; the solution at the end of a given time step is the initial condition for the next step.

C. ROD Code Listings

A FORTRAN source listing of the ROD code is provided at the rear of this appendix. The code consists of a mainline routine RODML and four subroutines RODDE, RODES, HPCG, and OUTP. These routines perform the following functions.

RODML - mainline routine which controls:

(1) input and output,

(2) variable initialization,

(3) integration of equations,

(4) computation of auxiliary quantities, and

(5) run termination.

Ref. 8. IBM large computer scientific subroutine package.

RODES - subroutine which evaluates E_{*d}

HPCG - subroutine which integrates the system of equations

RODDE - subroutine which evaluates the derivatives as required by HPCG

OUTP - external output subroutine required by HPCG. It is not used in ROD except insofar as to satisfy the EXTERNAL statement.

D. Input Specifications

The ROD code can be run using card input. The input specifications are shown below. FORTRAN format statements are shown in parentheses.

CARD 1 (1I5) Number of Cases

NCASE - number of impact cases which will be run (no limit)

For each case, the following cards are required.

CARD 2 (40A2) Title Card

ITITL - title or heading which will appear on each page of print-out

CARD 3 (6F10.0) Rod Specifications

VELOC - normalized impact velocity, equal to V/1000 where V is the impact velocity in ft/sec

ELOVD - length to diameter ratio of the rod

EFREE - normalized E_{*d} of the rod material, equal to .01052 x E_* where E_* has the units Btu/lbm

SIGMA - normalized adiabatic yield stress of the rod, equal to .01052 x E_* where E_* has the units Btu/lbm

EPSO - the plastic strain permitted in the head before erosion occurs, present value 0.36

THICK - normalized thickness of the target, equal to T/ℓ_p where T is the thickness of

the target and ℓ_p is the length of the projectile

OBLIQ - angle of incidence, in degrees, from the normal

CARD 4 (2I5) Flag Specifications

NPRNT - number of integration steps between print-outs (usually 10)

NLAYR - number of separate material layers in the target (maximum value - 5)

CARDS 5-9 (4F10.0) Target Specifications

A separate card is needed for each layer of the target.

DENS - ratio of layer material density to projectile material density

ESTR - normalized hydrodynamic mode energy, E_*, of the layer, equal to .02505 x E_* and E_* has the units Btu/lbm

THIK - the normalized line-of-sight thickness of the layer, equal to T_m/ℓ_p where T_m is the line-of-sight thickness of the layer and ℓ_p is the length of the projectile. Note that

$$\text{THICK} = \text{COS(OBLIQ)} \times \sum_{m=1}^{\text{NLAYR}} T_m/\ell_p \; .$$

DTAUI - the integration step size in nondimensional time, usually 0.002. Recall, the non-dimensional time, τ, is related to real time, t, by

$$\tau = 1000\ t/\ell_p \; .$$

The cards for all impact cases must be input prior to execution of the first case. The code will process each case sequentially provided the preceding case is not terminated by an error. If an error occurs, the execution of all subsequent cases is terminated. A successful termination of the case occurs when one of the following occurs:

(1) the total kinetic energy of the rod is less than 0.1% of the initial kinetic energy;

(2) the axial momentum of the rod is less than 0.1% of the initial axial momentum;

(3) the front face of the head of the rod penetrates a distance equal to the total thickness of the target.

There are various conditions for which abrupt termination of the code will occur. When the program terminates prior to successful completion of a case, an error message is printed These errors include:

ERROR 1 - denotes a situation which yields an imaginary solution of the equations. This error is the result of global modeling of the deformation field in the head. There is no solution to the problem using this version of the ROD code although a future version which utilizes a somewhat different formulation for the system of equations will eliminate the error.

ERROR 2 - denotes an error in the solution subroutine HPCG. The predictor-corrector algorithm cannot integrate the equations within its own internal tolerances. The problem may be solved by changing the time step - which is an input item - or the internal tolerances within HPCG - which requires code editing.

ERROR 3 - denotes excessive build-up of integration error. Try a smaller time step.

ERROR 4 - denotes that the code requires more than 2,000 integration steps to complete the case. This error is included to prevent looping. Try running with a larger time step.

In addition to these error messages, there are two additional messages which will occur which are not errors.

END OF LAYER - denotes that the front face of the projectile has penetrated a distance equivalent to the thickness of a layer.

END OF SHAFT - denotes that the shaft has been completely eroded, and only the head of the rod remains.

E. Sample Case and Output Translation

A sample case is presented to illustrate the input specifications and to translate the output. The case is the normal impact of a tungsten alloy rod (Mallory 3000) into a semi-infinite target of rolled homogeneous steel armor. The impact velocity is 5,046 feet per second. The value of E_* for the rod material is 50 Btu/lbm and for the RHA target E_* is 200 Btu/lbm. This case corresponds to an actual test performed by BRL for ARAP.

The input cards for this case are as follows:

CARD 1	1,
CARD 2	MALLORY 3000 ROD INTO RHA AT 5046 FPS
CARD 3	5.046,10.1,.526,.526,.36,1000.,0.
CARD 4	10,1,
CARD 5	0.462,5.01,1000.,.002,

An explanation for each of these inputs is given below.

CARD 1 NCASE = 1 One impact case will be calculated.

CARD 2 Title and page heading for case

CARD 3 $$\text{VELOC} = \frac{V}{V^+} = \frac{5{,}046 \text{ fps}}{1{,}000 \text{ fps}} = 5.046$$

$$\text{ELOVD} = \frac{\ell_p}{D} = \frac{80.26 \text{ mm}}{7.92 \text{ mm}} = 10.1$$

$$\text{EFREE} = \frac{E_{*d}}{V^{+2}} = \frac{.42E_*}{V^{+2}} = \frac{(.42)(50 \frac{\text{Btu}}{\text{lbm}})}{10^6 \frac{\text{ft}^2}{\text{sec}^2}} \times 2.505 \times 10^4 \frac{\text{ft}^2/\text{sec}^2}{\text{Btu/lbm}}$$

$$= .01052 \times 50 = .526$$

Note the conversion factor required to make EFREE dimensionless.

$$\text{SIGMA} = \frac{\sigma}{\rho_p V^{+2}} = \frac{.42\rho_p E_*}{\rho_p V^{+2}} = \frac{.42\ E_*}{V^{+2}} = \text{EFREE} = .526$$

EPSO = .36 (model parameter)

THICK = T/ℓ_p = 1000 (very large value to approximate semi-infinite target)

OBLIQ = 0. (normal impact)

CARD 4 NPRNT = 10 The solution for every tenth integration step will be printed. In addition, printouts automatically occur for the first step and for significant steps such as layer penetration.

NLAYR = 1 The target consists of one layer.

CARD 5 DENS $= \dfrac{\rho_t}{\rho_p} = \dfrac{7.86 \text{ gm/cc}}{17.0 \text{ gm/cc}} = .462$

ESTR $= \dfrac{E_*}{V^{+2}} = \dfrac{200 \frac{\text{Btu}}{\text{lbm}}}{10^6 \frac{\text{ft}^2}{\text{sec}^2}} \times 2.505 \times 10^4 \dfrac{\text{ft}^2/\text{sec}^2}{\text{Btu/lbm}} = 5.01$

THIK $= \dfrac{T_m}{\ell_p} = 1000$ (very large value to approximate semi-infinite layer)

DTAUI = .002 nondimensional time step.

The output for this case is shown on the following pages. The top of the first output page contains a summary of the input specifications for the case. This is followed by three lines of headings for the output parameters. Table C-3 provides a translation for each of these parameters. Each three line grouping beneath these headings provides the solution of the system of equations at the indicated time. Thus, the time history (or the history versus depth of penetration) for any of the variables is readily available. The final grouping of three lines is the solution at the final time step. In this case, the penetration terminates at τ = .402 (which corresponds to t = 106 μ sec), and the rod has penetrated a distance PEN = .954 (which corresponds to .954 x 80.26 mm = 76.6 mm). The run is terminated at this point because the total kinetic energy in the head is less than 0.1% of the initial kinetic energy in the rod.

Table C-3

OUTPUT TRANSLATION

Output Heading	Symbol	Definition
TAU	τ	Table C-1
VS	$\bar{V}_s$	Table C-1
VCM	$\bar{V}_{cm}$	Table C-1
V-PERP	$\bar{V}_\perp$	Table C-1
VT	$\bar{V}_T$	Table C-1
VB	$\bar{V}_b$	Table C-1
WIDTH	–	$= 2 \times \bar{b}$ (Table C-1)
THICK	–	$= 2 \times \bar{\ell}$ (Table C-1)
PEN	$\bar{p}$	Table C-1
MH	$\bar{m}_h$	Table C-1
MS	$\bar{m}_s$	Table C-1
MB	$\bar{m}_b$	Table C-1
MASS RATIO	–	$= (\bar{m}_h + \bar{m}_s)/\bar{m}_p$
Y HEAD	–	$= \bar{p}$
ESTAR	E_*	E_{*p} in Btu/Lbm
K	$\bar{K}$	Table C-1
KCM	$\bar{K}_{cm}$	Table C-1
KS	$\bar{K}_s$	Table C-1
KR	$\bar{K}_r$	Table C-1
K-DISS	$\bar{K}_d$	$= \bar{K}_o - \bar{K}_{cm} - \bar{K}_s - \bar{K}_r$ $\bar{K}_o$ = initial kinetic energy

A. R. A. P. INC.
TWO CELL ROD PROGRAM

MALLORY 3000 ROD INTO RHA AT 5046 FPS

NCASE	NPRNT	NLAYR	THICK
2	10	1	0.1000E+04

ROD	VELOCITY	L/D	SIGMA	EPS0	E* FREE	CD	OBLIQ
	0.5046E+01	0.1010E+02	0.5260E+00	0.3600E+00	0.5260E+00	0.1000E+01	0.0000E+00

TARGET LAYER 1	DENS	THICK	ESTR	DTAU
	0.4620E+00	0.1000E+04	0.5010E+01	0.2000E-02

TAU PEN K	VS MH KCM	VCM MS KS	V-PERP MB KR	VT MASS RATIO K-DISS	VB VHEAD	WIDTH ESTAR	THICK
0.0000E+00	0.5046E+01	0.4945E+01	0.4844E+01	0.5046E-01	0.5046E+01	0.9901E-01	0.9901E-01
0.0000E+00	0.9901E-01	0.9010E+00	0.0000E+00	0.1000E+01	0.0000E+00	0.0000E+00	
0.2536E+02	0.2421E+01	0.2294E+02	0.4622E-03	0.9937E-01			
0.2000E-01	0.5046E+01	0.3766E+01	0.2247E+01	0.1917E+01	0.5205E+01	0.1348E+00	0.5342E-01
0.6394E-01	0.9901E-01	0.9010E+00	0.0000E+00	0.1000E+01	0.6394E-01	0.2000E+03	
0.2460E+02	0.1405E+01	0.2294E+02	0.2500E+00	0.8585E+00			
0.4000E-01	0.5037E+01	0.2615E+01	0.2436E+01	0.2479E+01	0.2793E+01	0.1348E+00	0.2130E-01
0.1100E+00	0.3948E-01	0.8782E+00	0.8230E-01	0.9177E+00	0.1100E+00	0.2000E+03	
0.2265E+02	0.2699E+00	0.2228E+02	0.1218E+00	0.2793E+01			
0.6000E-01	0.5024E+01	0.2493E+01	0.2471E+01	0.2530E+01	0.2514E+01	0.13[illegible]E+00	0.1861E-01
0.1591E+00	0.3449E-01	0.8294E+00	0.1361E+00	0.8639E+00	0.1591E+00	0.2000E+03	
0.2125E+02	0.2143E+00	0.2094E+02	0.1104E+00	0.4200E+01			
0.8000E-01	0.5011E+01	0.2483E+01	0.2480E+01	0.2531E+01	0.2486E+01	0.1348E+00	0.1822E-01
0.2087E+00	0.3377E-01	0.7790E+00	0.1872E+00	0.8128E+00	0.2087E+00	0.2000E+03	
0.1986E+02	0.2082E+00	0.1956E+02	0.1081E+00	0.5583E+01			
0.1000E+00	0.4997E+01	0.2474E+01	0.2474E+01	0.2525E+01	0.2474E+01	0.1348E+00	0.1817E-01
0.2582E+00	0.3368E-01	0.7285E+00	0.2378E+00	0.7622E+00	0.2582E+00	0.2000E+03	
0.1849E+02	0.2061E+00	0.1819E+02	0.1074E+00	0.6956E+01			
0.1200E+00	0.4982E+01	0.2463E+01	0.2463E+01	0.2520E+01	0.2464E+01	0.1348E+00	0.1817E-01
0.3076E+00	0.3367E-01	0.6781E+00	0.2882E+00	0.7118E+00	0.3076E+00	0.2000E+03	
0.1713E+02	0.2043E+00	0.1683E+02	0.1069E+00	0.8318E+01			
0.1400E+00	0.4966E+01	0.2452E+01	0.2452E+01	0.2515E+01	0.2452E+01	0.1348E+00	0.1817E-01
0.3567E+00	0.3367E-01	0.6278E+00	0.3386E+00	0.6614E+00	0.3567E+00	0.2000E+03	
0.1577E+02	0.2025E+00	0.1548E+02	0.1065E+00	0.9670E+01			
0.1600E+00	0.4949E+01	0.2440E+01	0.2440E+01	0.2510E+01	0.2440E+01	0.1348E+00	0.1817E-01
0.4057E+00	0.3367E-01	0.5776E+00	0.3888E+00	0.6112E+00	0.4057E+00	0.2000E+03	
0.1443E+02	0.2005E+00	0.1414E+02	0.1061E+00	0.1101E+02			
0.1800E+00	0.4930E+01	0.2427E+01	0.2427E+01	0.2505E+01	0.2427E+01	0.1348E+00	0.1817E-01
0.4543E+00	0.3366E-01	0.5275E+00	0.4389E+00	0.5611E+00	0.4543E+00	0.2000E+03	
0.1310E+02	0.1983E+00	0.1282E+02	0.1056E+00	0.1234E+02			

MALLORY 3000 ROD INTO RHA AT 5046 FPS

TAU PEN K	VS MH KCM	VCM MS KS	V-PERP MB KR	VT MASS RATIO K-DISS	VB YHEAD	WIDTH ESTAR	THICK
0.2000E+00	0.4909E+01	0.2413E+01	0.2413E+01	0.2498E+01	0.2413E+01	0.1348E+00	0.1817E-01
0.5027E+00	0.3366E-01	0.4775E+00	0.4889E+00	0.5111E+00	0.5027E+00	0.2000E+03	
0.1179E+02	0.1959E+00	0.1150E+02	0.1050E+00	0.1366E+02			
0.2200E+00	0.4885E+01	0.2397E+01	0.2397E+01	0.2491E+01	0.2397E+01	0.1348E+00	0.1817E-01
0.5508E+00	0.3365E-01	0.4276E+00	0.5387E+00	0.4613E+00	0.5508E+00	0.2000E+03	
0.1049E+02	0.1933E+00	0.1021E+02	0.1044E+00	0.1496E+02			
0.2400E+00	0.4859E+01	0.2379E+01	0.2378E+01	0.2484E+01	0.2379E+01	0.1348E+00	0.1816E-01
0.5986E+00	0.3364E-01	0.3779E+00	0.5885E+00	0.4115E+00	0.5966E+00	0.2000E+03	
0.9201E+01	0.1903E+00	0.8923E+01	0.1038E+00	0.1624E+02			
0.2600E+00	0.4829E+01	0.2358E+01	0.2358E+01	0.2475E+01	0.2358E+01	0.1348E+00	0.1816E-01
0.6460E+00	0.3364E-01	0.3284E+00	0.6380E+00	0.3620E+00	0.6460E+00	0.2000E+03	
0.7932E+01	0.1870E+00	0.7659E+01	0.1030E+00	0.1751E+02			
0.2800E+00	0.4795E+01	0.2334E+01	0.2334E+01	0.2464E+01	0.2334E+01	0.1348E+00	0.1816E-01
0.6929E+00	0.3363E-01	0.2791E+00	0.6873E+00	0.3127E+00	0.6929E+00	0.2000E+03	
0.6684E+01	0.1832E+00	0.6416E+01	0.1021E+00	0.1876E+02			
0.3000E+00	0.4753E+01	0.2306E+01	0.2306E+01	0.2452E+01	0.2306E+01	0.1348E+00	0.1815E-01
0.7393E+00	0.3361E-01	0.2380E+00	0.7364E+00	0.2636E+00	0.7393E+00	0.2000E+03	
0.5459E+01	0.1788E+00	0.5196E+01	0.1010E+00	0.1999E+02			
0.3200E+00	0.4702E+01	0.2271E+01	0.2271E+01	0.2437E+01	0.2272E+01	0.1348E+00	0.1814E-01
0.7851E+00	0.3360E-01	0.1812E+00	0.7852E+00	0.2148E+00	0.7851E+00	0.2000E+03	
0.4262E+01	0.1733E+00	0.4006E+01	0.9972E-01	0.2118E+02			
0.3400E+00	0.4634E+01	0.2226E+01	0.2226E+01	0.2416E+01	0.2227E+01	0.1348E+00	0.1813E-01
0.8301E+00	0.3357E-01	0.1328E+00	0.8336E+00	0.1664E+00	0.8301E+00	0.2000E+03	
0.3100E+01	0.1664E+00	0.2852E+01	0.9600E-01	0.2235E+02			
0.3600E+00	0.4536E+01	0.2162E+01	0.2161E+01	0.2387E+01	0.2163E+01	0.1348E+00	0.1810E-01
0.8740E+00	0.3352E-01	0.8500E-01	0.8815E+00	0.1185E+00	0.8740E+00	0.2000E+03	
0.1984E+01	0.1567E+00	0.1748E+01	0.9548E-01	0.2346E+02			
0.3800E+00	0.4356E+01	0.2053E+01	0.2049E+01	0.2334E+01	0.2056E+01	0.1348E+00	0.1802E-01
0.9162E+00	0.3337E-01	0.3816E-01	0.9285E+00	0.7150E-01	0.9162E+00	0.2000E+03	
0.9381E+00	0.1406E+00	0.7234E+00	0.9087E-01	0.2451E+02			
0.3960E+00	0.3730E+01	0.1792E+01	0.1727E+01	0.2190E+01	0.1050E+01	0.1348E+00	0.1755E-01
0.9473E+00	0.3250E-01	0.3089E-02	0.9644E+00	0.3555E-01	0.9473E+00	0.2000E+03	
0.2079E+00	0.1044E+00	0.4233E-01	0.7797E-01	0.2524E+02			
END OF SHAFT							
0.4000E+00	0.0000E+00	0.1326E+01	0.8831E+00	0.1983E+01	0.1760E+01	0.1348E 00	0.1505E-01
0.9525E+00	0.2786E-01	0.0000E+00	0.9720E+00	0.2801E-01	0.9525E+00	0.2000E+03	
0.1055E+00	0.4896E-01	0.0000E+00	0.5658E-01	0.2536E+02			
0.4020E+00	0.0000E+00	0.9814E+00	0.5818E+00	0.2015E+01	0.1381E+01	0.1348E+00	0.1337E-01
0.9540E+00	0.2475E-01	0.0000E+00	0.9751E+00	0.2489E-01	0.9540E+00	0.2000E+03	
0.7536E-01	0.2382E-01	0.0000E+00	0.5154E-01	0.2539E+02			

```
C RODML,FTN-----ROD PROGRAM MAINLINE
C
C          THIS PROGRAM COMPUTES THE BEHAVIOR OF A
C          TWO-ELEMENT ROD WITH A DEFORMING HEAD
C
      EXTERNAL RODDE,OUTP
C
      COMMON BMAX,SIGMA,ELOVD,ESTBK,EFREE,THICK,RHO,ESTRT,CD,FS
      COMMON OBLIQ,ESTAR,PPROJ,LBDOT,ILAYR,NLAYR,LSHFT
C
C
      DIMENSION PRMT(5),Y(15),DERY(15),AUX(16,15)
      DIMENSION X(15),ITITL(40)
      DIMENSION DENS(5),ESTR(5),THIK(5),DTAUI(5)
C
      DATA NIN,ICASE,NDIM/5,0,15/
C
1000  FORMAT (16I5)
1001  FORMAT (40A2)
1002  FORMAT (8F10.0)
2001  FORMAT (1H1,54X,'A. R. A. P. INC.')
2002  FORMAT (1H ,51X,'TWO CELL ROD PROGRAM')
2003  FORMAT (1H0,40A2)
2004  FORMAT (1H0,3X,'NCASE',5X,'NPRNT',5X,'NLAYR',9X,'THICK')
2005  FORMAT (1H ,3X,I5,5X,I5,5X,I5,1X,E13.4)
2006  FORMAT (1H0,7X,'ROD',5X,'VELOCITY',9X,'L/D',12X,'SIGMA',9X,'EPS0',
     1    11X,'E* FREE',10X,'CD',7X,'OBLIQ')
2007  FORMAT (1H ,10X,8(E14.4,1X))
2008  FORMAT (1H0,4X,'TARGET LAYER',I2,6X,'DENS',10X,'THICK',9X,
     1 'ESTR',13X,'DTAU')
2009  FORMAT (1H0,7X,'TAU',10X,'VS',11X,'VCM',10X,'V-PERP',10X,'VT',12X,
     1           'VB',10X,'WIDTH',9X,'THICK')
2010  FORMAT (1H ,7X,'PEN',10X,'MH',11X,'MS',13X,'MB',9X,'MASS RATIO',
     1 7X,'YHEAD',8X,'ESTAR')
2011  FORMAT (1H ,7X,'K',12X,'KCM',10X,'KS',13X,'KR',10X,'K-DISS')
2012  FORMAT (1H ,9E14.4)
2013  FORMAT (1H )
2014  FORMAT (1H1)
2016  FORMAT (1H ,18X,7(E14.4,1X))
3001  FORMAT (1H ,'ERROR 4')
3002  FORMAT (1H0,'ERROR 2')
3004  FORMAT (1H ,'END OF LAYER',I2)
3005  FORMAT (1H ,'END OF SHAFT')
3006  FORMAT (1H ,'ERROR 3')
C
      NOUT=6
C
C                        READ INPUT CARDS
C
      READ (NIN,1000) NCASE
10    ICASE=ICASE+1
      IF (ICASE. LE. NCASE) GO TO 20
      CALL EXIT
20    READ (NIN,1001) ITITL
      READ (NIN,1002) VELOC,ELOVD,EFREE,SIGMA,EPS0,THICK,OBLIQ
      READ (NIN,1000) NPRNT,NLAYR
      DO 21 N=1,NLAYR
      READ (NIN,1002) DENS(N),ESTR(N),THIK(N),DTAUI(N)
21    CONTINUE
C
C                       INITIALIZE X VECTOR
```

```
C
C     X(1)   IS   VB
C     X(2)   IS   VCM
C     X(3)   IS   VPERP
C     X(4)   IS   VT
C     X(5)   IS   MB
C     X(6)   IS   MH
C     X(7)   IS   MS
C     X(8)   IS   B
C     X(9)   IS   L
C     X(10)  IS   K
C     X(11)  IS   KS
C     X(12)  IS   KCM
C     X(13)  IS   KR
C     X(14)  IS   P
C     X(15)  IS  YHEAD
C
      MXSTP=2000
      STOP=.001
      TOLER=.001
      ZKSTR=.01
      ESTBK=1.0
      ZKLB=1.0
      CD=1.0
      X(1)=VELOC
      X(4)=ZKSTR*VELOC
      BZRO=0.5/ELOVD
      ELZRO=ZKLB*BZRO
      ELOVB=ELZRO/BZRO
      DISS=ZKSTR*(4.0*ELOVB-(0.5+16.*ELOVB*ELOVB/3.0)*ZKSTR)
      X(2)=VELOC-2.0*ELOVB*X(4)
      X(3)=X(2)-2.0*ELOVB*X(4)
      X(5)=0.0
      X(6)=8.0*ELOVD*ELOVD*BZRO*BZRO*ELZRO
      X(7)=1.0-X(6)
      X(8)=BZRO
      X(9)=ELZRO
      X(11)=X(7)*X(1)*X(1)
      X(12)=X(6)*X(2)*X(2)
      XI=X(3)-X(2)
      X(13)=X(6)*(1.5*X(4)*X(4)+XI*XI)/3.0
      X(10)=X(11)+X(12)+X(13)
      X(14)=0.0
      X(15)=0.0
      DO 30 I=1,NDIM
      Y(I)=X(I)
30    CONTINUE
C
C
C                        PRINT THE INPUT
C
      WRITE (NOUT,2001)
      WRITE (NOUT,2002)
      WRITE (NOUT,2003) ITITL
      WRITE (NOUT,2004)
      WRITE (NOUT,2005) NCASE,NPRNT,NLAYR,THICK
      WRITE (NOUT,2006)
      WRITE (NOUT,2007) VELOC,ELOVD,SIGMA,EPSO,EFREE,CD,OBLIQ
      DO 40 N=1,NLAYR
      WRITE (NOUT,2008) N
      WRITE (NOUT,2016) DENS(N),THIK(N),ESTR(N),DTAUI(N)
40    CONTINUE
C
```

```
C                         INITIALIZE REMAINING PARAMETERS
C
      TAU=0.0
      TAUM=0.0
      ILAYR=1
      LAYFG=0
      LCORR=0
      LSHFT=1
      FS=0.0
      OBLIQ=OBLIQ*0.01745329
      THEND=THICK/COS(OBLIQ)
      DTAU=DTAUI(ILAYR)
      RHO=DENS(ILAYR)
      ESTRT=ESTR(ILAYR)
      TAULR=THIK(ILAYR)
      BMAX=(1.0+EPSO)*BZRO
      ZMOMO=VELOC
      ZENO=VELOC*VELOC
      KPT=-1
      ISTEP=1
      ITAU=0
      LEXIT=0
      LFLAG=0
      LTERM=0
      LPRNT=1
      LLINE=12+3*(NLAYR-1)
      LBDOT=1
      GO TO 155
  100 DO 120 I=1,NDIM
      Y(I)=X(I)
  120 CONTINUE
C
C                         PREPARE FOR HPCG INTEGRATION
C
      DO 200 ISTEP=2,MXSTP
      TAU=TAUM+DTAU
      PRMT(1)=TAUM
      PRMT(2)=TAU
      PRMT(3)=DTAU/15.
      PRMT(4)=0.01
      TEMP=1.0/NDIM
      DO 130 I=1,NDIM
      DERY(I)=TEMP
  130 CONTINUE
C
C                         INTEGRATE THE SYSTEM OF EQUATIONS
C
      CALL HPCG(PRMT,Y,DERY,NDIM,IHLF,RODDE,OUTP,AUX)
      IF (IHLF. LE. 10) GO TO 131
      WRITE (NOUT,3002)
      CALL EXIT
C
C                        CHECK FOR LAYER PENETRATION
C
  131 TAUOK=(1.0-TOLER)*TAULR
      IF (Y(15). LT. TAUOK) GO TO 135
      TAUBG=(1.0+TOLER)*TAULR
      IF (Y(15). LE. TAUBG) GO TO 133
      RATIO=(TAULR-X(15))/(Y(15)-X(15))
      DTAU=DTAU*RATIO
      TAU=TAUM
      GO TO 100
  133 ILAYR=ILAYR+1
```

```
      DTAU=DTAUI(ILAYR)
      RHO=DENS(ILAYR)
      ESTRT=ESTR(ILAYR)
      TAULR=TAULR+THIK(ILAYR)
      LPRNT=1
      LAYFG=1
      IF (ILAYR. GT. NLAYR) LTERM=1
C
C                        STOP THE GROWTH OF THE HEAD
C
 135  IF (Y(15). GT. Y(14)) Y(14)=Y(15)
      IF (Y(7). GT. 0.0) GO TO 1359
      Y(7)=0.0
      Y(1)=0.0
      Y(11)=0.0
 1359 GO TO (1351,1352,136),LBDOT
 1351 IF (Y(8). GT. BMAX) GO TO 1352
      BPRED=2.0*Y(8)-X(8)
      IF (BPRED. LT. BMAX) GO TO 136
      SLOPE=(BMAX-Y(8))/(BPRED-Y(8))
      DTAU=(TAU-TAUM)*SLOPE
      LBDOT=2
      GO TO 136
 1352 BMAX=Y(8)
      DTAU=DTAUI(ILAYR)
      LBDOT=3
C
C                        PREDICT LAYER PENETRATION
C
 136  IF (LAYFG. EQ. 1) GO TO 1369
      YPRED=2.0*Y(15)-X(15)
      TAUOK=(1.0-TOLER)*TAULR
      IF (YPRED. LT. TAUOK) GO TO 1369
      RATIO=(TAULR-Y(15))/(YPRED-Y(15))
      DTAUP=RATIO*(TAU-TAUM)
      IF (DTAUP. GE. DTAU) GO TO 1369
      DTAU=DTAUP
      IF (LBDOT. EQ. 2) LBDOT=1
C
C                        PREDICT END OF SHAFT
C
 1369 GO TO (1370,1371,1374),LSHFT
 1370 PDQMS=2.0*Y(7)-X(7)
      IF (PDQMS. GT. 0.0) GO TO 1373
      RATIO=Y(15)/(Y(15)-PDQMS)
      DTAUP=RATIO*(TAU-TAUM)
      IF (DTAUP. LT. DTAU) DTAU=DTAUP
      LSHFT=2
      LPRNT=1
      GO TO 1373
 1371 LSHFT=3
      Y(1)=0.0
      Y(7)=0.0
      Y(11)=0.0
      Y(4)=0.5*Y(8)*(Y(2)-Y(3))/Y(9)
      FACT=ZKSTR*Y(2)
      IF (Y(4). GE. FACT) GO TO 13715
      Y(4)=FACT
      Y(3)=Y(2)-2.0*Y(4)*Y(9)/Y(8)
13715 Y(13)=Y(6)*(0.5*Y(4)*Y(4)+(Y(3)-Y(2))**2/3.0)
      Y(10)=Y(13)+Y(12)+Y(11)
C
C                TIME STEP AND PREDICTIONS FOR NEXT STEP COMPLETE
```

```
C
 1373  VB=Y(3)+2.0*(Y(2)-Y(3))
       IF (VB. GE. Y(1)) GO TO 13735
       FS=1.0
       IF (LCORR. EQ. 1) GO TO 13738
       Y(4)=0.5*Y(8)*((Y(1)-VB)/Y(6)-(Y(3)-Y(2))/Y(9))
       Y(13)=Y(6)*(Y(4)*Y(4)/2.0+(Y(3)-Y(2))**2/3.0)
       LCORR=1
       GO TO 13738
 13735 FS=0.0
       LCORR=0
 13738 CONTINUE
       IF (LSHFT. GE. 3) GO TO 1374
       IF (Y(1). GT. VB. OR. Y(7). GT. 0.5) GO TO 1374
       LPRNT=1
       GO TO 1371
 1374  TEMP=Y(5)-X(5)
       IF (TEMP. EQ. 0.0) GO TO 13741
       PPROJ=Y(14)+(.950-Y(5))*(Y(14)-X(14))/TEMP
 13741 DO 1375 I=1,NDIM
       X(I)=Y(I)
 1375  CONTINUE
       TAUM=TAU
C
C                  CHECK FOR RUN TERMINATION
C
       ZMOM=Y(7)*Y(1)+Y(6)*Y(2)
       RAMOM=ZMOM/ZMOMO
       IF (RAMOM. GT. STOP) GO TO 140
       LTERM=1
       GO TO 150
 140   ZENER=Y(7)*Y(1)*Y(1)+Y(6)*Y(2)*Y(2)
       RAENR=ZENER/ZENO
       IF (RAENR. GT. STOP) GO TO 150
       LTERM=1
 150   IF (Y(14). LT. THEND) GO TO 155
       LTERM=1
C
C                        CHECK THE FLAGS
C
 155   KPT=KPT+1
       IF (ISTEP. EQ. 1) GO TO 190
       IF (KPT. NE. NPRNT) GO TO 165
       LPRNT=1
       KPT=0
 165   IF (LTERM. EQ. 1. OR. LEXIT. EQ. 1) LPRNT=1
       IF (LPRNT. EQ. 0) GO TO 200
       IF (LFLAG. EQ. 0) GO TO 195
C
C                         PRINT THE PAGE HEADINGS
C
 190   IF (LLINE. NE. 0) GO TO 193
       WRITE (NOUT,2014)
       WRITE (NOUT,2003) ITITL
 193   WRITE (NOUT,2009)
       WRITE (NOUT,2010)
       WRITE (NOUT,2011)
       LLINE=LLINE+4
       LFLAG=0
C
C                        COMPUTE AUXILIARY QUANTITIES
C
 195   VB=Y(3)+2.0*(Y(2)-Y(3))
```

```
      WIDTH=2.0*Y(8)
      THIC=2.0*Y(9)
      RATM=1.0-Y(5)
      DISSK=VELOC*VELOC-Y(11)-Y(12)-Y(13)
      HEADM=8.0*ELOVD*ELOVD*Y(8)*Y(8)*Y(9)
      RELK=Y(6)*(1.5*Y(4)*Y(4)+(Y(3)-Y(2))**2)/3.0
      ERRM=1.0-HEADM/Y(6)
      IF (ERRM. LE. .5. OR. LSHFT. GE. 3) GO TO 1955
      WRITE (NOUT,3006)
      CALL EXIT
 1955 ERRK=1.0-RELK/Y(13)
      E=ESTAR*39.91761
C
C                      PRINT THE OUTPUT
C
      WRITE (NOUT,2012) TAU,Y(1),Y(2),Y(3),Y(4),VB,WIDTH,THIC
      WRITE (NOUT,2012) Y(14),Y(6),Y(7),Y(5),RATM,Y(15),E
      WRITE (NOUT,2012) Y(10),Y(12),Y(11),Y(13),DISSK
      IF (LAYFG. EQ. 0) GO TO 196
      ILAY=ILAYR-1
      WRITE (NOUT,3004) ILAY
      LAYFG=0
 196  IF (LSHFT. EQ. 2) WRITE (NOUT,3005)
      WRITE (NOUT,2013)
      LLINE=LLINE+4
      LPRNT=0
      IF (LLINE. LE. 55) GO TO 197
      LFLAG=1
      LLINE=0
 197  IF (LTERM. NE. 0) GO TO 10
      IF (ISTEP. EQ. 1) GO TO 100
      IF (LEXIT. EQ. 0) GO TO 200
      IF (ISTEP. EQ. MXSTP) WRITE (NOUT,3001)
      CALL EXIT
 200  CONTINUE
      END
C
```

```
C RODDE-----ROD PROGRAM   DERIVATIVE EVALUATION
      SUBROUTINE RODDE(X,Y,DERY)
C
C            THIS SUBROUTINE IN THE ROD PROGRAM
C            EVALUATES DERIVATIVES FOR HPCG INTEGRATION
C
      COMMON BMAX,SIGMA,ELOVD,ESTRK,EFREE,THICK,RHO,ESTRT,CD,FS
      COMMON OBLIQ,ESTAR,PPROJ,LBDOT,ILAYR,NLAYR,LSHFT
C
      DIMENSION DERY(15),Y(15)
C
1000  FORMAT (1H0,'ERROR 1')
C
C                          INITIALIZE VARIABLES FOR THIS STEP
C
      NOUT=6
      VS=Y(1)
      VCM=Y(2)
      VPERP=Y(3)
      VT=Y(4)
      EMB=Y(5)
      EMH=Y(6)
      EMS=Y(7)
      B=Y(8)
      EL=Y(9)
      EK=Y(10)
      EKS=Y(11)
      EKCM=Y(12)
      EKR=Y(13)
      PEN=Y(14)
      YHEAD=Y(15)
C
C                          PARAMETER DEFINITIONS
C
      XI=VPERP-VCM
      DELTA=VS-VPERP+2.0*XI
      BSQ=B*B
      ELDSQ=ELOVD*ELOVD
C
C                             CHECK DISCRIMINANT OF QUADRATIC TERM
C
      BIGA=4.0*B*EL/(2.0*BSQ-FS/4.0/ELDSQ)
      BIGB=FS/(BSQ*ELDSQ*8.0-FS)
      QUAD1=(3.0+2.0*BIGA*BIGA)*EKR/EMH
      FACT=VS-VCM
      QUAD2=BIGB*BIGB*FACT*FACT
      QUAD=QUAD1-QUAD2
      IF (QUAD. GT. 0.0) GO TO 5
      WRITE (NOUT,1000)
      CALL EXIT
C
C                          EVALUATE F FACTORS
C
5     IF (LSHFT. LT. 3) GO TO 20
      EMS=0.0
      FS=0.0
20    IF (LBDOT. LE. 2) FH=0.0
      IF (LBDOT. EQ. 3) FH=1.0
C
C                          EVALUATE SEVERAL DERIVATIVES
C
      IF (FS. EQ. 0.0) GO TO 50
```

```
      DERY(1)=-SIGMA/EMS
      GO TO 60
   50 DERY(1)=0.0
   60 DERY(5)=16.0*ELDSQ*B*EL*VT*FH
      DERY(6)=FS*DELTA-DERY(5)
      DERY(7)=-FS*DELTA
      DERY(11)=VS*(VS*DERY(7)+2.0*EMS*DERY(1))
      DERY(8)=VT*(1.0-FH)
C
C                    EVALUATE EFFECTIVE E* OF THE ROD MATERIAL
C
      IF (EFREE. EQ. 0.0) GO TO 65
      CALL RODES(VCM,VS,ESTRD)
      GO TO 67
   65 ESTRD=0.0
C
C                    EVALUATE BACKFACE EFFECT
C
   67 ESTAR=ESTRT
      IF (ILAYR. LT. NLAYR) GO TO 90
      BRKPT=THICK-4.0*B
      PENTH=YHEAD*COS(OBLIQ)
      IF (PENTH. LE. THICK) GO TO 70
      ESTAR=0.0
      GO TO 90
   70 IF (PENTH. LE. BRKPT) GO TO 90
      ESTAR=ESTRT*(1.0-(PENTH-BRKPT)/4.0/B)
   90 IF (YHEAD. LT. PEN) GO TO 93
      IF (VPERP. LT. 0.0) GO TO 93
      FORCE=ESTAR+CD*VPERP*VPERP/2.0
      DERY(14)=VPERP
      GO TO 95
   93 FORCE=0.0
      DERY(14)=0.0
   95 ETA=VT
      XI=VPERP-VCM
      ETA2=ETA*ETA
      XI2=XI*XI
      ZKR1=-DERY(5)*FH*(ETA2+XI2/3.0)
      ZKR2=-8.0*RHO*BSQ*ELDSQ*XI*FORCE
      FACT=VS-VCM
      ZKR3=2.0*SIGMA*FS*FACT
      ZKR4=-2.0*DERY(7)*(FACT*FACT/2.0-ESTRD)
      DERY(13)=ZKR1+ZKR2+ZKR3+ZKR4
      DERY(2)=-VCM*(DERY(5)+DERY(6))-VS*DERY(7)-EMS*DERY(1)
     1        -4.0*BSQ*ELDSQ*FORCE*RHO
      DERY(2)=DERY(2)/EMH
      DERY(12)=VCM*(VCM*DERY(6)+2.0*EMH*DERY(2))
      DERY(10)=DERY(11)+DERY(12)+DERY(13)
      DERY(9)=VPERP-VCM
      DERY(15)=VPERP
C
C                    FACTORS FOR VPERP AND VT DERIVATIVES
C
      ABAR=(3.0*DERY(13)-(1.5*ETA2+XI2)*DERY(6))/EMH
      C1=(DERY(1)-DERY(2))*FS/EMH
      FACT1=DERY(8)*VT/B
      FACT2=XI*(DERY(8)+VT)/EL
      CBAR=C1-2.0*(FACT1+FACT2)/B
C     FACT1=DERY(6)*(2.0*VT/B+XI/EL)/EMH
C     FACT2=XI2/EL/EL+2.0*VT*DERY(8)/BSQ
C     CBAR=C1-FACT1+FACT2
      DBAR=1.0/B
```

```
      EBAR=1.0/EL-F3/EMH
C
C                    LAST TWO DERIVATIVES
C
      DENOM=4.0*XI*DBAR-3.0*ETA*EBAR
      DERY(3)=DERY(2)+(2.0*ABAR*DBAR-3.0*ETA*CBAR)/DENOM
      DERY(4)=(CBAR-EBAR*(DERY(3)-DERY(2)))/2.0/DBAR
      RETURN
      END
```

```
C RODES-----ROD PROGRAM  ESTAR OF ROD
      SUBROUTINE RODES(VC1,VS1,ESTR)
C
C          THIS SUBROUTINE IN THE ROD PROGRAM
C          COMPUTES THE EFFECTIVE ESTAR OF THE ROD
C
      COMMON BMAX,SIGMA,ELOVD,ESTBK,EFREE,THICK,RHO,ESTRT,CD,F3
      COMMON OBLIQ,ESTAR,PPROJ,LBDOT,ILAYR,NLAYR,LSHFT
C
      RATIO=0.5*(VS1-VC1)**2/EFREE
      IF (RATIO. GE. ESTBK) GO TO 10
      ESTR=EFREE*RATIO/ESTBK
      RETURN
 10   ESTR=EFREE
      RETURN
      END
```

```
      SUBROUTINE OUTP(X,Y,DERY,IHLF,NDIM,PRMT)
      RETURN
      END
```

```
C HPCG = PREDICTOR-CORRECTOR ORDINARY DIFFERENTIAL EQUATION SOLVER
      SUBROUTINE HPCG(PRMT,Y,DERY,NDII,IHLI,FCT,OUTP,AUX)
      DIMENSION PRMT(5),Y(1),DERY(1),AUX(16,1)
      NDIM=NDII
      N=1
      IHLF=0
      X=PRMT(1)
      H=PRMT(3)
      PRMT(5)=0.0
      DO 1 I=1,NDIM
      AUX(16,I)=0.0
      AUX(15,I)=DERY(I)
    1 AUX(1,I)=Y(I)
      IF (H*(PRMT(2)-X)) 3,2,4
    2 IHLF=12
      GO TO 4
    3 IHLF=13
    4 CALL FCT(X,Y,DERY)
      CALL OUTP(X,Y,DERY,IHLF,NDIM,PRMT)
      IF (PRMT(5)) 6,5,6
    5 IF (IHLF) 7,7,6
    6 IHLI=IHLF
      RETURN
    7 DO 8 I=1,NDIM
    8 AUX(8,I)=DERY(I)
      ISW=1
      GO TO 100
    9 X=X+H
      DO 10 I=1,NDIM
   10 AUX(2,I)=Y(I)
   11 IHLF=IHLF+1
      X=X-H
      DO 12 I=1,NDIM
   12 AUX(4,I)=AUX(2,I)
      H=0.5*H
      N=1
      ISW=2
      GO TO 100
   13 X=X+H
      CALL FCT(X,Y,DERY)
      N=2
      DO 14 I=1,NDIM
      AUX(2,I)=Y(I)
   14 AUX(9,I)=DERY(I)
      ISW=3
      GO TO 100
   15 DELT=0.0
      DO 16 I=1,NDIM
   16 DELT=DELT+AUX(15,I)*ABS(Y(I)-AUX(4,I))
      DELT=0.06666667*DELT
      IF (DELT-PRMT(4)) 19,19,17
   17 IF (IHLF-10) 11,18,18
   18 IHLF=11
      X=X+H
      GO TO 4
   19 X=X+H
      CALL FCT(X,Y,DERY)
      DO 20 I=1,NDIM
      AUX(3,I)=Y(I)
   20 AUX(10,I)=DERY(I)
      N=3
      ISW=4
```

```
      GO TO 100
21    N=1
      X=X+H
      CALL FCT(X,Y,DERY)
      X=PRMT(1)
      DO 22 I=1,NDIM
      AUX(11,I)=DERY(I)
22    Y(I)=AUX(1,I)+H*(0.375*AUX(8,I)+0.7916667*AUX(9,I)
     1 -0.2083333*AUX(10,I)+0.04166667*DERY(I))
23    X=X+H
      N=N+1
      CALL FCT(X,Y,DERY)
      CALL OUTP(X,Y,DERY,IHLF,NDIM,PRMT)
      IF (PRMT(5)) 6,24,6
24    IF (N-4) 25,200,200
25    DO 26 I=1,NDIM
      AUX(N,I)=Y(I)
26    AUX(N+7,I)=DERY(I)
      IF (N-3) 27,29,200
27    DO 28 I=1,NDIM
      DELT=AUX(9,I)+AUX(9,I)
      DELT=DELT+DELT
28    Y(I)=AUX(1,I)+0.3333333*H*(AUX(8,I)+DELT+AUX(10,I))
      GO TO 23
29    DO 30 I=1,NDIM
      DELT=AUX(9,I)+AUX(10,I)
      DELT=DELT+DELT+DELT
30    Y(I)=AUX(1,I)+0.375*H*(AUX(8,I)+DELT+AUX(11,I))
      GO TO 23
100   DO 101 I=1,NDIM
      Z=H*AUX(N+7,I)
      AUX(5,I)=Z
101   Y(I)=AUX(N,I)+0.4*Z
      Z=X+0.4*H
      CALL FCT(Z,Y,DERY)
      DO 102 I=1,NDIM
      Z=H*DERY(I)
      AUX(6,I)=Z
102   Y(I)=AUX(N,I)+0.2969776*AUX(5,I)+0.1587596*Z
      Z=X+0.4557372*H
      CALL FCT(Z,Y,DERY)
      DO 103 I=1,NDIM
      Z=H*DERY(I)
      AUX(7,I)=Z
103   Y(I)=AUX(N,I)+0.2181004*AUX(5,I)-3.050965*AUX(6,I)+3.832865*Z
      Z=X+H
      CALL FCT(Z,Y,DERY)
      DO 104 I=1,NDIM
104   Y(I)=AUX(N,I)+0.1747603*AUX(5,I)-0.5514807*AUX(6,I)
     1 +1.205536*AUX(7,I)+0.1711848*H*DERY(I)
      GO TO (9,13,15,21),ISW
200   ISTEP=3
201   IF (N-8) 204,202,204
202   DO 203 N=2,7
      DO 203 I=1,NDIM
      AUX(N-1,I)=AUX(N,I)
203   AUX(N+6,I)=AUX(N+7,I)
      N=7
204   N=N+1
      DO 205 I=1,NDIM
      AUX(N-1,I)=Y(I)
205   AUX(N+6,I)=DERY(I)
      X=X+H
```

```
  206 ISTEP=ISTEP+1
      DO 207 I=1,NDIM
      DELT=AUX(N-4,I)+1.333333*H*(AUX(N+6,I)+AUX(N+6,I)-AUX(N+5,I)
     1 +AUX(N+4,I)+AUX(N+4,I))
      Y(I)=DELT-0.9256198*AUX(16,I)
  207 AUX(16,I)=DELT
      CALL FCT(X,Y,DERY)
      DO 208 I=1,NDIM
      DELT=0.125*(9.0*AUX(N-1,I)-AUX(N-3,I)+3.0*H*(DERY(I)+AUX(N+6,I)
     1 +AUX(N+6,I)-AUX(N+5,I)))
      AUX(16,I)=AUX(16,I)-DELT
  208 Y(I)=DELT+0.07438017*AUX(16,I)
      DELT=0.0
      DO 209 I=1,NDIM
  209 DELT=DELT+AUX(15,I)*ABS(AUX(16,I))
      IF (DELT-PRMT(4)) 210,222,222
  210 CALL FCT(X,Y,DERY)
      CALL OUTP(X,Y,DERY,IHLF,NDIM,PRMT)
      IF (PRMT(5)) 212,211,212
  211 IF (IHLF-11) 213,212,212
  212 IHLI=IHLF
      RETURN
  213 IF (H*(X-PRMT(2))) 214,212,212
  214 IF (ABS(X-PRMT(2))-0.1*ABS(H)) 212,215,215
  215 IF (DELT-0.02*PRMT(4)) 216,216,201
  216 IF (IHLF) 201,201,217
  217 IF (N-7) 201,218,218
  218 IF (ISTEP-4) 201,219,219
  219 IMOD=ISTEP/2
      IF (ISTEP-IMOD-IMOD) 201,220,201
  220 H=H+H
      IHLF=IHLF-1
      ISTEP=0
      DO 221 I=1,NDIM
      AUX(N-1,I)=AUX(N-2,I)
      AUX(N-2,I)=AUX(N-4,I)
      AUX(N-3,I)=AUX(N-6,I)
      AUX(N+6,I)=AUX(N+5,I)
      AUX(N+5,I)=AUX(N+3,I)
      AUX(N+4,I)=AUX(N+1,I)
      DELT=AUX(N+6,I)+AUX(N+5,I)
      DELT=DELT+DELT+DELT
  221 AUX(16,I)=8.962963*(Y(I)-AUX(N-3,I))-3.361111*H*(DERY(I)+DELT
     1 +AUX(N+4,I))
      GO TO 201
  222 IHLF=IHLF+1
      IF (IHLF-10) 223,223,210
  223 H=0.5*H
      ISTEP=0
      DO 224 I=1,NDIM
      Y(I)=0.00390625*(80.0*AUX(N-1,I)+135.0*AUX(N-2,I)+40.0*AUX(N-3,I)
     1 +AUX(N-4,I))-0.1171875*(AUX(N+6,I)-6.0*AUX(N+5,I)
     2 -AUX(N+4,I))*H
      AUX(N-4,I)=0.00390625*(12.0*AUX(N-1,I)+135.0*AUX(N-2,I)
     1 +108.0*AUX(N-3,I)+AUX(N-4,I))-0.0234375*(AUX(N+6,I)
     2 +18.0*AUX(N+5,I)-9.0*AUX(N+4,I))*H
      AUX(N-3,I)=AUX(N-2,I)
  224 AUX(N+4,I)=AUX(N+5,I)
      X=X-H
      DELT=X-(H+H)
      CALL FCT(DELT,Y,DERY)
      DO 225 I=1,NDIM
      AUX(N-2,I)=Y(I)
```

```
      AUX(N+5,I)=DERY(I)
  225 Y(I)=AUX(N-4,I)
      DELT=DELT-(H+H)
      CALL FCT(DELT,Y,DERY)
      DO 226 I=1,NDIM
      DELT=AUX(N+5,I)+AUX(N+4,I)
      DELT=DELT+DELT+DELT
      AUX(16,I)=8.962963*(AUX(N-1,I)-Y(I))-3.361111*H*(AUX(N+6,I)
     1 +DELT+DERY(I))
  226 AUX(N+3,I)=DERY(I)
      GO TO 206
      END
```